

CARDIFF
UNIVERSITY

PRIFYSGOL
CAERDYDD

**Optimisation of Processing Parameters for Fabrication of
Perovskite Solar Cells Under High Humidity**

**Thesis submitted in fulfilment of the requirement for the degree of
Doctor of Philosophy**

By

HAMED ABDULLAH EMJAHED IFHEEMA

July 2024

Declaration

I certify that this thesis has never been submitted for a degree, nor has it been considered for another degree or qualification at any other university. This thesis consists of my work and includes no collaborative results except where specifically indicated.

Hamed Ifheema

2024

Dedication

*To the souls of my Father and sister, whom I lost at the beginning
of my PhD journey*

May Allah Almighty have mercy upon them.

*To my blessed Mother
the priceless woman who lights my life*

*To my Brothers, Sisters, and family
the great and blessed individuals who have supported my
success.*

To my beloved Country, Libya

And to all others who love me

Abstract

Renewable energy sources, such as solar energy, have gained significant attention in addressing global energy challenges and promoting sustainable development. Perovskite solar cells (PSCs) are promising photovoltaic technology, which have a great potential in future due to their high efficiency and potentially low fabrication cost. However, their performance and stability are significantly affected by environmental conditions during fabrication. This thesis investigates the possibility of fabricating high performance perovskite solar cells in ambient air to eliminate the need for high-cost environmental chambers frequently used for fabrication of high-performance solar cells.

An initial study was conducted to explore suitable fabrication parameters for obtaining high power conversion efficiency (PCE). Through a series of experiments, the optimal annealing temperature was determined to be 90°C, yielding a PCE of 7.27%. The optimal spin-coating speed was found to be 4000 rpm, resulting in a PCE of 8.67%. Additionally, different antisolvents were tested, and methyl acetate was shown to be the best treatment, achieving a PCE of 10.63%. This study led to successful identification of suitable processes/parameters for fabrication of perovskite solar cells with respectable performance.

An systematic investigation was conducted to explore the fabrication of PSCs under high relative humidity of more than 70%RH, using various combinations of antisolvents. The combinations tested include Ethyl Acetate with Methanol, Methyl Acetate with Toluene, and Methyl Formate with Chlorobenzene. The best performance for each combination was as follows: 12.70 mW/cm² for Ethyl Acetate with 30% Methanol, 13.31 mW/cm² for Methyl Acetate with 30% Toluene, and 9.82 mW/cm² for Methyl Formate with 15% Chlorobenzene. To our knowledge, the power density of 13.31 mW/cm² from the treatment of Methyl Acetate with 30% Toluene represents the highest value of PSCs fabricated under high humidity of >70%RH, reported to date.

The findings from this work demonstrated the feasibility of fabricating PSCs in high humidity ambient air with respectable performance. The outcomes from this work indicates that further improvement is possible by exploring new combinations of treatments, opening up a truly low cost fabrication route.

Acknowledgements

The greatest praise goes to Allah (God), who has given me the wisdom, health, and patience to accomplish this task.

With the deepest gratitude, I would like to extend my best wishes to my primary supervisor, Professor Gao Min, for the outstanding guidance, intellectual support, and encouragement he provided throughout my graduate studies. Throughout my time of studying, I have learned a great deal from him academically and personally. The comments and advice you provided regarding my research, as well as my life and career, were invaluable. Additionally, I wish to thank my second supervisor, Dr. Victoria Garcia Rocha, for her generous support and academic guidance.

Additionally, I appreciate the support of my colleagues, Ali Bahr, Godwin Ugwuanyi, Abdullah Altuwaigi, and Martin Eze

My sincere thanks go out to the many people who have contributed to the success of this research and thesis. I would like to thank Libya's higher education ministry. Without their funding, this work would not have been possible. Thanks to them for their financial support and the invaluable PhD Scholarship.

It is also highly appreciated that the academic and technical support staff within the school helped with the construction of the equipment used for the experimental work, as well as the design of the printed circuit boards. Thanks are due to the Postgraduate Research Coordinator and the other administrative staff members.

Table of contents

Abstract	iii
Acknowledgements	iv
Table of contents	v
List of figures	ix
List of tables	xiv
Chapter 1: Introduction	1
1.1 Background.....	1
1.2 Aims	2
1.3 Objectives	2
1.4 Thesis structure	3
Chapter 2: Literature review	5
2.1 Introduction.....	5
2.2 Renewable energy	5
2.2.1 Solar energy	6
2.2.2 Geothermal energy	6
2.2.3 Biomass Energy	6
2.2.4 Wind energy	7
2.2.5 Hydro energy.....	7
2.3 Solar cells.....	7
2.3.1 Development of the solar cells	8
2.3.2 Working principle and Structure of the solar cells	12
2.3.3 Performance evaluation of the solar cell.....	15
2.3.3.1 Solar cells equivalent circuit.....	15
2.3.3.2 Series resistance (R_s) and shunt resistance (R_p).....	16
2.3.3.3 Fill factor (FF)	16
2.3.3.4 Power conversion efficiency (PCE).....	17

Table of contents

2.4	Factors that influence the efficiency of solar cells.....	18
2.4.1	Irradiance intensity	18
2.4.2	Temperature	19
2.5	Perovskite Solar Cells.....	21
2.5.1	Structure of the perovskite solar cells	22
2.5.2	Perovskite solar cells operation principles	25
2.5.3	Work function and energy band gap	26
2.5.4	Impact of Humidity on Perovskite Film Properties.....	27
2.6	Performance in controlled environment.....	28
2.6.1	Advances in Power Conversion Efficiency Under Controlled Conditions .	32
2.6.2	Factors Influencing Device Stability	38
2.6.2.1	Impact of Temperature	39
2.6.2.2	Influence of Moisture and Oxygen.....	40
2.6.2.3	Impact of UV Light (Photostability).....	41
2.6.3	Importance of Controlled Environment.....	44
2.7	Ambient Atmosphere Fabrication	45
2.7.1	Issues with fabrication in uncontrolled environment.....	45
2.7.2	Strategies to improve device efficiency in ambient atmosphere fabrication.	47
2.7.3	Recent progress and performance in ambient atmosphere fabrication ..	47
2.8	Summary.....	53
Chapter 3: Methodology and Experimental procedure		54
3.1	Introduction.....	54
3.2	Structure and experimental procedure of a perovskite solar cell	54
3.3	Preparation of the materials and device.....	55
3.3.1	Fluorine-doped Tin Oxide Glass Substrate (FTO).....	56
3.3.2	Electron transport layer (SnO ₂)	59
3.3.3	Perovskite active layer (MAPbI ₃).....	61

Table of contents

3.3.4	Hole transport layer (Spiro-OMeTAD)	63
3.3.5	Sputtering of silver deposition (Ag)	64
3.4	Characterisation of device layers	65
3.4.1	Ultraviolet-visible (UV-Vis) spectroscopy.....	66
3.4.2	X-ray diffraction (XRD)	69
3.4.3	Atomic force microscopy (AFM)	70
3.4.4	Fourier-transform infrared spectroscopy (FTIR)	71
3.4.5	Scanning electron microscopy (SEM).....	72
3.5	Evaluate the performance of the perovskite solar cells	73
3.5.1	Current -Voltage measurements	73
3.5.2	Impedance spectroscopy	75
3.5.3	Sheet resistance	77
3.6	Summary.....	78
Chapter 4: Establish in air fabrication procedures.....		79
4.1	Introduction.....	79
4.2	Establish initial fabrication procedure	79
4.2.1	Film and device fabrication	79
4.2.2	Performance of the devices	80
4.3	Optimisation fabrication procedure.....	82
4.3.1	Optimising annealing temperature of MAPbI ₃ layer	83
4.3.1.1	Film and device fabrication	83
4.3.1.2	Result and discussion	84
4.3.2	Optimising spin-coating speed of MAPbI ₃ layer	90
4.3.2.1	Film and device fabrication	90
4.3.2.2	Result and discussion	90
4.3.3	Treatment of MAPbI ₃ layer with various antisolvents.....	96
4.3.3.1	Film and device fabrication	96
4.3.3.2	Result and discussion	96

Table of contents

4.4	Effect of humidity on device performance	104
4.5	Summary.....	105
Chapter 5: Fabrication under high relative humidity.....		107
5.1	Introduction.....	107
5.2	Mixed antisolvent of ethyl acetate and methanol.....	107
5.2.1	Film and device fabrication	108
5.2.2	Properties of the prepared MAPbI ₃ films.....	108
5.2.3	Photovoltaic performance of the devices.....	113
5.3	Mixed antisolvent of methyl acetate and toluene.....	115
5.3.1	Film and device fabrication	115
5.3.2	Properties of the prepared MAPbI ₃ films	116
5.3.3	Photovoltaic performance of the devices.....	119
5.4	Mixed antisolvent of methyl formate and chlorobenzene	121
5.4.1	Film and device fabrication	121
5.4.2	Properties of the prepared MAPbI ₃ films	122
5.4.3	Photovoltaic performance of the devices.....	125
5.5	Stability of the best-performing devices.....	127
5.6	Summary.....	129
Chapter 6: Conclusion		130
6.1	Conclusion	130
6.2	Future work	132
References		133
Appendix A: Other results not included in the main chapters.		156

List of figures

Figure 2-1 illustrates the different types of solar cells and their efficiency improvements over years[36].....	11
Figure 2-2 Solar irradiance spectrum above atmosphere and at surface [33]	13
Figure 2-3 Schematic diagram of silicon solar cell with p-n junction.[46]	15
Figure 2-4 Solar cells equivalent circuit[47]	16
Figure 2-5 Effect of irradiance intensity on I-V curves[51]	19
Figure 2-6 Effect of temperature on I-V curves [51]	20
Figure 2-7 Effect of temperature Coefficients of Voc and Jsc in Perovskite Solar Cells[64].....	21
Figure 2-8 Perovskite solar cells efficiency in the years [73]	22
Figure 2-9 Crystal structure of perovskite ABX ₃	23
Figure 2-10 (a) Standard PSCs structure and (b) Inverted PSC structure.[84]	24
Figure 2-11 Schematic diagram of energy levels and transport processes of electrons and holes in an HTM/perovskite/SnO ₂ cell[91].....	26
Figure 2-12 Schematic energy level diagram of TiO ₂ , (CH ₃ NH ₃)PbI ₃ and spiro-MeOTAD[96].	27
Figure 2-13 The SEM images show the perovskite layer prepared under nitrogen at 0%, 10%, 20%, and 40% RH[99].	28
Figure 2-14 A possible degradation pathway of metal halide perovskites in presence of water[132].	40
Figure 2-15 SEM images of CH ₃ NH ₃ PbI ₃ perovskite films were analyzed after spin-coating and annealing at 0%, 30%, 50%, and 75% relative humidity. Films at 0% RH were processed in a nitrogen-filled glovebox, with different antisolvents used during spin-coating[190]	48
Figure 2-16 SEM images of perovskite films annealed in ambient air (a) and (b) in vacuum.....	49
Figure 3-1 Structure of the perovskite solar cell.....	55
Figure 3-2 sequential deposition process that starts from the initial stages and progresses to complete device fabrication.....	56

List of figures

Figure 3-3 a) Schematic diagram showing the design of FTO substrate, (b) Photograph of FTO substrate, (c) Ultrasound bath and (d) UV-ozone cleaner, e) Schematic diagram of the completed device structure of perovskite solar cells.....58

Figure 3-4 a) Laurell spin-coater used for this research, b) Annealing of the SnO₂ coated FTO substrate in a petri dish, c) SnCl₂ solution, and d) FTO glass coated with SnO₂ layer after annealing.61

Figure 3-5 a) MAPbI₃ solution and b) FTO glass/SnO₂/MAPbI₃..... 62

Figure 3-6 a) the Spiro-OMETAD solution and b) the fabricated FTO glass/SnO₂/MAPbI₃/Spiro-OMeTAD structure.....63

Figure 3-7 a) PLD2000 for magnetron sputtering, b) Substrate holder, c) Photograph of fabricated devices with four perovskite solar cells formed underneath the deposited silver layers, and d) Photograph of the perovskite solar cells with contact wires soldered on silver pads.65

Figure 3-8 Hitachi U-1900 Spectrophotometer66

Figure 3-9 Schematic representation of Beer-Lambert law.....67

Figure 3-10 Tauc plot of the fabricated MAPbI₃ film showing an energy band gap of 1.55 eV.68

Figure 3-11 Siemens D5000 X-ray diffractometer system.70

Figure 3-12 Dimension 3100 AFM instrument.....71

Figure 3-13 Shimadzu FTIR-8400S spectrophotometer72

Figure 3-14 Zeiss 1540 XB Crossbeam Field emission scanning electron microscope (FE-SEM).....73

Figure 3-15 Newport Oriel LCS-100 solar simulator/PGSTAT302N Autolab Metrohm setup for I-V measurement system.....74

Figure 3-16 the current -voltage (I-V) curve of tested silicon solar cell.....75

Figure 3-17 an example schematic of impedance spectra for PSC device.....76

Figure 3-18 In-house built apparatus for 4-probe measurement.....77

Figure 4-1 J-V characteristics of the initial experiment81

Figure 4-2 J-V characteristics of the best performing devices for different annealing temperatures of MAPbI₃ layers..... 85

Figure 4-3 a) Absorbance spectra of MAPbI₃ layers fabricated at different annealing temperatures b) Tauc plot of MAPbI₃ layers at different annealing temperatures

Figure 4-4 a) presents the XRD spectra of the MAPbI₃ films deposited on FTO/SnO₂ substrates at

List of figures

different annealing temperatures (60°C, 90°C, 120°C, and 150°C). The diffraction peaks observed at 14.38(110), 20.32(211), 28.18(220), and 32.18(310) correspond to specific crystal planes of the perovskite films of the tetragonal phase as reported in [188]–[190]. While the peaks at 24.80(110), 35.53(101), and 38.06 (200) correspond to the FTO/SnO₂ films. It can be seen that the typical perovskite peaks are presented in all the films regardless annealing temperatures, indicating the formation of perovskite crystals. However, the peaks of the films annealed at 90°C appear to be more pristine, suggesting the better quality of crystals. Furthermore, the films annealed at 90°C exhibit a relatively small FWHM (Full Width at Half Maximum) as shown in Figure 4-4 b). This implies that relatively large crystals were formed after annealing at 90°C, compared to other annealing temperatures. In solar cell applications, large perovskite crystals are preferred due to their high carrier mobility. The results from this analysis indicates that 90°C is a favourable annealing temperature to obtain good quality perovskite films.86

Figure 4-4 a) XRD spectra of FTO/SnO₂ /MAPbI₃ at different annealing temperatures
b) The Full Width at Half Maximum (FWHM) of the MAPbI₃ peaks of different annealing temperatures.87

Figure 4-5 a-d) AFM topography images of MAPbI₃ at different annealing temperatures e) RMS roughness of MAPbI₃ film vs annealing temperatures89

Figure 4-6 J-V characteristics of the best devices as a function of different spin coating speeds.....92

Figure 4-7 a) MAPbI₃ absorbance spectra at various spin coating speeds. b) MAPbI₃ Tauc plot as a function of different spin coating speed93

Figure 4-8 a) XRD spectra of FTO/SnO₂ / MAPbI₃ prepared at different spin-coating speeds. b) The full width at half-maximum (FWHM) of the MAPbI₃ peaks vs spin-coating speed.94

Figure 4-9 (a-d) AFM images of MAPbI₃ at different spin coating speed. e) RMS roughness of MAPbI₃ film vs different spin coating speed.....95

Figure 4-10 J-V characteristics of the best performing devices treated using different antisolvents97

Figure 4-11 a) Absorbance of MAPbI₃ films treated by different antisolvents. b) Tauc plots of the MAPbI₃ films treated by different antisolvents.....99

List of figures

Figure 4-12 a) XRD spectra of the MAPbI₃ layers on FTO/SnO₂ substrates with different antisolvent treatment b) FWHM values of the XRD peaks of the MAPbI₃ films treated using different antisolvents. 101

Figure 4-13 AFM images of MAPbI₃ films treated by a) methyl acetate, b) toluene, c) ethyl acetate, d) ethanol, e) methyl formate and f) chlorobenzene; g) RMS roughness of corresponding MAPbI₃ films. 103

Figure 4-14 Improvements in power conversion efficiency comparing to relative humidity 105

Figure 5-1 (a) Absorbance of the MAPbI₃ films treated using the mixed ethyl acetate-methanol antisolvent with a varied ratio of 0%, 15%, 30% and 40% methanol, respectively; (b) Tauc plots of the corresponding films..... 109

Figure 5-2 a) XRD pattern of MAPbI₃ films treated using the mixed antisolvent of ethyl acetate and methanol at the ratio of 0%, 15%, 30% and 45% methanol, respectively. b) The FWHM values of the corresponding films..... 111

Figure 5-3 a) AFM images of MAPbI₃ with different antisolvent concentrations of Ethyl acetate and methanol. b) RMS roughness of the films 112

Figure 5-4 J-V characteristics of the best-performing devices fabricated using mixed antisolvent of ethyl acetate and methanol with different mix ratios. 113

Figure 5-5 (a) The absorbance of MAPbI₃ films treated with pure methyl acetate and varying ratios of added toluene (b) Tauc plots films. 116

Figure 5-6 a) XRD patterns of MAPbI₃ films treated by the mixed antisolvent of methyl acetate and toluene with different ratio of mixture, b) The FWHM values of the corresponding films..... 118

Figure 5-7 AFM images of the MAPbI₃ films treated using the mixed antisolvent with the ratio of a) 0% toluene, b) 15% toluene, c) 30% toluene, d) 45% toluene; and e) RMS roughness of the corresponding films 119

Figure 5-8 J-V characteristics of the best devices as a function of different antisolvent concentrations of Methyl Acetate and Toluene 121

Figure 5-9 (a) Absorbance of MAPbI₃ films treated with pure methyl formate and different mixture of methyl acetate with chlorobenzene (b) Tauc plots of the corresponding films..... 122

List of figures

Figure 5-10 a) XRD pattern of MAPbI₃ films treated using the mixed antisolvent of methyl acetate and chlorobenzene with different ratio of mixture , b) The FWHM values as a function of the ratio of mixture.....124

Figure 5-11 AFM images of the MAPbI₃ films treated using the mixed antisolvent of methyl acetate and chlorobenzene with different percentage of chlorobenzene at a) 0%, b) 15%, c) 30%, and d) 45%, e) RMS roughness of the films.....125

Figure 5-12 J-V characteristics of the best-performing devices treated using the mixed antisolvent of methyl acetate and chlorobenzene with a varied ratio of mixtures.126

Figure 5-13 The maximum power outputs as a function of operating period for the best-performing devices treated by three different mixed antisolvents.128

Figure 6-1 A) and B) illustrate the error between experimental and calculated I-V curves for perovskite devices.....156

Figure 6-2 A) Transmission spectrum of FTO substrates and SnO₂ films deposited on FTO substrates. B) absorbance spectrum of FTO substrates and SnO₂ films deposited on FTO substrates.157

Figure 6-3 A) Transmittance spectra of FTO/SnO₂/MAPbI₃ films. B) absorbance spectra of FTO/SnO₂/MAPbI₃ films.....157

Figure 6-4 illustrates the humidity levels recorded over time in lab C3.03 at Cardiff University158

Figure 6-5 illustrates the Nyquist plot, which was generated by adding a combination of ethyl acetate and methanol as antisolvents at varying concentrations.....158

Figure 6-6 illustrates the Nyquist plot, which was generated by adding a combination of methyl acetate and toluene as antisolvents at varying concentrations.....159

Figure 6-7 illustrates the Nyquist plot, which was generated by adding a combination of methyl formate and chlorobenzene as antisolvents at varying concentrations. ...159

Figure 6-8 illustrates the FTIR spectra, which was generated by adding a combination of ethyl acetate and methanol as antisolvents at varying concentrations.....160

Figure 6-9 illustrates the FTIR spectra, which was generated by adding a combination of methyl acetate and toluene as antisolvents at varying concentrations.....161

Figure 6-10 illustrates the FTIR spectra, which was generated by adding a combination of methyl formate and chlorobenzene as antisolvents at varying concentrations.162

List of tables

Table 2-1	List of the most efficient PSCs constructed in a controlled environment. ...	30
Table 2-2	List of champion perovskite solar cells.	34
Table 2-3	List of the research efforts focusing on improving device stability	43
Table 2-4	List of the perovskite solar cells fabricated in ambient air.	51
Table 4-1	Photovoltaic parameters of the perovskite devices for the initial experiment	82
Table 4-2	Photovoltaic parameters of the fabricated perovskite devices for different MAPbI ₃ annealing temperatures ("Best" denotes the data obtained from the best- performing devices and "Ave" denotes the average performance of 16 PSCs and the area of each device is(0.15 cm ²)	84
Table 4-3	Photovoltaic parameters of the perovskite devices fabricated using the MAPbI ₃ layers prepared at different spin coating speeds ("Best" denotes the data obtained from the best-performing devices and "Ave" denotes the average performance of 16 PSCs and the area of each device is(0.15 cm ²)	91
Table 4-4	Photovoltaic parameters of the perovskite devices treated using different antisolvent ("Best" denotes the data obtained from the best-performing devices and "Ave" denotes the average performance of 16 PSCs and the area of each device is(0.15 cm ²).	98
Table 5-1	Photovoltaic parameters of perovskite solar cells fabricated using mixed antisolvent of ethyl acetate and methanol and tested under AM1.5 G illumination. ("Best" denotes the data obtained from the best-performing devices and "Ave" denotes the average performance of 16 PSCs and the area of each device is(0.15 cm ²)	115
Table 5-2	Photovoltaic parameters of the PSCs fabricated using the mixed antisolvent of methyl acetate and toluene ("Best" denotes the data obtained from the best- performing devices and "Ave" denotes the average performance of 16 PSCs and the area of each device is(0.15 cm ²).	120
Table 5-3	summarizes the photovoltaic performance parameters of PSCs fabricated with a methyl formate and chlorobenzene anti-solvent combination ("Best" denotes the data obtained from the best-performing devices and "Ave" denotes the average performance of 16 PSCs and the area of each device is(0.15 cm ²).	127

List of tables

Table 6-1 presents the measured electrical performance parameters of several perovskite devices.....163

List of planned publications:

- Exploring Methyl Formate as a Promising Antisolvent for Perovskite Solar Cell Fabrication in uncontrolled Humidity Conditions
- Effects of Varying Antisolvent Ratios on Enhancing Perovskite Solar Cell Performance Under High-Humidity Conditions

Chapter 1: Introduction

1.1 Background

The confluence of rapid industrial development and the burgeoning global population in the 21st century has thrust humans inevitably into a critical juncture marked by severe energy crises and climate change, a consequence of our overwhelming dependence on fossil fuels. According to the International Energy Agency (IEA), the production, transport, and processing of oil and gas resulted in 5.1 billion metric tons (Gt) of CO₂ emission in 2022 just under 15% of global energy sector GHG emissions[1] [2], [3]About half of these emissions came from flaring and methane released during oil and gas operations. The act of burning these fossil fuels for electricity generation not only underscores our reliance but also leads to the substantial production and emission of carbon dioxide, a well-known primary greenhouse gas in the environment[3]. Recognizing the interconnectedness of these factors emphasizes the urgency for a shift towards sustainable energy sources to mitigate the unfolding environmental challenges[4], [5].

Solar cells have emerged as a crucial future energy source due to their ability to convert sunlight into electricity. The evolution of solar cell technology has progressed through three generations: the first generation based on silicon wafers, the second generation utilizing thin-film technologies, and the third generation, which includes perovskite solar cells. Perovskite solar cells are particularly noted for their high efficiency, low production costs, and versatility in application[7]. These characteristics have made them a focal point of research for many scientists, as they present a sustainable solution to global energy demands. The significant efficiency improvements and potential for low-cost production in perovskite solar cells offer an exciting opportunity to transform the solar energy market.

Despite their promise, perovskite solar cells face significant challenges, particularly concerning their power conversion efficiency (PCE) and durability. One major issue is the sensitivity of perovskite materials to humidity, which can severely degrade their performance[8]. It has been observed that fabricating these cells in an air environment often leads to suboptimal performance due to moisture exposure, although this method can significantly reduce production costs compared to fabrication in controlled environments. Understanding and mitigating the effects of humidity on perovskite solar

cells are essential for improving their performance and commercial viability. Consequently, research efforts are concentrated on addressing these challenges to enhance the stability and efficiency of perovskite solar cells, aiming to make air fabrication a viable and cost-effective method for large-scale production[8]. This objective aligns with the broader goal of developing sustainable and affordable energy technologies.

1.2 Aims

- To enhance the performance and stability of perovskite solar cells (PSCs) fabricated under high-humidity conditions.
- To explore the use of mixed antisolvents as a solution to improve the quality of perovskite films and their resistance to moisture.

1.3 Objectives

1. Systematic Investigation:

- Analyse the optimal processing parameters for in-air fabrication of PSCs, including:
 - Annealing temperature.
 - Spin-coating speed.
 - Choice and combination of antisolvents.

2. Development and Testing:

- Explore the potential of mixed antisolvents in overcoming the limitations of single antisolvents, particularly under high-humidity conditions (>70%).
- Evaluate the J-V characteristics (current density-voltage relationship) of PSCs fabricated under various conditions.

3. Performance Optimization:

- Determine the combinations of processing parameters and antisolvents that yield the highest power conversion efficiency (PCE).
- Test the humidity tolerance of PSCs fabricated with mixed antisolvents compared to single antisolvents.

4. Enhance Stability:

- Investigate the role of mixed antisolvents in not only boosting PCE but also improving the stability of PSCs under high humidity

1.4 Thesis structure

This thesis describes a research effort in exploring the possibility of fabricating efficient perovskite solar cells in high humidity ambient air. It consists of six chapters and the main focuses of each chapter are summarised as follows.

Chapter 1

In chapter 1, the background and motivation for the research are introduced. The chapter outlines the primary objectives and provides an overview of the structure of the thesis.

Chapter 2

Chapter 2 provides a comprehensive literature review on the key topics that are relevant to this research, starting with renewable energy sources (including solar energy, geothermal energy, biomass energy, wind energy, and hydro energy). It delves into the structure and working principles of solar cells, along with a detailed examination of performance evaluation, factors influencing efficiency (such as irradiance intensity and temperature), and an overview of perovskite solar cells. The chapter also scrutinizes the improved performance of solar cells in controlled environments, addressing power conversion efficiency and device stability under various conditions like temperature, moisture, oxygen, and UV light. It further discusses the importance of a controlled environment and explores ambient atmosphere fabrication techniques, highlighting challenges, strategies for efficiency improvement, and recent progress in this approach.

Chapter 3

Chapter 3 focuses on the methodology and experimental procedures, beginning with an introduction and detailing the structure and experimental procedure of a perovskite solar cell. The chapter further outlines the preparation steps for materials and device components, including the Fluorine-doped Tin Oxide (FTO) glass substrate, electron transport layer (SnO₂), perovskite active layer (MAPbI₃), hole transport layer (Spiro-OMeTAD), and sputtering of silver deposition (Ag). This is followed by a brief description

Chapter 1: Introduction

of the techniques for characterization of device layers, including Ultraviolet-visible spectroscopy (UV-Vis), X-ray diffraction (XRD), Atomic force microscopy (AFM), Fourier-transform infrared spectroscopy (FTIR), and Scanning electron microscopy (SEM). The performance evaluation of perovskite solar cells is then discussed, involving a Solar cell simulator, Current-Voltage measurements, and Impedance spectroscopy.

Chapter 4

In Chapter 4, the focus is on establishing device fabrication procedures in ambient air, commencing with an introduction and the initial fabrication procedure, including film and device fabrication, as well as an evaluation of device performance. The chapter then progresses to the optimization of fabrication procedures, exploring the annealing temperature, the spin-coating speed, and the treatment of the MAPbI₃ layer with various antisolvents. Each optimization section includes sub-sections on film and device fabrication, results, and discussions. The chapter ends with an examination of improvements in yield and power conversion efficiency.

Chapter 5

In Chapter 5, the exploration of antisolvent combinations was carried out to improve the fabrication capability in high humidity ambient. Each section dedicated to a detailed investigation of a specific antisolvent combination, beginning with Ethanol and Methanol, and then Methyl Acetate and Toluene, and finally Methyl Formate and Chlorobenzene, with sub-sections focusing on film and device fabrication, the properties of the prepared MAPbI₃ films, and the photovoltaic performance of the devices.

Chapter 6

In Chapter 6, the main outcomes and conclusions of this study are summarised and the recommendations for further research were discussed.

Chapter 2: Literature review

2.1 Introduction

In recent years, perovskite solar cells (PSCs) have emerged as a promising alternative to traditional silicon-based solar cells due to their high efficiency, low-cost production, and flexibility in device design. PSCs utilize a hybrid organic-inorganic metal halide perovskite material as the light-harvesting layer, which has shown exceptional photovoltaic performance and has rapidly attracted extensive research attention. With significant progress in the development of PSC technology, numerous studies have investigated the optimization of perovskite materials, device architectures, and fabrication methods to improve the efficiency and stability of PSCs. This literature review aims to provide a general understanding of various types of renewable energy, as well as an overview of the working principle of solar cells and factors that affect the performance of the solar cells, the improvements that occurred on the perovskite solar cells and the current state-of-the-art of perovskite solar cells for both fabrication methods under controlled and non-controlled atmosphere.

2.2 Renewable energy

In the future, renewable energy sources will have a significant impact on the world's energy usage. There are three types of energy resources: fossil fuels, renewable sources, and nuclear resources. Renewable resources are sources of energy that can be repeatedly used to generate power, such as solar energy, wind energy, biomass energy, and geothermal energy. These resources are sometimes referred to as alternative sources of energy [9], [10]. Renewable energy sources have the potential to meet domestic energy needs while emitting little or no air pollutants or greenhouse gases. The development of renewable energy systems can address important challenges such as enhancing energy supply reliability and efficiency, resolving issues related to local energy and water supply, improving living standards and employment opportunities for residents, and promoting sustainable development in remote areas located in mountain and desert regions [11], [12]. Additionally, implementing renewable energy sources can help countries fulfil their international obligations related to

protecting the environment [13]. The establishment and execution of renewable energy initiatives in rural regions can result in employment opportunities and reduce the need for individuals to migrate to urban areas. Collecting renewable energy through a decentralized approach is a feasible method for meeting the energy requirements of rural and small-scale communities in a dependable, cost-effective, and ecologically sustainable manner [14].

The most popular and promising renewable energy sources include solar energy, geothermal energy, biomass energy, wind energy, hydro energy.

2.2.1 Solar energy

Sunlight is an abundant and easily accessible energy source for our planet. In fact, the amount of solar energy that reaches the earth's surface in an hour exceeds the planet's total energy requirements for an entire year [15]. Despite its apparent advantage as a renewable energy source, solar energy availability is affected by the time of day, season, and location. Solar energy has become a more and more popular option for supplementing energy consumption in most countries worldwide [16].

2.2.2 Geothermal energy

Geothermal energy, which takes advantage of the natural heat beneath the earth's surface, can be used for direct home heating or power generation [17], [18]. Despite its direct use of subterranean resources, geothermal energy is less used in comparison to other renewable energy sources [19].

2.2.3 Biomass Energy

Biomass electricity generation involves the transformation of plant-derived solid fuel into electrical energy. While biomass typically entails the combustion of organic matter to produce electricity, contemporary biomass conversion methods are notably cleaner and more efficient [20]. By converting various waste materials, including agricultural, industrial, and household refuses, into solid, liquid, or gaseous fuel, biomass power generation achieves a more cost-effective and eco-friendly energy solution [21].

2.2.4 Wind energy

Clean energy can be abundantly obtained from the wind. Many countries have now become familiar with the sight of wind farms, as wind power continues to make a growing contribution to various country's National Grid [22]. To produce electricity from wind energy, turbines are utilized to power generators that then transfer the electricity to the National Grid.

2.2.5 Hydro energy

Hydropower, a prominent renewable energy resource, has achieved widespread commercialization and utilization. The process involves the construction of dams or barriers to create expansive reservoirs, enabling a regulated flow of water that, in turn, propels turbines to generate electricity [23]. This energy source boasts greater reliability compared to solar or wind power. Notably, in the case of tidal energy, it possesses the added capability of storing electricity for peak demand. Similar to solar and wind energy, hydropower stands as a sustainable and environmentally friendly source of energy [24].

2.3 Solar cells

Solar cells represent an exceedingly promising energy source, manifesting a substantial advantage over conventional power generation systems by effecting a seamless conversion of sunlight into solar energy. This method of direct conversion not only underscores its cost-effectiveness but also aligns with environmentally conscious practices, obviating the generation of toxic materials. Consequently, considered as one of the most promising green energy sources.

In the past, silicon wafers were the preferred material for the production of solar cells. However, their massive investment required for production facilities makes silicon technology less accessible to under-developed countries and regions. On the other hand, the thin-film solar cell technologies usually require less expensive production equipment and

provide a “low-cost” alternative to silicon wafer counterparts, leading a transformation in the domain of solar energy innovation[25].

2.3.1 Development of the solar cells

Since Becquerel discovered the photovoltaic effect in 1839, the concept of using solar energy for electricity generation has been frequently explored. In recent decades, the research community has made significant efforts to identify the most effective and economical solar cells. This stems from realizing that the sun's energy received by Earth's atmosphere every hour is sufficient to meet global energy demands for an entire year [26]. Therefore, finding sustainable and eco-friendly ways to generate electricity has become a top priority.

The evolution of solar cells unfolds as a fascinating journey, marked by distinct generations and propelled by technological advancements aimed at enhancing efficiency, cutting costs, and broadening applications. The first generation, originating in the 1950s, predominantly employed crystalline silicon as the semiconductor material, laying the foundation for practical applications in space exploration and satellite technology. However, despite their pioneering role, these cells faced barriers to widespread adoption due to cost and efficiency limitations. The subsequent emergence of the second generation in the 1980s introduced thin-film solar cells, leveraging materials such as amorphous silicon, cadmium telluride, and copper indium gallium selenide. Despite being less efficient than their crystalline counterparts, thin-film solar cells found niche applications and offered a more economically viable alternative.

Since the first production of solar cells, solar cell technology has advanced significantly, and it has been classified into three generations based on their distinct features and characteristics. The first generation of solar cells, which is widely used and commercially established, primarily uses silicon wafers in either monocrystalline or polycrystalline form [27]. These cells are highly efficient, with a laboratory efficiency range of 22% to more than 25%. However, their efficiency is limited by the spectral response of silicon single-junction semiconductors, which cannot capture the full range of light wavelengths and convert them into electrical energy.

To overcome the limitations of the first-generation solar cells, researchers and manufacturers have developed the second generation of solar cells that use thin-film semiconductors. These cells are cheaper than silicon wafer technology, as they require a significant reduction in the amount of material used and different production processes like vacuum deposition. Amorphous silicon, cadmium telluride (CdTe), and copper indium gallium selenide (CIGS) are some of the commonly used thin-film semiconductors. These cells have unique features like flexibility, making them suitable for specific applications [28]. However, their efficiency is slightly lower than traditional cells. The third generation of solar cells utilizes novel materials and architectures, with the goal of achieving very high efficiency and/or very low production costs. These cells are designed to overcome the limitations of the previous two generations and provide a viable alternative to traditional power sources [29]. Examples of third-generation solar cells include multijunction solar cells (MJSCs), dye-sensitized solar cells (DSSCs), quantum dot-sensitized solar cells, organic solar cells (OSCs), and perovskite solar cells (PSCs). Each type of cell has specific advantages and limitations, including cost, stability, efficiency, and unique properties such as flexibility and transparency [30].

Multijunction solar cells (MJSCs), for instance, are capable of capturing a broader range of light wavelengths by using multiple layers of semiconductors with varying bandgaps [31]. This results in a higher efficiency rate, as more energy from the sun is converted into electricity. Dye-sensitized solar cells (DSSCs) use organic dyes that absorb light and transfer electrons to the semiconductor layer, increasing their efficiency and reducing the amount of material required [32]. Quantum dot-sensitized solar cells, on the other hand, use tiny semiconductor particles that can be precisely tuned to absorb specific wavelengths of light, increasing the efficiency of the cell. Organic solar cells (OSCs) utilize carbon-based materials as semiconductors, making them lightweight, flexible, and transparent [33].

In recent years, perovskite solar cells have shown great promise. PSCs are composed of perovskite materials that have a favourable crystal structure, which allows to absorb a wide range of light wavelengths and achieve a high conversion efficiency [34]. Additionally, they can be produced using simple and cost-effective fabrication techniques, making them a promising candidate for large-scale production. However, PSCs also face some challenges, such as long-term stability and scalability issues [35]. Nonetheless, the ongoing research and development in the field of PSCs continue to show potential for significant

advancements in the future. Figure 2-1 illustrates the different types of solar cells and their efficiency improvements over years [35].

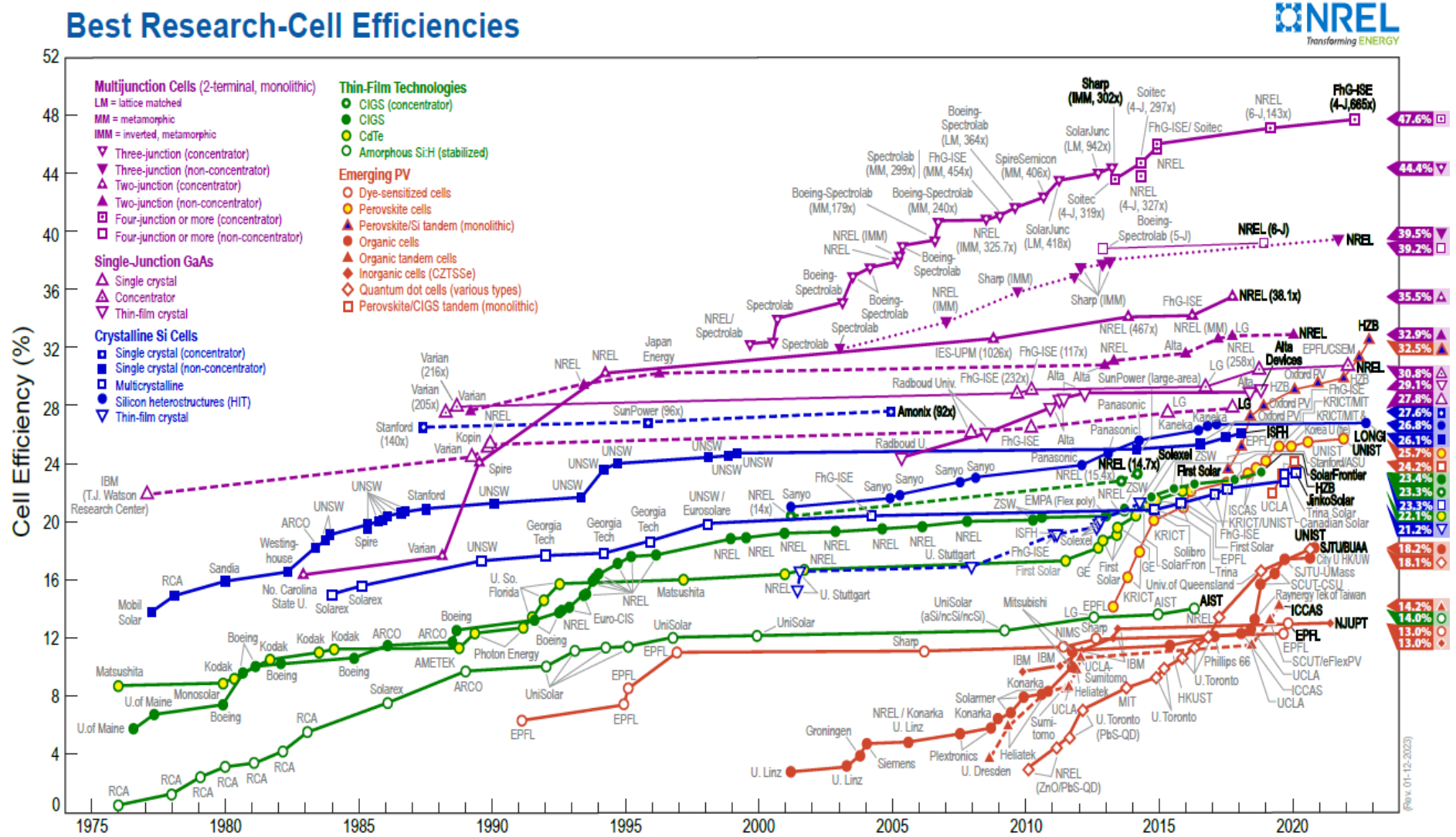


Figure 2-1 illustrates the different types of solar cells and their efficiency improvements over years [36].

2.3.2 Working principle and Structure of the solar cells

The efficiency of solar cells is based on the ability of the device to capture solar irradiance across the wavelength of the entire solar spectrum. This spectrum encompasses a range from 100 nm to 1 mm, with the most substantial energy density concentrated between 250 nm and 2500 nm. This energy distribution is visually presented in Figure 2-2, clearly emphasizing that the peak of energy concentration aligns specifically with the visible light spectrum spanning 400-700 nm. Consequently, the strategic focal point for solar cells lies in their capacity to absorb the maximum possible energy within this visible region of the solar spectrum to reach the high efficiency [27], [37]. However, by the assumption that the sun behaves as a blackbody with a temperature of 6000K, emitting radiation at a rate of approximately 158 mW/cm². It's important to note that contemporary understanding recognizes the influence of the Earth's atmosphere on solar radiation reaching the surface, altering its spectral energy distribution. International standards precisely define solar spectral irradiance at Earth's surface, notably through the widely used AM 1.5G spectrum, essential in photovoltaic research and calculations. This spectrum establishes a standard power density of 100 mW/cm².

Additionally, tools like SMARTS version 2.9.2 generate the American Society for Testing and Materials ASTM terrestrial reference spectra aligned with the ASTM standard G-173-03, providing crucial benchmarks for solar spectral irradiance[38]. Given that the majority of the electromagnetic spectrum falls within 380 nm to 1100 nm, photovoltaic materials are engineered to operate within this range. Consequently, (ASTM) established a consensus standard solar terrestrial spectrum in 1982, facilitating standardized performance assessments for photovoltaic applications. Standardizing the solar cell temperature at 298.15 K (25°C) provides a consistent benchmark for analysis. Considering parameters such as radiative losses from both front and rear sides of the cell, the maximum power conversion efficiency, as estimated by Shockley and Queisser, exceeds initial predictions, reaching 32.23% for semiconductors with a bandgap of 1.1 eV and 33.16% for a bandgap of 1.34 eV[39], [40].

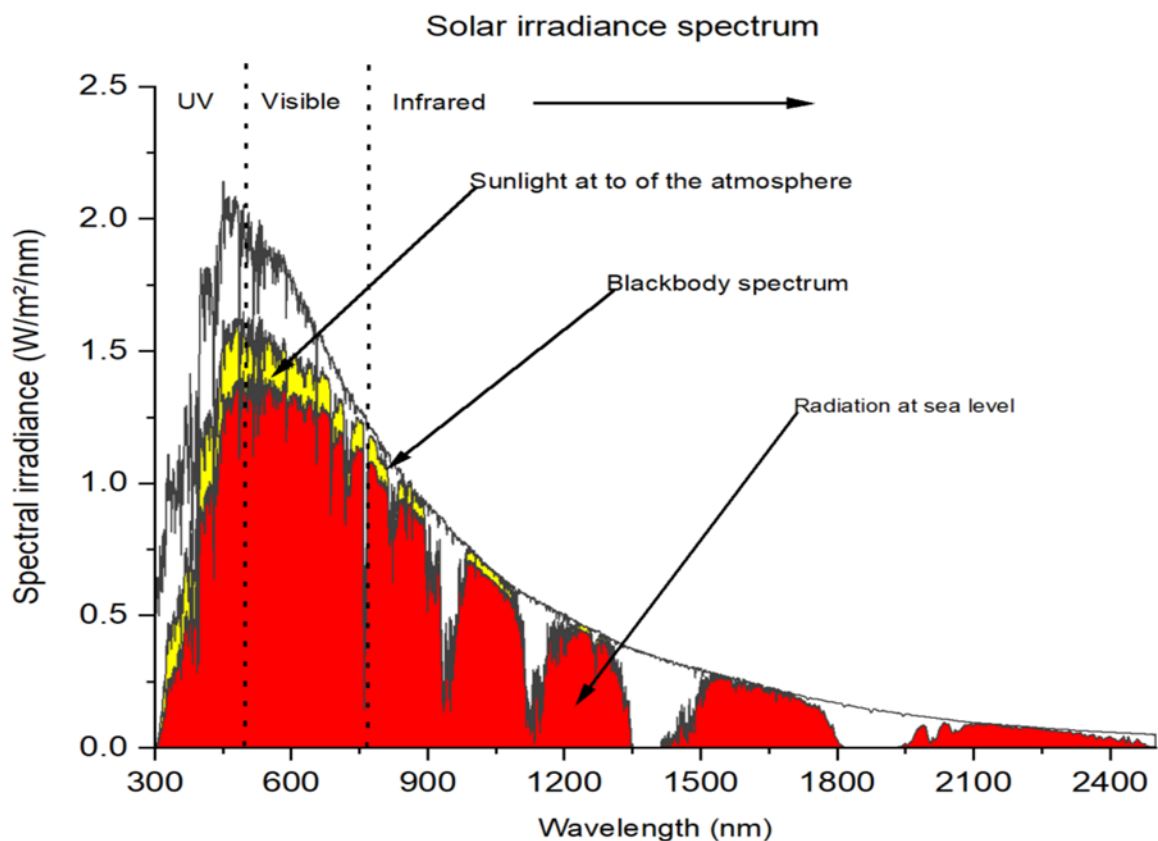


Figure 2-2 Solar irradiance spectrum above atmosphere and at surface [33]

The basic structure of the silicon solar cell which is considered as first generation typically composed of a thin wafer of silicon, which is usually less than 200 micrometres thick, and a p-n junction that separates regions of positive and negative charge. The silicon wafer is fabricated by slicing a thin layer of high-purity silicon from a larger crystal [34]. The p-n junction is created by doping the silicon wafer with impurities, which results in the formation of two regions of opposite charge. Specifically, the p-type region contains a higher concentration of positively charged impurities, while the n-type region contains a higher concentration of negatively charged impurities. [35] However the working principle of this type of the solar cells based on three primary processes of the photovoltaic effect—photon absorption, charge carrier separation, and charge carrier collection all work together to convert sunlight into electricity within a solar cell.

As shown in Figure 2-3 when sunlight (photons) strikes the surface of the solar cell, the solar cell absorbs these photons. This absorption process generates pairs of charged particles known as holes and electrons. If the energy of the absorbed photon is greater than the bandgap (E_g) of the semiconductor material in the solar cell, it excites electrons from a lower energy level (valence band) to a higher energy level (conduction band). This leaves behind a positively charged "hole" in the valence band. Furthermore, the formation of electron-hole pairs triggers the generation of an electric field at the p-n junction of the solar cell. This junction marks the boundary between the positively doped (p-type) and negatively doped (n-type) semiconductor layers. Due to the arrangement of charges and the electric field, electrons migrate towards the N-type side while holes move towards the P-type side. This spatial separation prevents the immediate recombination of electrons and holes, allowing them to move freely. Afterwards, metal contacts on the solar cell's surface collect the separated charges. Electrons are gathered by the top contact, while holes are captured by the bottom contact. These collected charges are then directed to an external electrical load for use. [36]. Furthermore these type of traditional solar cells continue dominating the solar cell market, representing a high number of global production due to their reliable performance and high effectiveness [37]. However, The cost of manufacturing solar cells remains relatively high. There is still a continuous need to research for new materials and technologies, such as organic and perovskite solar cells, in order to further improve efficiency while lowering fabrication costs.

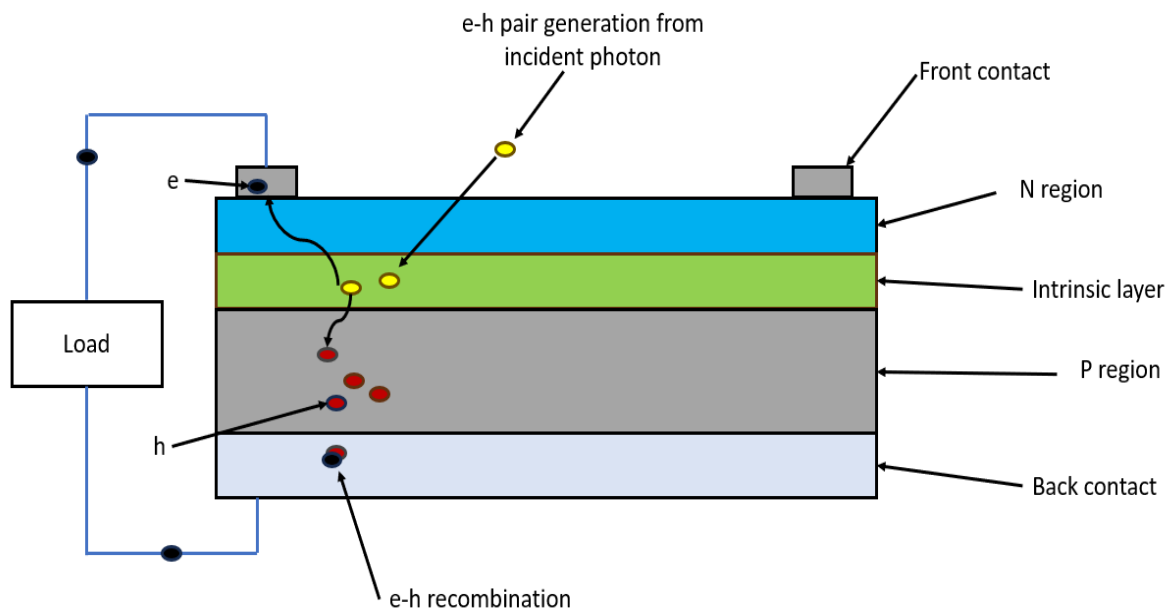


Figure 2-3 Schematic diagram of silicon solar cell with p-n junction.[46]

2.3.3 Performance evaluation of the solar cell

Performance evaluation is an important part of characterisation of the solar cells because it offers information about the performance and efficiency of solar cells. Solar cells are frequently subjected to thorough performance testing to ensure their efficiency and suitability for diverse applications. This part of the literature review outlines evaluation of several important characteristics that define the solar cell's capacity to convert sunlight into useful electrical power, which include solar cell equivalent circuit, fill factor (FF), series resistance (R_s), shunt resistance (R_p), and power conversion efficiency (PCE).

2.3.3.1 Solar cells equivalent circuit

The equivalent circuit of solar cells serves as a model that depicts solar cells through electrical circuits and discrete electrical components. As shown in Figure 2-4, it comprises a series resistance (R_s), a parallel resistance (R_{sh}), and a diode, along with a current source, representing photogenerated current. The series resistance symbolizes losses incurred due to the resistance of electrodes, interface resistances, and connecting wires. The parallel resistance signifies losses caused by current leakage across the p-n junction. If the parallel

resistance is high and the series resistance is low, it indicates that the losses in solar cells are less significant.

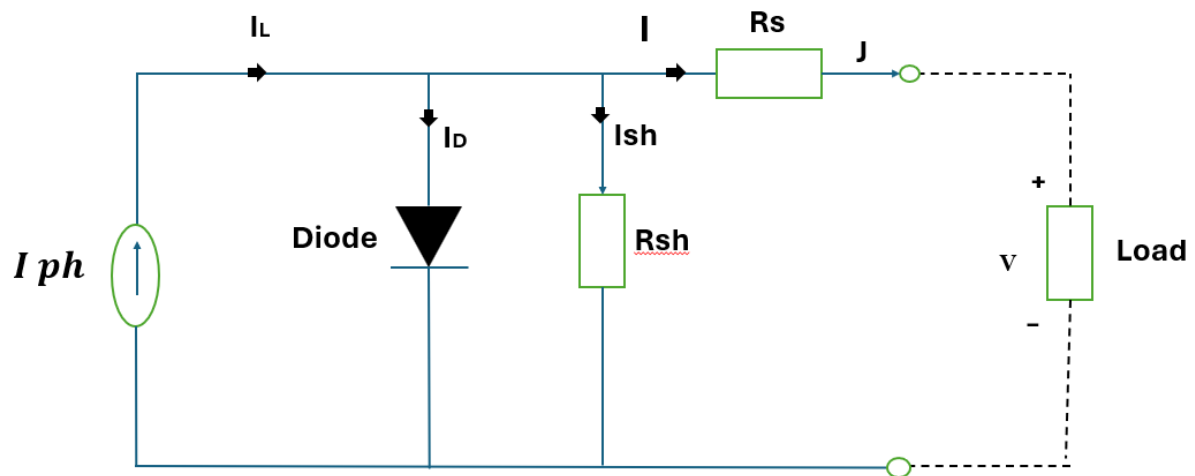


Figure 2-4 Solar cells equivalent circuit[47]

2.3.3.2 Series resistance (R_s) and shunt resistance (R_p)

Resistance represents the opposition to the flow of electric current in electrical circuits. As illustrate in Figure 2-4 the Series resistance (R_s) and shunt resistance (R_p) represent resistive and recombination losses in solar cells. A large R_s indicates a significant power consumption inside the solar cell, leading to less power delivered to the load. A small R_p represents a significant current loss due to recombination internally, resulting in a smaller current delivered to the load. Therefore, it is desirable to have a small R_s and a large R_p for an efficient solar cell 3[39] [43].

2.3.3.3 Fill factor (FF)

The fill factor (FF) represents a critical metric for quantifying solar cell performance, indicative of its efficacy in converting incident sunlight into electrical energy [38]. It is defined as the ratio of the maximum power output of a solar cell to the product of its open-circuit voltage and short-circuit current. Achieving optimal fill factor poses a significant challenge, primarily due to its sensitivity to several key parameters, including series resistance (R_s), shunt resistance (R_p), and incident light intensity[39] Extensive research efforts have been

devoted to elucidating the intricate factors governing FF, highlighting its intricate relationship with both R_s and R_p [40]. Furthermore, FF exhibits a dependency on the term $R_p/(R_p + R_s)$, with its magnitude diminishing as incident light intensity increases, attributable to heightened charge recombination dynamics [41]. Consequently, increasing the fill factor is one of the strategies to improve the power conversion efficiency of solar cells. The fill factor (FF) of a solar cell can be calculated using the following equation:

$$FF = \frac{J_m \times V_m}{J_{sc} \times V_{oc}} \dots\dots\dots \text{Equation 2-1}$$

where, J_m is the current density at maximum power point (MPP), V_m is the corresponding voltage at MPP, J_{sc} is the short-circuit current density, and V_{oc} is the open-circuit voltage.

2.3.3.4 Power conversion efficiency (PCE)

The power conversion efficiency is calculated by dividing the maximum output power supplied to a load by the incident solar radiance to the same area[45]. This efficiency is determined by three factors: the solar cell's V_{oc} , J_{sc} , and FF[45], [46]. The PCE can be calculated by testing solar cells under standard conditions, specifically the Standard Test Condition (STC)[47]. STC denotes the Air Mass (AM) 1.5 spectrum, with an incident solar power density of 100 mW/cm² and a temperature at 25°C [48]. The expression for calculating PCE from measured photovoltaic parameters is given in

$$PCE = \frac{V_m \cdot J_m}{P_{in}} = \frac{V_{oc} \cdot J_{sc} \cdot FF}{P_{in}} = \frac{P_m}{P_{in}} \dots\dots\dots \text{Equation 2-2}$$

2.4 Factors that influence the efficiency of solar cells.

The efficiency of solar cells is influenced by several factors such as the quality of the materials used, the manufacturing process, and environmental conditions. Two of the most important factors that impact the efficiency of solar cells are light intensity and temperature.

2.4.1 Irradiance intensity

The amount of sunlight that falls on a unit area is defined as irradiance intensity and plays a critical role in determining the current-voltage curve of a solar cell.

Irradiance intensity, which refers to the amount of sunlight that falls on a unit area, plays a critical role in determining the current-voltage (J-V) curve of a solar cell. When the irradiance intensity decreases, the J-V curve shifts downwards, indicating a reduction in both the short-circuit current density (J_{sc}) and open-circuit voltage (V_{oc}) of the solar cell[49]. Also, the current-voltage (J-V) curve of a solar cell is a crucial indicator of its electrical performance. where at an irradiance intensity of 1000 W m^{-2} , the IV curve of a solar cell exhibits higher J_{sc} and V_{oc} compared to the same cell under an irradiance intensity of 750 W/m^2 , 500 W/m^2 or 250 W/m^2 . As the irradiance intensity decreases, the J_{sc} decreases more rapidly than the V_{oc} , at all different irradiance intensities it can clearly be seen that the short circuit current J_{sc} is highly affected by the irradiance intensity compared to open circuit voltage V_{oc} , these factors result in a reduction in the fill factor (FF) and maximum power point (MPP). Therefore, it is important to consider the impact of irradiance intensity on the J-V curve when designing and optimizing solar cell systems[50]. Figure 2-5 illustrate effect of irradiance intensity on the J-V curves.

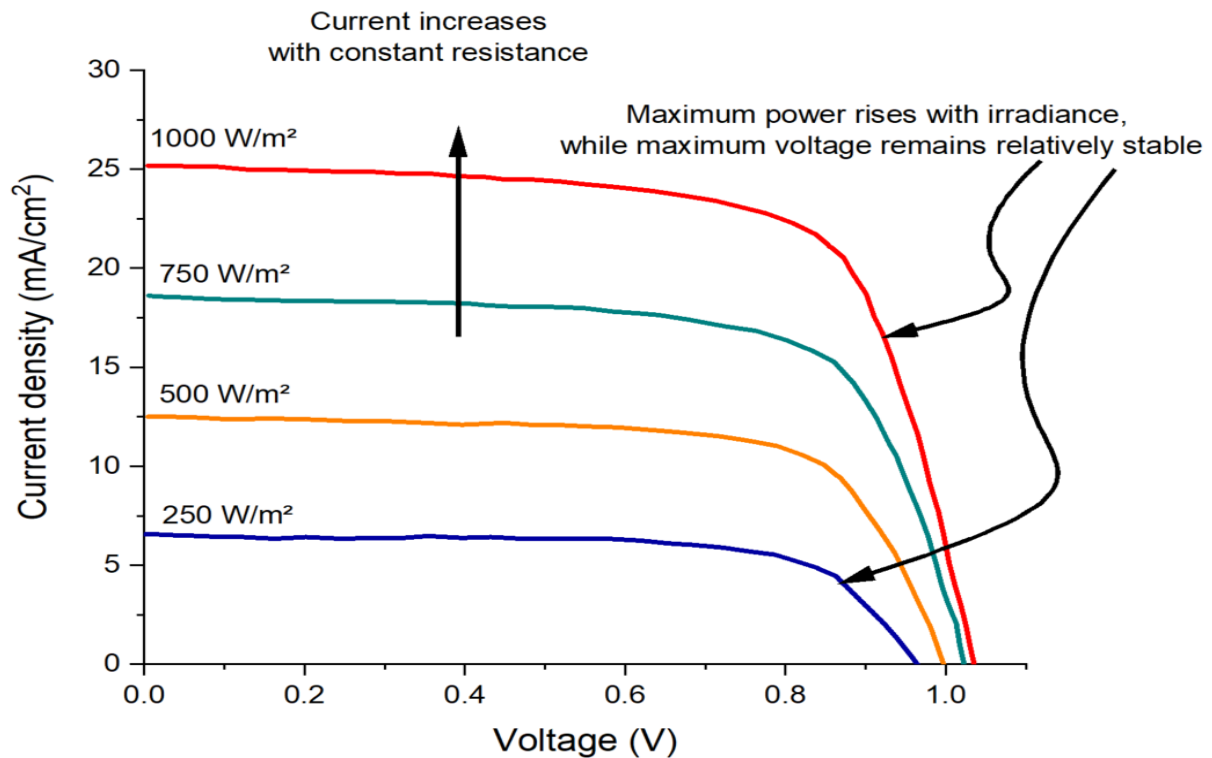


Figure 2-5 Effect of irradiance intensity on I-V curves[51]

2.4.2 Temperature

As shown in Figure 2-6 the temperature has a significant effect on the I-V curves of solar cells. As temperature rises, the operating voltage of the solar cell decreases due to the increased intrinsic carrier concentration in the semiconductor material, which reduces the intrinsic potential. [52]. Conversely, the short-circuit current (I_{sc}) typically increases with higher temperatures because of enhanced thermal generation of electron-hole pairs within the semiconductor material. [53]. Moreover, temperature variations influence the (FF) of the solar cell, with higher temperatures often leading to decreased fill factor due to increased series resistance and potential changes in shunt resistance. These changes collectively impact the overall efficiency of the solar cell. While higher temperatures may result in the reduction in voltage and fill factor, and potentially decreasing the overall efficiency of the solar cell. However, the specific impact of temperature on solar cell efficiency can vary depending on factors such as cell technology and design. Thus, understanding and mitigating these temperature effects are crucial for accurately predicting and optimizing the performance of solar energy systems across diverse environmental conditions. [54] [55].

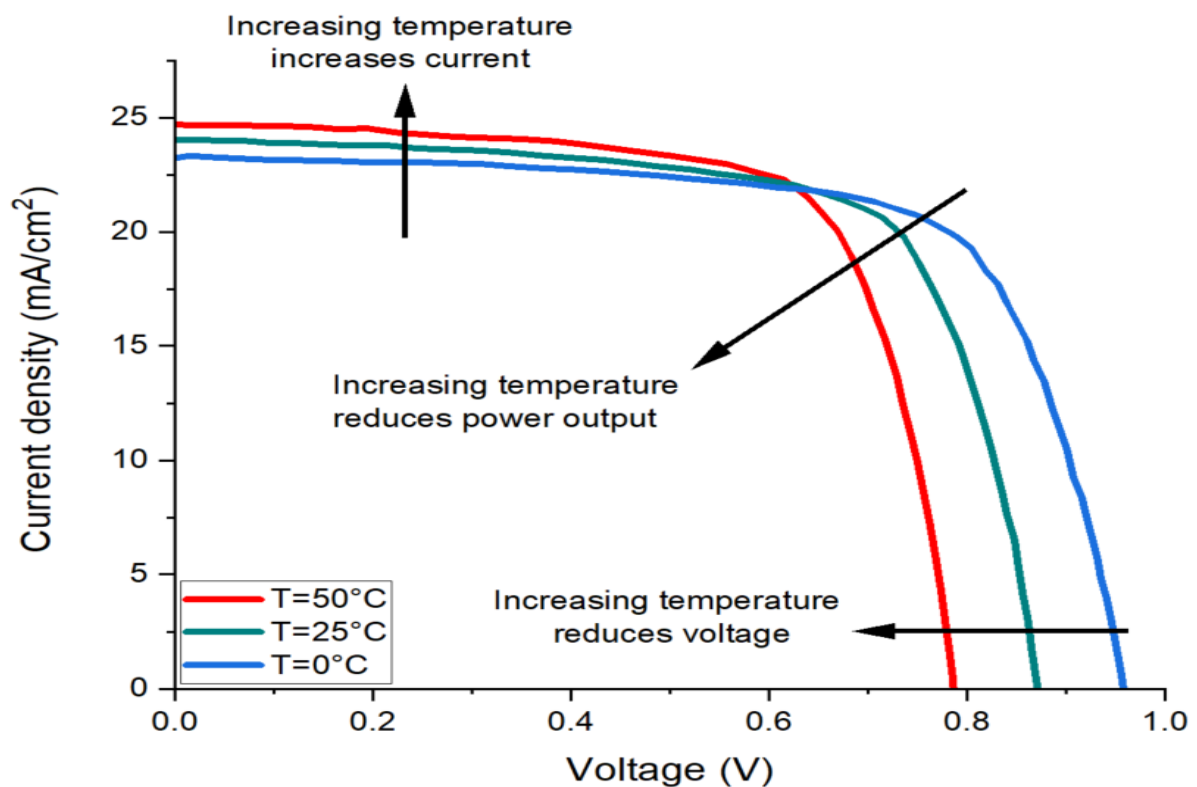


Figure 2-6 Effect of temperature on I-V curves [51]

Building on this understanding of temperature effects, the temperature coefficient (TC) provides a critical metric for evaluating the thermal stability and performance of different solar cell technologies, including perovskite solar cells (PSCs), in high-temperature environments. For example, a study by Tomoyuki Tobe et al[64]. reported that the power temperature coefficient (PTC) of PSCs is approximately $-0.44\%/^{\circ}\text{C}$ up to 85°C , indicating a 0.44% decrease in power output for every degree of temperature increase. Although this PTC is slightly worse than that of silicon solar cells, it underscores the potential of PSCs for outdoor applications due to their reasonable thermal tolerance. Furthermore, the voltage temperature coefficient (VTC) of PSCs is $-0.02\%/^{\circ}\text{C}$, and the current temperature coefficient (CTC) is $-0.06\%/^{\circ}\text{C}$, highlighting how temperature influences the electrical performance of these cells[64]. Understanding such temperature-dependent characteristics is essential for advancing solar cell technology and ensuring reliable performance in real-world applications.

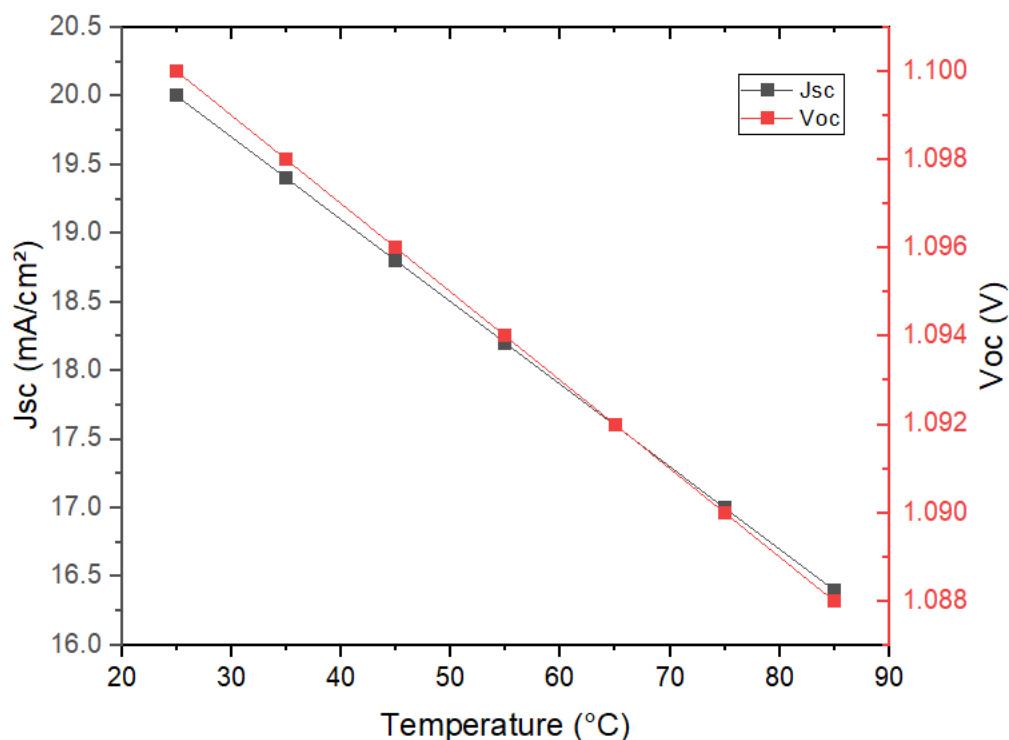


Figure 2-7 Effect of temperature Coefficients of Voc and Jsc in Perovskite Solar Cells[64]

2.5 Perovskite Solar Cells

Perovskite solar cells (PSCs), based on hybrid organic-inorganic halide perovskites, have emerged as one of the most promising photovoltaic (PV) technologies globally. Initially developed in 2009, the first PSCs achieved a power conversion efficiency (PCE) of 3.8% [56]. Subsequent breakthroughs in 2012 led to the introduction of the first solid-state PSC with a PCE of 9.7% and demonstrated long-term stability exceeding 500 hours, marking a significant advancement in PSC technology [57]. Notably, within a relatively short period, PCE has surged to 25.5%, a remarkable achievement as illustrated in Figure 2-8. However, it is important to acknowledge that these PCE records were achieved using small-scale PSCs with an active area of approximately 0.1 cm^2 [58]. Despite these advancements, commercialization of perovskite solar cells is still pending, as they remain confined to laboratory-scale production. Nonetheless, one of the principal advantages of perovskite solar cells lies in their potential for highly efficient energy conversion. By exhibiting the ability to absorb a broad spectrum of light wavelengths, these cells can attain high conversion rates and excel over other solar technologies under specific conditions[59][60]. Moreover, perovskite solar cells offer

versatility and adaptability, making them suitable for a wide array of applications. They can be fabricated into thin, lightweight films that seamlessly integrate into various products. Another significant advantage of perovskite solar cells is their lower production costs compared to traditional silicon solar cell[61]. The materials utilized in perovskite solar cells are abundant and readily available, and the manufacturing processes are notably simpler and more cost-effective than those required for silicon solar cells [62]. Consequently, perovskite solar cells present an enticing alternative for generating cost-effective renewable energy [63].

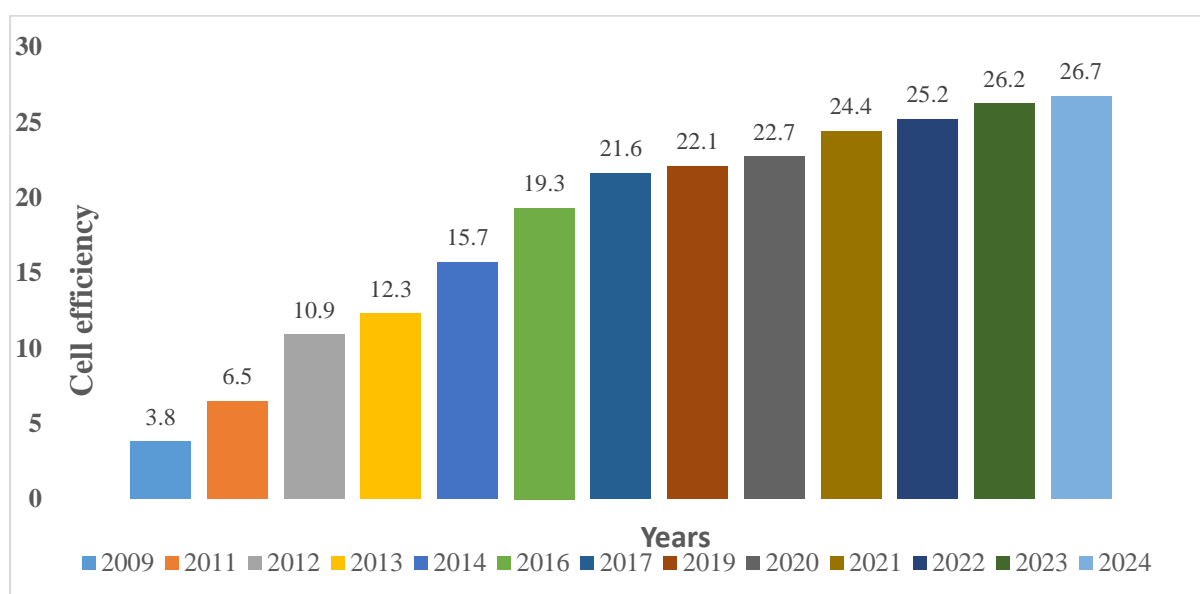


Figure 2-8 Perovskite solar cells efficiency in the years [73]

2.5.1 Structure of the perovskite solar cells

Perovskite refers to a crystal structure initially discovered in CaTiO_3 . Compounds with this perovskite structure typically adhere to the generic chemical formula of ABX_3 . In this structure, the A cation occupies the eight corners of the cubic cell, while the B cation is positioned at the body centre, surrounded by six X anions located at the face centres, thereby forming a BX_6 octahedron, as illustrated in Figure 2-9. Examples of A cations include Ca^{2+} , Cs^+ , as well as organic ions such as methylammonium (MA) and formamidinium (FA), among others. Conversely, the B site cation, usually smaller than the A cation, encompasses elements such as Ti^{4+} , Pb^{2+} , Sn^{2+} , and others. The X anion could be halide ions or oxygen. For the formation of a stable cubic perovskite structure, it is essential for the sizes of the ions to meet

a specific requirement determined by the tolerance factor (Γ), whose value should be within the range of $0.813 < \Gamma < 1.107$. The tolerance factor can be calculated from the effective ionic radii for A, B, and X ions using equation 2-3

$$\Gamma = \frac{r_A + r_X}{\sqrt{2}(r_B + r_X)} \dots\dots\dots \text{Equation 2-3}$$

where, r_A , r_B and r_X are the effective ionic radii for A, B and X ions, respectively. In the context of solar cell applications, one of the most commonly utilized perovskites is the methylammonium lead iodide (MAPbI₃). For MAPbI₃, the tolerance factor has been calculated as 0.83. This emphasizes the significance of adhering to the specific criteria for ion sizes in achieving stable perovskite structures, particularly crucial in applications like solar cells.

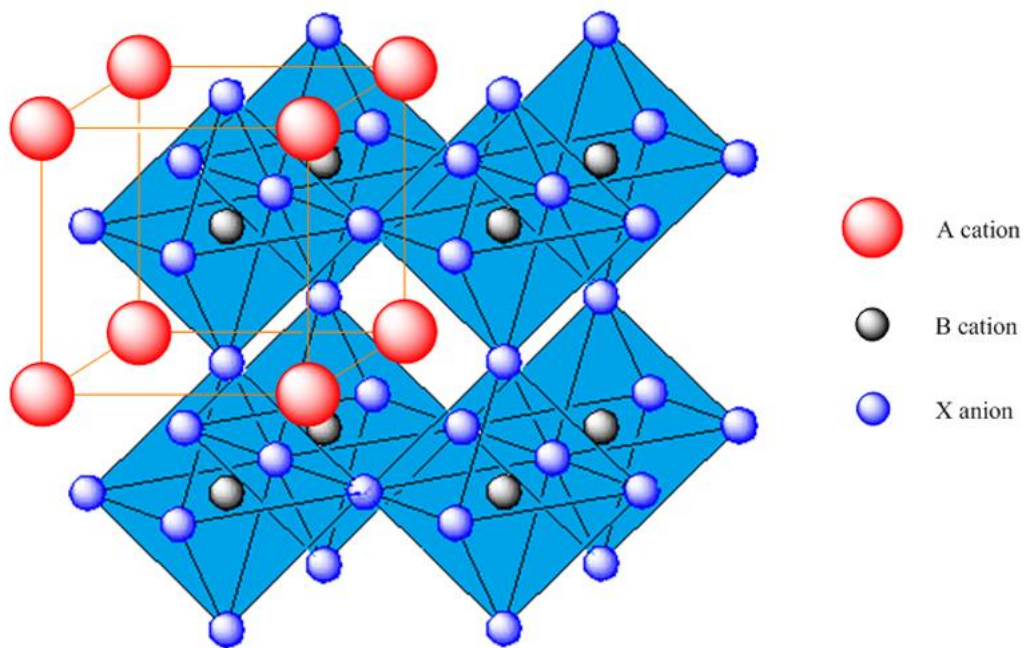


Figure 2-9 Crystal structure of perovskite ABX₃[74]

However, when fabricating perovskite solar cells (PSCs) devices, they are primarily categorized into two types: regular and planar. The planar type further divides into either n-i-p (regular planar) or p-i-n (inverted planar) type PSCs as depicted in Figure 2-10. For

the regular type, PSCs are again classified into two categories: planar and heterostructure (mesoporous)[74]. In the standard structure, PSCs comprise a fluorine-doped tin oxide (FTO) glass substrate, followed by an n-type electron transport layer (ETL), a perovskite layer, a hole transport layer (HTL), and finally, a top electrode[75]. In contrast, the inverted structure comprises an FTO glass substrate, a p-type HTL, a perovskite layer, an n-type ETL, and a top electrode[64], [65]. The perovskite layer is the most critical layer in PSCs, and its composition significantly affects the device's performance. Depending on the device's structure and performance requirements, different materials can be used for each layer[66]. For instance, for the HTL layer, 2,2',7,7'-Tetrakis [N, N-di(4-methoxyphenyl)amino]-9,9'-spirobifluorene (Spiro-OMeTAD) is commonly used in standard structure PSCs. The ETL layer can be made from materials such as Tin Dioxide (SnO_2) and Titanium Dioxide (TiO_2), while the perovskite layer's composition can vary, with materials such as methylammonium lead iodide (MAPbI_3) [66], [67] Figure 2-10 (a) shows standard structure and (b) shows the inverted structure. For high-performing perovskite solar cells (PSCs), ultra-thin perovskite films are necessary due to the absorption coefficient of the perovskite materials being between $\alpha = (10^4 \text{ to } 10^5) \text{cm}^{-1}$ [56], [68], [69]. In order to achieve high efficiency and stability, the material's properties of each layer, such as bandgap energy levels, and charge mobility, must be carefully tuned and optimised [70], [71].

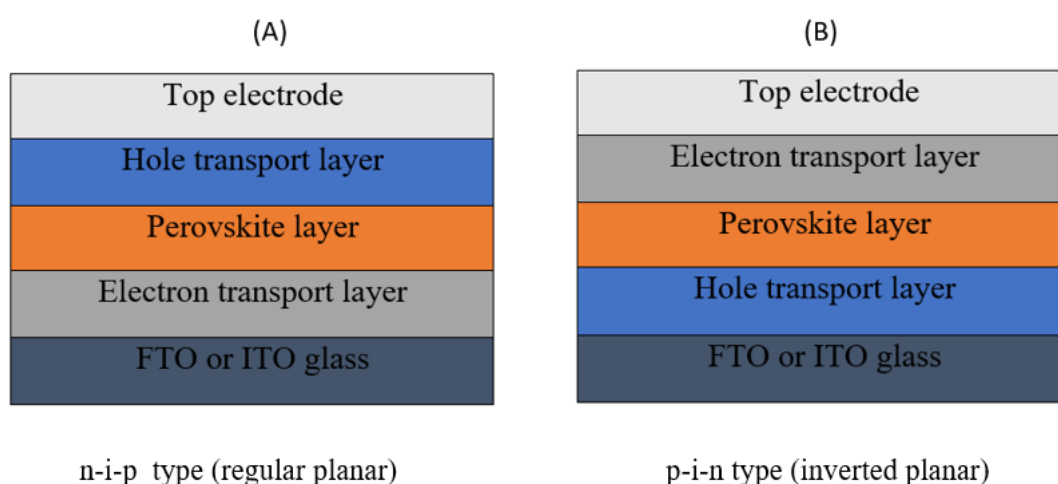


Figure 2-10 (a) Standard PSCs structure and (b) Inverted PSC structure.[84]

2.5.2 Perovskite solar cells operation principles

Perovskites possess four key characteristics that render them exceptionally suitable for application in solar cells. Firstly, they exhibit outstanding photoelectric properties characterized by low exciton binding energy and high optical absorption coefficients, reaching up to (10^4 cm^{-1}) [72], [73]. Secondly, when utilized as the light-absorbing layer in a solar cell, they efficiently capture and convert solar energy. Additionally, their large dielectric constant facilitates the effective transport and collection of both electrons and holes. Finally, perovskite materials enable the simultaneous transmission of electrons and holes over distances exceeding 100 nm, rendering them highly efficient for use in solar cells. This working principle can be simplified into fundamental steps, namely: (A) absorption of photons and generation of charges (electrons and holes), (B) transportation of charges, and (C) collection of charges [74].

These characteristics result in high open-circuit voltage and short-circuit current density when utilized in solar cell devices. Upon exposure to sunlight, the perovskite layer absorbs photons, creating electron-hole pairs. Depending on the exciton binding energy of the perovskite materials, these excitons can either produce free carriers (free electrons and holes) to generate current or recombine into excitons [75]. Due to the higher carrier mobility and low carrier recombination probabilities of perovskite materials such as $\text{CH}_3\text{NH}_3\text{PbI}_3$ (MAPbI₃), the diffusion distance and lifetime of carriers are extended, with MAPbI₃ having a diffusion distance of at least 100 nm. These extended diffusion distance and carrier lifetime contribute to the excellent performance of perovskite solar cells [76]. The free electrons and holes are then collected by an electron transport material (ETM) and a hole transport material (HTM), respectively. The electrons transfer from the perovskite material to SnO₂, used for ETM layers, and are ultimately collected by FTO, while the holes transfer to the HTM layer and are collected by the metal electrode. Finally, when an external load is connected between the FTO and metal electrodes, the generated photocurrent will flow through the outer circuit and deliver the power to the load.

The electron-hole pairs separated at the two heterojunction interfaces of SnO₂/perovskite and Spiro-OMeTAD/perovskite, followed by electrons injecting into SnO₂ (process (i) in Figure 2-11) and holes injecting into HTM (process (ii)) to achieve charges transport to the respective

electrodes. [77]. The transport processes of electrons and holes in an HTM/perovskite/ SnO₂ as shown in Figure 2-11 .

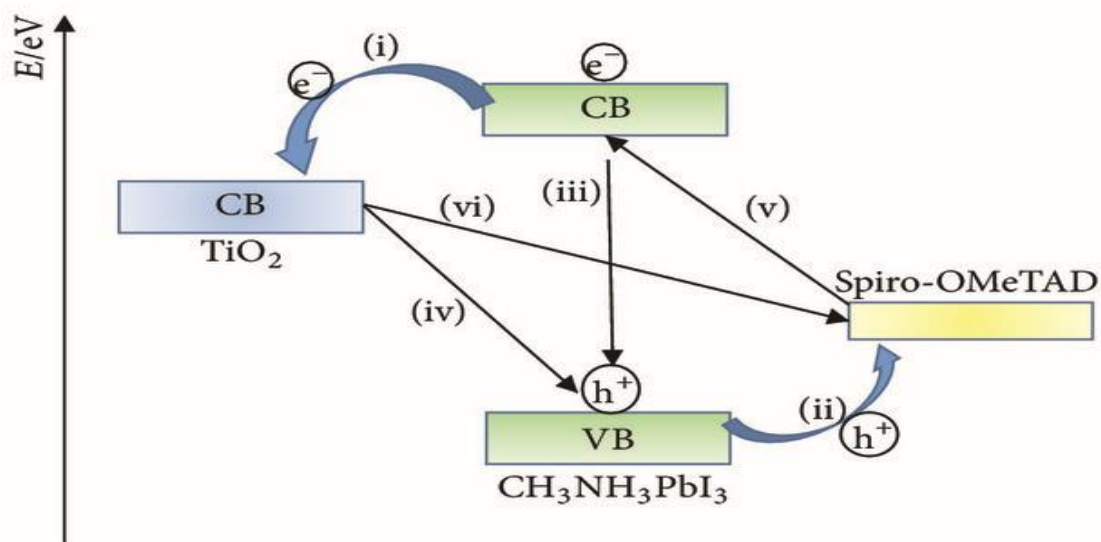


Figure 2-11 Schematic diagram of energy levels and transport processes of electrons and holes in an HTM/perovskite/SnO₂ cell[91].

2.5.3 Work function and energy band gap

The MAPbI₃ perovskite has a band gap of approximately 1.5 (eV). This band gap corresponds to an absorption onset occurring at around 800 (nm), effectively positioning MAPbI₃ as an exceptional absorber across the entire visible light spectrum. Its typical absorption coefficients are $1.5 \times 10^4 \text{ cm}^{-1}$ at 550 nm and $0.5 \times 10^4 \text{ cm}^{-1}$ at 700 nm, enabling efficient absorption even within thin perovskite films. Moreover, the high carrier mobility exhibited by MAPbI₃ perovskite adds to its appeal. With values of $11.6 \text{ cm}^2 \text{ V}^{-1} \text{ s}^{-1}$ for MAPbI_{3-x}Cl_x and approximately $8 \text{ cm}^2 \text{ V}^{-1} \text{ s}^{-1}$ for MAPbI₃, these materials facilitate the rapid movement of charge carriers within the solar cell structure. This, coupled with remarkably long carrier lifetimes measured in hundreds of nanoseconds, results in substantial carrier diffusion lengths, typically spanning from 100 nm to 1,000 nm. Such extensive diffusion

lengths significantly reduce the likelihood of carrier recombination within the bulk material, thereby enhancing the overall efficiency of the solar cell [78]–[80].

Perovskite solar cells typically use an n-i-p or p-i-n junction configuration. In this configuration, a perovskite layer acts like an intrinsic semiconductor layer between two critical layers: an n-type electron transporting layer (ETL) made of materials such as SnO₂, and a p-type hole-transporting layer (HTL) made of spiro-OMeTAD. The energy level alignment is critical in permitting efficient charge separation. Upon activation, photoelectrons are promptly injected into the TiO₂ conduction band, whereas holes are efficiently carried to the highest occupied molecular orbital (HOMO) of spiro-OMeTAD, as illustrated in Figure 2-12. This perfect separation of charge carriers significantly reduces recombination, ultimately optimising the performance and efficiency of perovskite solar cells. [80], [81].

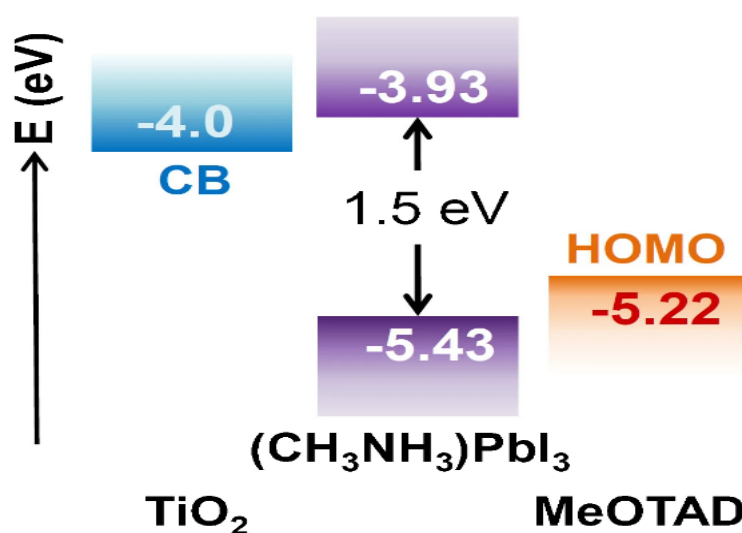


Figure 2-12 Schematic energy level diagram of TiO₂, (CH₃NH₃)PbI₃ and spiro-MeOTAD[96].

2.5.4 Impact of Humidity on Perovskite Film Properties

Understanding the complex relationship between humidity and perovskite film properties is essential for advancing the field of perovskite-based photovoltaics. Through systematic studies investigating the effects of humidity on film formation and device

performance can develop strategies to increase the efficiency and mitigate degradation mechanisms and enhance overall device durability. The influence of atmospheric humidity on perovskite deposition and device performance underscores the need for meticulous control and characterization. As depicted in Figure 2-13, the perovskite layer prepared under a nitrogen atmosphere with 0% relative humidity (RH) exhibits well-defined cubic crystallites, displaying strong connectivity among grains and grain sizes ranging from 100 to 200 nm. Conversely, the perovskite layer prepared under 40% RH displays blurred grain boundaries, likely caused by because of the high humidity during deposition and sintering. This humidity-induced effect also leads to the formation of significant gaps between crystals of the perovskite layer[97]. To address this challenge, various humidity levels were introduced during the preparation of the perovskite layer, which was deposited within a specialized glovebox. This step is significant in the broader context of perovskite fabrication but its potentially reduces the possibility of the widespread commercialization[98].

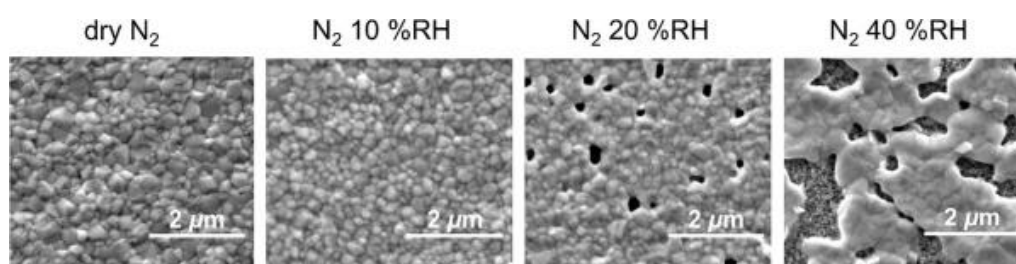


Figure 2-13 The SEM images show the perovskite layer prepared under nitrogen at 0%, 10%, 20%, and 40% RH[99].

2.6 Performance in controlled environment

In controlled environments, perovskite solar cells can perform better due to the absence of environmental factors that could degrade the material. For example, perovskite solar cells can be fabricated and tested under controlled humidity levels and temperatures to prevent moisture from affecting the performance of the cells. Also, numerous groups have worked on PSCs, and an efficiency of 25.5% has been obtained [30]. PSCs are typically manufactured in a controlled setting at a lab scale with a very small active area of 0.1 cm². It

was confirmed that perovskites are extremely sensitive to the ambient atmosphere, which includes light, moisture, and oxygen[82].

The controlled environment features have a profound impact on the performance and reliability of perovskite solar cells (PSCs). By mitigating environmental stressors such as moisture, oxygen, and temperature fluctuations, researchers can achieve efficiencies often exceeding 25%. This is because the controlled conditions help maintain the integrity and optimal electronic properties of the materials. Consistent and reproducible environments allow for precise tuning of material composition and fabrication processes, resulting in higher-quality films with fewer defects and larger grain sizes. This improvement in film quality enhances light absorption and charge transport within the cells, directly contributing to superior photovoltaic performance. Additionally, the stability of the solar cells is significantly increased, as the controlled conditions prevent degradation pathways that typically affect perovskite materials. This extended operational lifespan enhances the practical viability of these cells.

Furthermore, a controlled environment enables the optimization of the fabrication process for PSCs by adjusting parameters such as perovskite material composition, deposition methods, and annealing conditions. This optimization leads to improved film quality and larger grain sizes, which, in turn, result in higher efficiencies and better stability for PSCs. By refining fabrication processes under controlled conditions, consistent high performance and stability can be achieved. Table 2-1 contains a list of the most efficient PSCs constructed in controlled environment.

Table 2-1 List of the most efficient PSCs constructed in a controlled environment.

Year	Institute (First author affiliation)	Novelty	PSC device structure	Perovskite method	Device area(cm ²)	PCE (%)	Ref.
May-14	KRICT, Korea.	Solvent engineering	FTO/TiO ₂ /CH ₃ NH ₃ PbI ₃ /PTAA/Au	Spin-coating	0.16	16.2	[86]
Jun-15	KRICT, Korea.	intramolecular exchange	FTO/TiO ₂ /(FAPbI ₃) _{1-x} (MAPbBr ₃) _x /PTAA/Au	Spin-coating	0.16	20.1	[87]
Sep-2017	TU, Japan.	Mixed cation	FTO/TiO ₂ /meso-TiO ₂ /Cs _{0.05} (FA _{0.83} MA _{0.17}) _{0.95} Pb(I _{0.83} Br _{0.17}) ₃ /Spiro-OMeTAD/Au	Spin-coating (20–35% RH)	0.25	20.8	[88]
Jun-2017	UNIST, South Korea.	Iodide management	FTO/TiO ₂ /FAPbI ₃ /PTAA/Au	Spin-coating	0.0946	22.1	[89]
Apr-2019	CAS, China.	Surface passivation	ITO/SnO ₂ /FA _{1-x} MA _x PbI ₃ /PEAI/Spiro-OMeTAD/Au	Spin-coating	0.108	23.3	[90]

Year	Institute (First author affiliation)	Novelty	PSC device structure	Perovskite method	Device area(cm ²)	PCE (%)	Ref.
Oct-2020	UNIST, South Korea.	Reduction in lattice strain by addition of Cs, methylenediammonium in formamidinium	FTO/bl-TiO ₂ /mp-TiO ₂ /(FAPbI ₃) _{1-x} (MDA,Cs) _x /Spiro-OMeTAD or PTAA/Au	Spin-coating	0.0952	24.4	[91]

2.6.1 Advances in Power Conversion Efficiency Under Controlled Conditions

Perovskite solar cells have experienced a rapid improvement in power conversion efficiency over the past decade. In 2009, the efficiency of the first perovskite solar cell was only 3.8%, which was much lower than traditional silicon solar cells [92]. However, due to the continuous optimization of materials, device structures, and fabrication processes, the efficiency of perovskite solar cells has increased dramatically. By 2012, the efficiency had surpassed 10%, and in 2018, it reached a record-high of 24.2% [93], [94]. These improvements have made perovskite solar cells a promising candidate for large-scale photovoltaic applications.

The photovoltaic performance of perovskite solar cells (PSCs) is superior to that of their most potent competitors, including copper indium gallium selenide (CIGS), cadmium telluride (CdTe), and multi-crystalline solar cells, in terms of efficiency [58]. However, the majority of this success has been achieved at the laboratory scale, with a small active area (less than 0.1 cm²) and under tightly controlled environmental conditions [95]. To transition this technology to commercialization, several challenges must be addressed, including large-scale fabrication, processing in ambient environments, stability and high throughput solar modules, and cost-effectiveness. The most challenging aspect of ambient air fabrication of PSCs is controlling their crystal growth and morphology, mainly due to their rapid and less dense nucleation in the presence of moisture and oxygen. Therefore, understanding the influences of moisture and oxygen on the efficiency and stability of PSCs is highly desirable.

The high performance of perovskite solar cells can be attributed to the following key factors. First, developing better methods for creating high-quality perovskite materials, which are critical for achieving high efficiency. Second, device structures have been optimized to reduce recombination losses and improve charge transport [96]. Third, advanced characterization techniques have been applied to better understand for the fundamental physics and chemistry of perovskite solar cells, enabling to develop more effective strategies for improving efficiency. As a result of these factors, perovskite solar cells have achieved efficiencies of over 25%, which is comparable to traditional silicon solar cells [97].

Various solutions have been investigated to improve the power conversion efficiency of perovskite solar cells. To reduce recombination losses and increase charge transport, one method is to modify the interface between the perovskite and other layers in the device. Another approach is to adjust the perovskite material's bandgap to better fit the solar spectrum and enhance the amount of light that can be converted into electricity [98]. Finally, in order to obtain higher efficiencies beyond the limits of single junction solar cells, perovskite tandem solar cells have been developed, which combine a perovskite solar cell with other type of solar cells [99]. By continuing to develop and optimize these strategies, it is likely that perovskite solar cells will continue to improve and become increasingly competitive with traditional solar cell technologies, and Table 2-2 shoes a List of the champion PSC.

Table 2-2 List of champion perovskite solar cells.

Year	Institute (First author affiliation)	Novelty	PSC device structure	Power Conversion Efficiency (%)	Reference
Apr-2009	TU, Japan.	MAPbI ₃ and MAPbBr ₃ Perovskite compound as sensitizer	FTO/bl-TiO ₂ /mp-TiO ₂ /CH ₃ NH ₃ PbI ₃ /Redox Liquid electrolyte/Pt	3.8	[92]
Aug-2011	SKKU, South Korea.	Perovskite quantum dots	FTO/bl-TiO ₂ /mp-TiO ₂ /CH ₃ NH ₃ PbI ₃ /Redox Liquid electrolyte/Pt	6.5	[100]
Oct-2012	University of Oxford, England.	meso-superstructure Al ₂ O ₃ idea	FTO/bl-TiO ₂ /mp-Al ₂ O ₃ /CH ₃ NH ₃ PbI ₃ /Spiro-OMeTAD/Au	10.9	[101]
Mar-2013	University of Oxford, England	Low-temperature processing	FTO/bl-TiO ₂ /mp-Al ₂ O ₃ /CH ₃ NH ₃ PbI _{3-x} Cl _x /Spiro-OMeTAD/Ag	12.3	[102]
Dec-2013	University of Saskatchewan, Canada.	ZnO as ETL with no sintering for preparation of flexible PSC as well as ZnO with sintering method on hard substrates	ITO/np-ZnO/CH ₃ NH ₃ PbI ₃ /Spiro-OMeTAD/Ag	15.7	[103]

Year	Institute (First author affiliation)	Novelty	PSC device structure	Power Conversion Efficiency (%)	Reference
Jun-2014	SKKU, South Korea.	FAPbI ₃ Perovskite compound as sensitizer	FTO/bl-TiO ₂ /mp-TiO ₂ /FAPbI ₃ /Spiro-OMeTAD/Au	16.01	[104]
Aug-2014	UCLA, USA.	Interface engineering, air processed with RH30 ± 5%	ITO-PEIE/Y-TiO ₂ /CH ₃ NH ₃ PbI _{3-x} Cl _x /Spiro-OMeTAD/Au	19.3	[105]
May-2015	KRICT, South Korea.	Intramolecular exchange	FTO/bl-TiO ₂ /mp-TiO ₂ /(FAPbI ₃) _{1-x} (MAPbBr ₃) _x /PTAA/Au	20.1	[84]
Oct-2016	EPFL, Switzerland.	Incorporation of rubidium cations	FTO/bl-TiO ₂ /mp-TiO ₂ /RbCsFAMAPbI ₃ /SPIRO-OMeTAD or PTAA/Au	21.6	[106]
June-2017	NIST & KRICT, South Korea. China	Iodide management	FTO/bl-TiO ₂ /mp-TiO ₂ /FAMAPbI _{3-x} Br _x /PTAA/Au	22.1	[107]

Year	Institute (First author affiliation)	Novelty	PSC device structure	Power Conversion Efficiency (%)	Reference
Mar-2019	KRICT, South Korea & UNIST, s	P3HT as HTL	FTO/bl-TiO ₂ /mp-TiO ₂ /(FAPbI ₃) _{0.95} (MAPbBr ₃) _{0.05} /P ₃ HT/Au	22.7	[108]
Oct-2020	UNIST, South Korea.	Reduction in lattice strain by addition of Cs, methylenediammonium in formamidinium	FTO/bl-TiO ₂ /mp-TiO ₂ /(FAPbI ₃) _{1-x} (MDA, Cs) _x /Spiro-OMeTAD or PTAA/Au	24.4	
Feb-2021	MIT, USA & KRICT, South Korea	Carrier management	FTO/SnO ₂ /3D PS/2D PS/Spiro-OMeTAD/Au	25.2	[109]
Apr-2021	UNIST, South Korea & EPFL, Switzerland.	anion engineering (pseudo-halide anion formate (HCOO ⁻))	FTO/c-TiO ₂ /mp-TiO ₂ /FO-FAPbI ₃ /SPIRO-OMeTAD/Au	25.6	[110]
Jan 2022	National Renewable Energy Laboratory USA USA	NA	NA	25.7	[58]

Year	Institute (First author affiliation)	Novelty	PSC device structure	Power Conversion Efficiency (%)	Reference
Dec 2022	National Renewable Energy Laboratory USA	NA	NA	25.8	[58]

2.6.2 Factors Influencing Device Stability

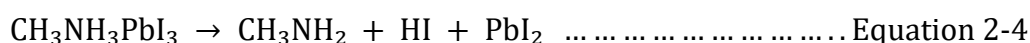
Perovskite solar cells encounter stability challenges attributed to issues like moisture, light, high temperatures, and air exposure, leading to device degradation[127]. The sources of instability include intrinsic stability problems, moisture and oxygen infiltration, and decomposition triggered by illumination. Fabricating perovskite solar cells poses challenges due to the need for a controlled environment to prevent oxygen and moisture interference. These factories have a greater impact on perovskite films than other layers such as hole and electron transport layers[128].

Using hydrophobic materials and employing effective encapsulation techniques enhance stability by impeding moisture ingress. Also, alternative materials for electron and hole transport layers to improve stability have been explored. However, achieving commercial viability necessitates simplifying the structure of perovskite solar cells without compromising their performance[129]. Various strategies have been proposed to tackle stability concerns. One approach involves employing different perovskite compositions, such as mixed bromide-iodide perovskites, which demonstrate improved resistance to moisture compared to pure iodide perovskites. Nevertheless, these compositions may experience reduced efficiency due to their wider bandgap. Enhancing stability through encapsulation methods has been investigated. While they can enhance stability under certain conditions, material degradation persists, particularly at elevated temperatures. Additives and dopants, like iridium complexes, have been explored to improve stability[130]. The choice of electrodes is another critical factor affecting perovskite device stability. Gold (Au) electrodes have been widely used due to their high efficiency, but their cost is prohibitive. because of this substituting gold with silver (Ag) paste to reduce cost. the stability poses a significant challenge for perovskite solar cells. Factors like moisture, UV light, high temperatures, and air exposure contribute to device degradation[128]. Researchers are actively exploring diverse strategies, including the use of alternative materials, encapsulation techniques, and structural modifications, to enhance stability. Achieving commercial viability necessitates streamlining the device structure while maintaining performance. Continued research and development

efforts are crucial to overcome stability limitations and unlock the full potential of perovskite solar cells[131].

2.6.2.1 Impact of Temperature

Increased temperatures also accelerate the deterioration of the perovskite layer, resulting in a decline in performance. The degradation observed at higher temperatures is associated with changes in the phase of the perovskite material [111]. Specifically, the perovskite phase shifts from orthorhombic to tetragonal at approximately 160 K, and it further transitions from tetragonal to cubic at 330 K. When exposed to temperatures above 358 K (i.e., 85 °C), the cubic phase decomposes. Equation 2-4 illustrates a potential reaction responsible for this degradation, where $\text{CH}_3\text{NH}_3\text{PbI}_3$ breaks down into CH_3NH_2 , HI, and PbI_2 . It's important to note that temperature alone does not directly impact stability, but it does accelerate the rate of this reaction [112]. The degradation occurring at 85 °C, well within the operating temperature range, is particularly concerning.



Meng et al. conducted a stability analysis on mixed-cation lead halide perovskite $(\text{FAPb}_3)_{1-x}(\text{MAPb}(\text{Br}_3 - y\text{Cl}_y))_x$ in the ambient atmosphere, examining temperatures ranging from 25 to 250 °C. The study revealed that perovskites based on methylammonium (MA) rapidly decompose into PbI_2 at higher temperatures, leading to a degradation in the power conversion efficiency (PCE) [113]. SEM imaging, energy-dispersive X-ray (EDX), and X-ray diffraction (XRD) were performed on the perovskite samples under various temperature conditions. The results indicated that the absorption edge of the perovskites redshifted due to elevated temperature, resulting in a decrease in the bandgap by approximately 3.9% (from 1.569 to 1.508 eV). Additionally, higher temperatures led to an increased density of defects. Interestingly, the authors demonstrated that even in an inert (argon) atmosphere without moisture, the degradation of perovskite led to the formation of PbI_2 when the temperature approached 100 °C.

In another study, Afroz et al. introduced an additive called oxalic acid, which possesses two bifacial carboxylic groups, into the perovskite solution during crystal growth. The authors suggested that the addition of this compound improved crystallization, resulting in perovskite crystals with larger grains, fewer surface traps, and reduced boundaries. The devices with the additive exhibited enhanced thermal stability, retaining 90% of their initial efficiency after 9 hours at 100 °C and 60% relative humidity (RH), which decreased to 70% after 19 hours. In comparison, the control device without the additive experienced a degradation in PCE to 14% within 9 hours [114].

2.6.2.2 Influence of Moisture and Oxygen

Moisture does not react directly with perovskite. However, it does act as a catalyst in degradation reactions. Niu et al. proposed a series of reactions based on X-ray diffraction (XRD) patterns, which involve the formation of H_2 that can escape, hindering the reversibility of the reactions [115]. Another pathway for perovskite layer degradation is through deprotonation, as illustrated in Figure 2-14. In this pathway, water, acting as a Lewis base, takes a proton from the perovskite, forming an intermediate complex $[(CH_3NH_3)^{n-1}(CH_3NH_2)^nPbI_3][H_3O]$, which subsequently breaks down, yielding HI, CH_3NH_2 , and PbI_2 [116]. On the other hand, the initial reaction initiates the degradation process, but the degradation of HI through the last two reactions makes the earlier reactions irreversible, compromising the lifetime of the perovskite material. Additionally, the solubility of PbI_2 formed in the initial reaction is environmentally harmful due to the high toxicity of lead [117].

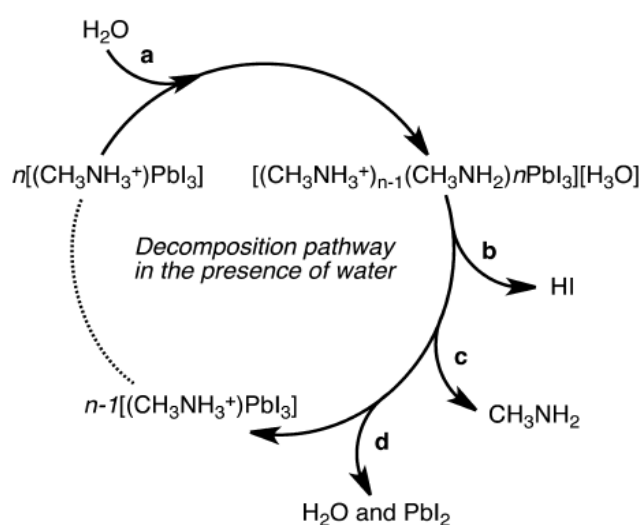


Figure 2-14 A possible degradation pathway of metal halide perovskites in presence of water [132].

The effect of relative humidity (RH) on perovskite degradation was investigated by Yang et al. using in situ absorption spectroscopy and grazing-incidence X-ray diffraction (XRD). They observed a gradual phase change and its impact on the declining power conversion efficiency (PCE) under uncontrolled RH conditions. Devices remained relatively stable up to an RH of 50%. However, at 80% and 98% RH, rapid degradation occurred, resulting in a drop in perovskite absorbance to 20% of its initial value within the first 20 hours of operation. Interestingly, an RH of 20% showed an initial increase in absorbance during the first 100 hours, although the underlying cause was not explained [118]. Controlled moisture at specific levels may participate in passivating defects in the perovskite/electron transport layer interface. Stability analysis for RH levels between 50% and 80% commonly encountered in outdoor conditions was not conducted. In recent research, Akram et al. developed a moisture-resistant structure for perovskite solar cells (PSC) by passivating the surface of the active layer of perovskite with additives to achieve a PCE of 22.25%. And Stability testing between (40-75% RH) for 600 hours showed that the devices which had additives to the active layer lost only 10% of their PCE, while the control devices experienced a 50% decrease [119].

2.6.2.3 Impact of UV Light (Photostability)

Methyl ammonium halide is the most common material used as a perovskite absorber, but it is vulnerable to moisture, temperature, and UV exposure, leading to reduced efficiency and shortened device lifetime [120]. Under UV light, perovskite solar cells (PSCs) degrade rapidly due to intense UV interaction with TiO_2 , resulting in redox reactions that decompose the perovskite layer at the heterojunction. To address this issue, various strategies have been employed, such as replacing the TiO_2 layer with alternative electron transport layers (ETL), introducing protective layers between the ETL and active layer, and using encapsulation [115].

Efforts to explore wide bandgap materials as alternatives to TiO_2 for electron transport layers (ETLs) in perovskite solar cells (PSCs) have highlighted the potential advantages of SnO_2 . Replacing TiO_2 with SnO_2 as the ETL offers significant benefits due to SnO_2 's wider bandgap, which helps reduce recombination losses and improves overall efficiency [142]. For instance,

Dong et al. investigated the microscopic carrier dynamics under UV irradiation using atomically thin transparent layers of SnO₂, demonstrating its superior performance compared to TiO₂. This highlights how SnO₂ not only enhances efficiency but also addresses some of the degradation issues associated with TiO₂, particularly under UV exposure. [121] [122]. Li et al. utilized Cesium bromide (CsBr) for interface engineering between the electron transport and perovskite absorber, effectively enhancing UV stability. However, studies have shown that encapsulated devices may degrade more quickly than non-encapsulated devices, indicating that degradation can also originate from the meso-TiO₂ layer [122], [123]

Understanding the degradation mechanisms of perovskites is complex, as several factors come into play. To gain deeper insights into UV-induced degradation, Farooq et al. investigated the degradation of MAPbI₃ devices under UV-A (310-317 nm) and UVB (360-380 nm) bands, as well as AM1.5G conditions for reference. They found that the UV-A range deteriorated the current density of the devices, regardless of the ETL layer's composition, while the UV-B range mainly affected TiO₂ devices, with a negligible effect on devices with SnO₂ [122]. Another interesting phenomenon observed during light soaking experiments is the bounce back of current density, which was attributed to the passivation of traps by PbI₂ in MAPbI₃ devices, resulting in improved charge conduction. However, prolonged exposure still leads to permanent degradation in the devices [124].

To achieve long-term stability under illumination, several researchers have demonstrated PSCs with nearly 1000 hours or more of stability and minimal performance drop. Strategies such as composition engineering and novel interfaces have been used to mitigate photo-degradation issues, along with other factors like moisture and oxygen. Encapsulation remains one of the best approaches for overall protection against external factors. [125]. Overall, addressing the various degradation factors and long-term stability are crucial steps towards the commercialization of perovskite solar cells [126]. Table 2-3 shows the improvements in PSC devices stability.

Table 2-3 List of the research efforts focusing on improving device stability

Year of publication	Structure	PCE (%)	Stability	Stability test parameters	Ref
2014	ITO glass/MAPbI ₃ /spiro OMeTAD/Ag	13.5	—	—	[127]
2015	FTO glass/MAPbI _{3-x} Cl _x /spiro-OMeTAD/Au	14.14	>70% of PCE retained	500 h, RH 20%, dark	[128]
2016	FTO glass/MAPbI ₃ :C ₇₀ /spiro-OMeTAD/Au	13.6	PCE of 7% retained	3 h, continuous light illumination (1 sun)	[129]
2017	FTO glass/MAPbI ₃ /is-2/spiro-OMeTAD/Au	14.3	No significant degradation	124 h, continuous light (AM 1.5, 1 sun)	[130]
2018	FTO glass/BCP/CsFAMA/spiro-OMeTAD/Ag	19.07	PCE retained 92.2%	500 h, continuous light (AM 1.5, 1 sun)	[131]
2018	FTO glass/MAPbI ₃ /spiro-OMeTAD/Au	12.60	PCE dropped by 4.0%	374 h, stored in the ambient environment	[132]
2019	FTO glass-TMAH/FAMA/spiro-OMeTAD/Au	20.1	PCE retained about 83%	500 h, RH 25%, 30 °C	[133]
2020	ITO glass/MAAc/MAPbI ₃ /spiro-OMeTAD/Au	21.08	PCE retained about 86%	400 h, continuous light (AM 1.5, 1 sun)	[134]
2021	TETA-GR/BCP/MAPbI ₃ :GQDs/PTAA/Au	15.72	PCE retained about 83%	500 h, ambient environment	[135]

2.6.3 Importance of Controlled Environment

The controlled environment plays a crucial role in enhancing the performance of perovskite solar cells by providing optimal conditions for their fabrication. It minimizes the impact of external factors and allows for precise control and measurement of various parameters, resulting in improved efficiency and stability. The performance of perovskite solar cells is highly influenced by the environmental conditions in which they are fabricated and operated [136], [137]. A controlled environment is necessary to provide favourable conditions for manufacturing stable and high performance devices.

Perovskite solar cells are sensitive to light intensity and spectrum, which can significantly impact their efficiency during operation [138], [139]. By regulating the light exposure during testing, it allows to analyse the influence of different light parameters on cell performance, leading to the development of strategies to enhance efficiency. However, the light control in fabrication is rarely employed and reported.

Temperature is another crucial parameter to be controlled in fabrication of perovskite solar cells, [140], [141]. The properties and stability of perovskite materials can be affected by temperature variations. Maintaining a stable temperature during the fabrication process ensures uniform deposition and crystallization of perovskite layers, resulting in improved performance. Additionally, precise temperature control during operation can enhance overall cell performance and extend the lifespan of perovskite solar cells.

In addition to light and temperature, humidity is another factor that has impact on the performance and stability of perovskite solar cells. Perovskite materials are sensitive to moisture, which can lead to degradation and reduced efficiency [142]. A controlled environment with low humidity levels mitigates the risk of moisture absorption, ensuring the stability and longevity of perovskite solar cells. By carefully controlling humidity during fabrication and storage, manufacturers can achieve consistent and reproducible performance, enhancing the reliability of perovskite solar cell technologies [143], [144]. Moreover, a controlled environment provides protection against external contaminants such as dust particles or volatile organic compounds. These contaminants can introduce defects and reduce the energy conversion efficiency of perovskite solar cells, compromising their

long-term stability. However, controlling the humidity and providing clean environment for fabrication require expensive fabrication facilities such as glovebox or clean room.

[145], [147]

2.7 Ambient Atmosphere Fabrication

The fabrication processes, have a direct impact on PSC performance and especially have a major influence on the film's properties such as shape, homogeneity, crystallinity, and phase purity. hence influencing how well the PSCs perform [148], [149]. To date, a number of approaches for producing higher-quality perovskite films have been established. Because partial film coverage could result in the formation of shunt pathways by bringing ETLs and HTLs into direct contact, the manufacturing procedure must achieve total film covering over the substrate [150]. To create an efficient PSC, the stoichiometry, grain structure, and crystallographic phase of the perovskite layer must be tightly controlled . this is because these features are largely dependent on the film deposition technique, researchers have performed substantial studies to establish the various fabrication procedures. For mass production, several film fabrication and PSC manufacturing methods including doctor blade, inkjet printing, and spin coating are used [151].

2.7.1 Issues with fabrication in uncontrolled environment

The fabrication of devices in uncontrolled ambient atmospheres presents a range of challenges, primarily stemming from contamination. This contamination has the causes a significantly undermine device performance by weakening structural formation and leading to reduce the device functions. Among the various concerns associated with uncontrolled environments, contamination has the main concern . Additionally, factors like temperature, moisture, and UV light (photostability), as explained in Section 2.6.2, contribute to the complexities of this scenario. The repercussions of these weaknesses extend to the structural integrity of devices, causing an adverse impact on both their performance and durability[152]. To ameliorate the characteristics of these devices, thermal treatment emerges as a necessary step. However, executing effective thermal treatment poses its own set of challenges, as it can inadvertently result in the degradation of perovskite film absorption. Notably,

temperatures within the range of 45 to 55 °C exhibit a notable decline in device stability [153][154].

Furthermore, the combined influence of humidity and oxygen exacerbates the degradation and instability of the perovskite film. This phenomenon is visually evident through the colour shift of the perovskite layer, transitioning from a dark brown to a light yellow colour[155]. Mitigating this issue necessitates the application of hydrophobic passivation materials. The technique, involving a spin-coating approach, significantly curtails moisture-induced degradation, thereby extending the device's longevity by over 30 days [148].

Critical to the performance of perovskite solar cell devices is the effective collection of charges, contingent on the interfacial contact between the absorber layer and charge transport layers (ETLs and HTLs) [152]. The hydrophilic nature of the absorber layer renders it sensitive to moisture absorption from its surrounding environment [153]. Also when the active layer absorbs the moisture it will cause instigate the disintegration of the absorber layer into its constituents and damages it, consequently inducing defects at both the ETL/perovskite and perovskite/HTL interfaces [153]. These imperfections in turn become sites for charge recombination, potentially entrapping charge carriers.

Addressing this challenge necessitates innovative strategies. Researchers have proposed the incorporation of a buffer layer, like Al₂O₃, between the absorber and charge transport layers, as highlighted by Qiu et al. [153]. The introduction of this buffer layer serves as a mechanism to counteract the deleterious effects of moisture absorption and interface defects[156]. Conversely, with regard to the degradation of perovskite under UV illumination, several modifications have been undertaken to enhance the layers of perovskite solar cells [157]. A notable concern arises from the common use of TiO₂ as the ETL, which can be susceptible to degradation upon exposure to UV irradiation. The interaction between UV photons and the perovskite active layer triggers the release of desorbed oxygen from vacant sites [153][158]. This, in turn, escalates charge carrier recombination, precipitating poor device performance characterized by diminished (FF) and (V_{oc}). The intricate interplay of these factors significantly influences overall device performance[159][160].

2.7.2 Strategies to improve device efficiency in ambient atmosphere fabrication.

Various strategies have been developed to enhance device performance under these conditions. Additive engineering involves integrating specific additives into perovskite precursor solutions, such as pseudohalides, to reduce defect densities and enhance crystallinity, thereby improving device stability and efficiency [182]. Solvent engineering, which includes using solvent mixtures and anti-solvents, enables controlled crystallization, leading to films with larger and more uniform crystalline grains, crucial for optimal photovoltaic properties [183]. Surface passivation techniques, which entail applying protective layers like polymers and metal oxides, help alleviate degradation by bonding with surface defects and reducing recombination losses [184]. Interface engineering focuses on optimizing charge transport by selecting suitable materials and aligning energy levels between layers to minimize recombination and enhance charge extraction [185]. Additionally, optimizing fabrication conditions, such as controlling humidity and temperature during film formation, has been demonstrated to significantly enhance film quality and device stability [186]. These strategies collectively address the intrinsic and extrinsic factors affecting PSCs, enabling the production of more robust and efficient devices in ambient environments, thus advancing their potential for commercial deployment.

2.7.3 Recent progress and performance in ambient atmosphere fabrication

The capability to fabricate perovskite solar cells in open environments has practical significance because it allows reduction of fabrication cost. Due to the presence of moisture and oxygen, the quality of perovskite films fabricated in ambient air are usually poor. Several techniques and approaches have been explored to improve the film quality. Rong et al demonstrated an improvement in the perovskite film quality using ammonium chloride (NH_4Cl) as additive to decrease the moisture effect and slowdown the rapid non-uniform nucleation. The addition of (NH_4Cl) has reduced the quick non-uniform nucleation during the solvent evaporation, and obtained an efficiency of 15.6% with stability of 130 days under RH 30 % [167]. Wang et al studied the impact of different environments on the stability and quality of perovskite films during thermal annealing stage. They fabricated perovskite films in

two different environments: one in air with RH of 50% and one in vacuum, using one step method with thermal annealing[168]. They discovered that the thermal annealing in vacuum produced a better quality film, which resulted in an increase of 45% in terms of the performance of PSCs devices. Compared to air-processed counterparts, the enhancement is mostly due to faster solvent evaporation in vacuum. Figure 2-15 shows SEM images of perovskite crystal growth, and Figure 2-16 SEM images of perovskite films annealed in (a) air, and (b) in vacuum[169]

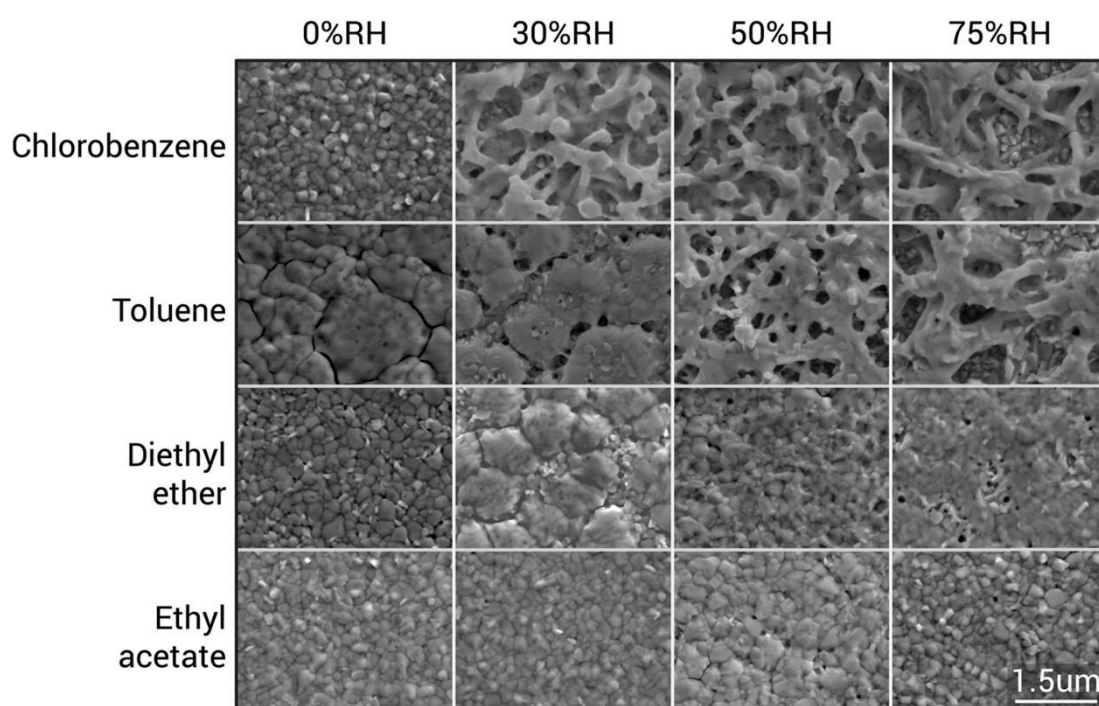


Figure 2-15 SEM images of $\text{CH}_3\text{NH}_3\text{PbI}_3$ perovskite films were analyzed after spin-coating and annealing at 0%, 30%, 50%, and 75% relative humidity. Films at 0% RH were processed in a nitrogen-filled glovebox, with different antisolvents used during spin-coating[190]

Wang et al. also demonstrated in another study that the interface engineering using the carbon graphite-based perovskite where an increase in interface contact, thus improved charge transport between layers and reduced charge recombination as well as they obtained 14.78% efficiency and device stability by more than 300 days. It is worth noting that the active layer has been made in air. [170].

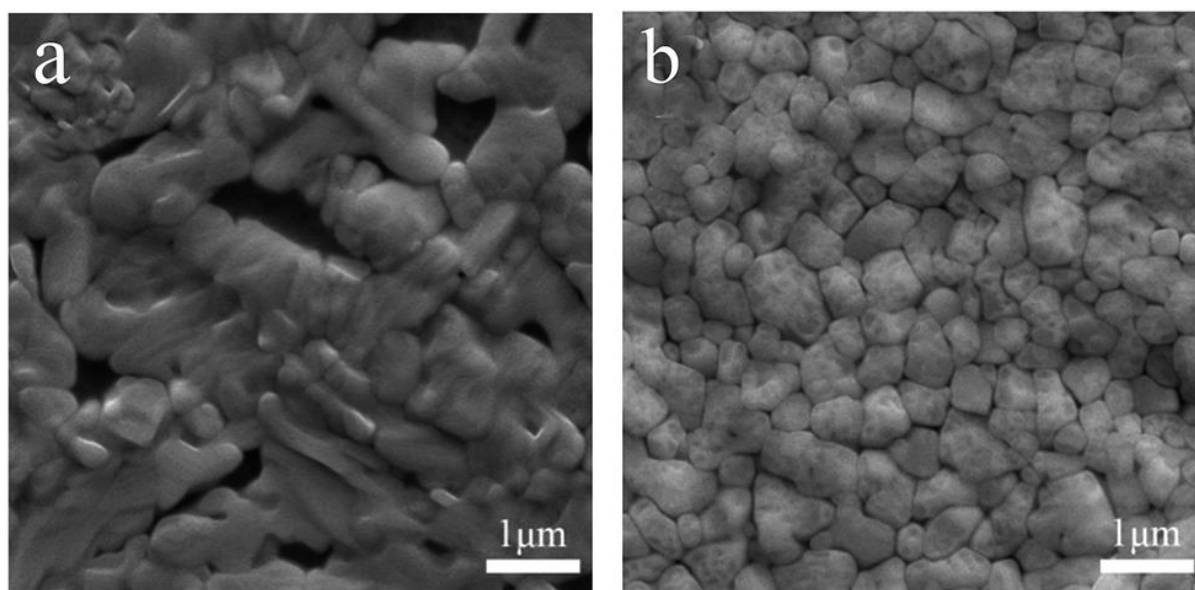


Figure 2-16 SEM images of perovskite films annealed in ambient air (a) and (b) in vacuum [190].

Several techniques have been reported to avoid non-uniform morphology of the perovskite films by using solvent and antisolvent. Huang et al used chlorobenzene (CB) as a solvent in fabrication in air with RH of 35%, which resulted in less grain boundaries and increased current density, and consequently an improved efficiency of 14.55% [173]. Fu Yang et al used the acetate-based solvents (MA, EA, PA, BA) as the antisolvents to fabricate MAPbI_3 based perovskite solar cells under high humidity. The best efficiency of 16.3% was achieved with MA-treated perovskite films. The experiments also reveal that improved stability was gained with MA-treated devices, which retained over 80% for 360 hours of performance [193]. Troughton et al investigated the effect of four different antisolvents (ethyl acetate, diethyl acetate, toluene, and chlorobenzene) on the perovskite film quality in the ambient environment of high relative humidity. They examined the morphology and crystallisation of antisolvent treated perovskite films using scanning electron microscopy and observed that the ethyl acetate performed the best among these four antisolvents, even at high RH [175]. and a study done by Tingting Zhong et al demonstrates that using potassium iodide (KI) as an additive and optimized interface engineering significantly improved the performance and stability of (PSCs) fabricated in ambient air. A (PCE) of over 18.41% was achieved, and devices retained 90% of their efficiency after 1000 hours of operation under standard conditions [195]. However, Pengchi Liu et al.'s study introduces a novel ionic liquid, 1-butyl-3-

methylpyridine thiocyanate (BPySCN), to overcome moisture interference and poor crystallization in the scalable ambient fabrication of flexible perovskite solar cells (F-PSCs). By improving nucleation dynamics and passivating defects, BPySCN enables F-PSCs to achieve impressive efficiencies of 23.01% on flexible substrates and 23.70% on rigid substrates (0.09 cm²). Additionally, these cells maintained over 90% efficiency after 500 hours at 85°C and 600 hours under 85% humidity, demonstrating enhanced durability and stability[196]. Table 2-4 provides a list of PSCs produced in ambient environments at different humidity conditions.

Table 2-4 List of the perovskite solar cells fabricated in ambient air.

Year	Institute (First author affiliation)	Novelty	PSC device structure	Perovskite method	Device area(cm ²)	PCE (%)	Ref.
Sep-14	IISER	Air-processed PSC	FTO/TiO ₂ /CH ₃ NH ₃ PbI _{3-x} Cl _x /P3HT/Ag	Spin-coating (50% RH)	0.09	5.67	[176]
Jan-15	HUT, China.	low-pressure chemical vapor deposition	FTO/TiO ₂ /CH ₃ NH ₃ PbI ₃ /Spiro-OMeTAD/Ag	Low-pressure chemical vapor deposition (RH 60%)	0.12	12.73	[177]
Aug-16	ZJU, China.	Various solvents ambience fabrication	FTO/TiO ₂ /CH ₃ NH ₃ PbI ₃ /Spiro-OMeTAD/Au	Spin-coating (35% RH)	0.1256	14.55	[178]
Apr-18	NTUST, Taiwan.	nanoparticle-induced fast nucleation (NIFN) method	ITO/ZnO/CH ₃ NH ₃ PbI ₃ /Spiro-OMeTAD/Ag	Spin-coating (55–65% RH)	0.04	18.34	[179]
Feb-19	CSU, China.	Substrate-Heating-Assisted Deposition	ITO/SnO ₂ /Cs _{0.21} FA _{0.56} MA _{0.23} (I _{0.98} Br _{0.02}) ₃ /Spiro-OMeTAD/Ag	Spin-coating (40% RH)	0.09	18.38	[180]

Year	Institute (First author affiliation)	Novelty	PSC device structure	Perovskite method	Device area(cm ²)	PCE (%)	Ref.
Feb-18	Kyushu Institute of Technology, Japan	Air Knife-Assisted Recrystallization Method	FTO /SnO ₂ /MAPbI ₃ /Spiro-OMeTAD/Ag	Air-blading (60% RH)	0.1	16.30	[174]
Feb-19	CAS, China.	Air blading for high-efficiency PSC	ITO/SnO ₂ /MAPbI ₃ /Spiro-OMeTAD/Au	Air blading	0.09	20.08	[181]
Feb-21	MIT, USA & KRICT, South Korea,	Carrier management	FTO/SnO ₂ /3D PS/2D PS/Spiro-OMeTAD/Au	Spin-coating (40 ± 10% RH)	0.09	25.20	[182]
Dec-22	School of Science, University of Geosciences Beijing, China	Use of urea additives for interface engineering	FTO/C-TiO ₂ /MTiO ₂ /FAxMA1-xPblyBr3-y/Spiro-OMeTAD/Ag	spin-coating (20–30% RH)		18.41%	[183]

2.8 Summary

The chapter provides a brief review on the importance of renewable energy sources and the significance in developing renewable energy systems to address various challenges from energy supply reliability to environmental protection, and sustainable development. It also outlines the basic knowledge of the solar cells that are crucial to this study, which includes the structure and working principle of solar cells, p-n junction, performance parameters, and methods for evaluation. The focus is then given on the perovskite solar cells (PSCs), covering initial development, the state-of-art performance and issues for further research. The fabrication of perovskite solar cells in controlled and uncontrolled environments and their impact on the efficiency and stability of the device were discussed. The current approaches, together with their advantages and challenges, of PSC fabrication in ambient atmosphere are summarised.

Chapter 3: Methodology and Experimental procedure

3.1 Introduction

This chapter provides an overview of the procedures involved in the preparation of perovskite solar cells (PSCs) as well as the measurement techniques employed for characterization purposes. The following sections detail each step of the process, starting from the cleaning of FTO glasses to the preparation of various essential components such as electron transport layers, perovskite layers, hole transport layers, and top electrodes. Furthermore, this chapter delves into the discussion of the equipment utilized for both solar cell assembly and film characterization.

3.2 Structure and experimental procedure of a perovskite solar cell

In this project, a specific solar cell structure is employed as depicted in Figure 3-1. This structure was originally reported in a study conducted by Yang [174] which is consisting of the following layers:

1. **FTO glass:** A transparent conducting material fluorine-doped tin oxide (FTO) is used at the base. This layer functions as an electrode for collecting electrons as well as a media through which incident light can pass, ensuring maximal light absorption by photoactive layers.
2. **Electron Transport Layer:** A tin oxide (SnO_2) layer is used as an electron transport layer immediately above the FTO layer. Its principal function is to ensure efficient movement of electrons generated by light absorption, directing them to the bottom electrode, but stop the holes.
3. **Perovskite Layer:** A perovskite layer (MAPbI_3 in this study) is used as the light-absorbing component, this layer is responsible for the creation of electrons and holes upon the absorption of incoming photons.
4. **Hole Transport Layer:** A spiro-OMETAD layer is used as the hole transport layer. Its primary function is to transport positively charged holes to the top electrode, but stop electrons to pass.

5. **Top Electrode:** A top electrode which is a silver (Ag) layer in this study plays an essential role as the positive electrode where the holes are collected from the solar cell and delivered to the electric load of the external circuit.

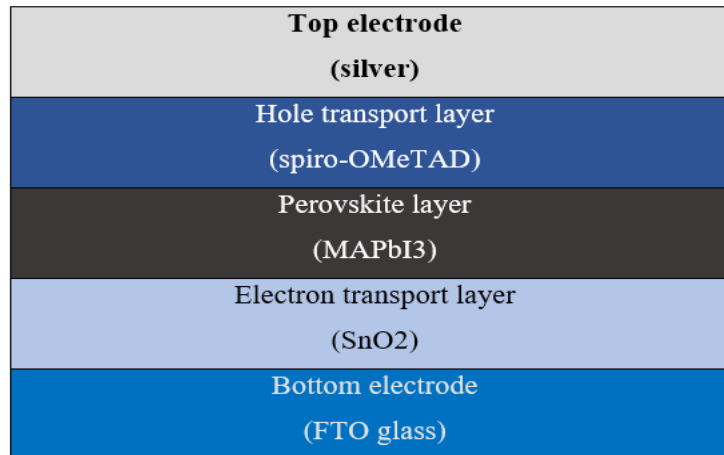


Figure 3-1 Structure of the perovskite solar cell

3.3 Preparation of the materials and device

The perovskite solar cells for this study were fabricated following the procedures shown in Figure 3-2. The materials for the perovskite solar cell are prepared as follows: A transparent conductive SnO₂ layer is deposited onto a commercially available FTO glass substrate using techniques such as spin-coating or chemical vapor deposition. The perovskite active layer (MAPbI₃) is created by mixing lead iodide (PbI₂) and methylammonium iodide (MAI) solutions, which are then deposited onto the SnO₂ layer and subjected to annealing. The hole transport layer (Spiro-OMeTAD) is applied by spin-coating using a Spiro-OMeTAD solution with additives. Finally, a thin layer of silver (Ag) is sputter-deposited on top.

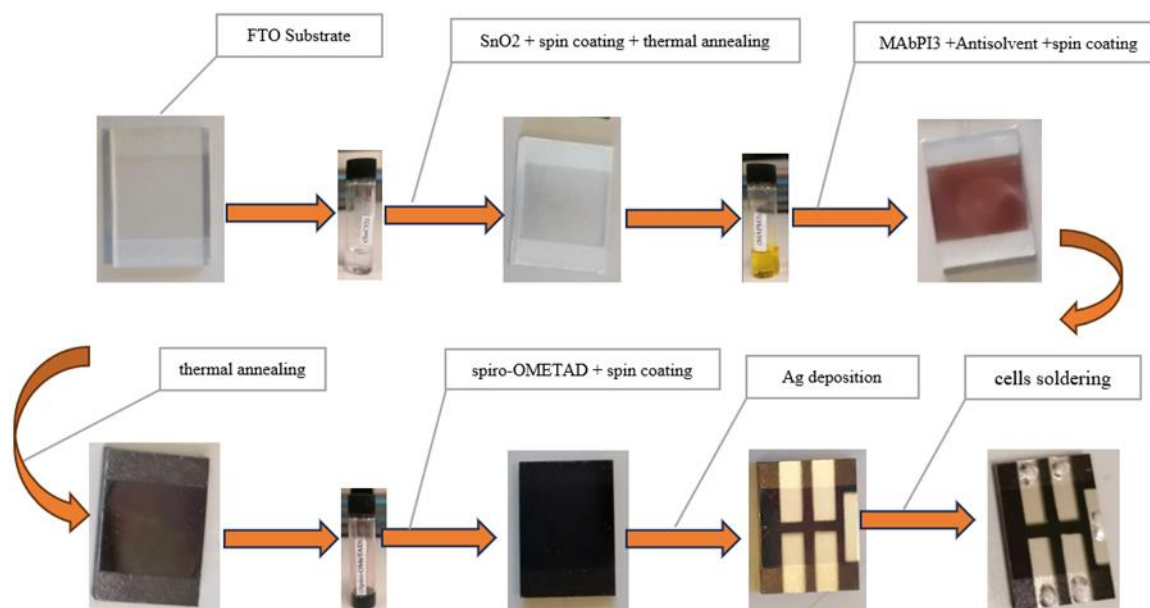


Figure 3-2 sequential deposition process that starts from the initial stages and progresses to complete device fabrication

3.3.1 Fluorine-doped Tin Oxide Glass Substrate (FTO)

Fluorine-doped tin oxide (FTO) glass substrates used in this study were TEC-15 supplied by XOP GLASS Co. Ltd, with the following dimensions: length (L) 20mm, width (W) 15mm, and thickness (T) 2.2mm. The conductive area on each substrate was $12 \times 15 \text{ mm}^2$, located in the centre of the substrate. Figure 3-3 (a) and (b) show the schematic and photograph of the purchased FTO substrate, respectively.

In order to achieve a high-quality interface between the device layers and the FTO substrate, a meticulous cleaning process was undertaken. This process began with a thorough scrubbing using a brush and a diluted Hellmanex (III) solution, followed by a rise in deionized water. Subsequently, the FTO glasses underwent a sonication process in deionized water, acetone, and isopropanol at 50°C for a duration of 10 minutes, employing an ultrasonic bath (Allendale ultrasonic bath, US-CU-DI-9L). Afterwards, the FTO glasses were subjected to nitrogen gas drying before being placed into an ultraviolet (UV)-ozone cleaner (Ossila UV-ozone cleaner, L2002A2-UK) for a 10-minute treatment. This UV-ozone treatment served to enhance the substrate's surface energy and remove a wide exhibit of contaminants, including

organic molecules, grease, and residual chemicals. Figure 3-3 (c) and (d) show a ultrasound bath and UV-ozone cleaner used in these procedures, respectively. The meticulous execution of these cleaning steps proved to be important to ensure good charge transport and reduce recombination, ultimately affecting the efficiency and stability of the perovskite solar cells. The correct and accurate execution of these cleanings is an initial and crucial fabrication step to ensure successful fabrication of perovskite solar cells.

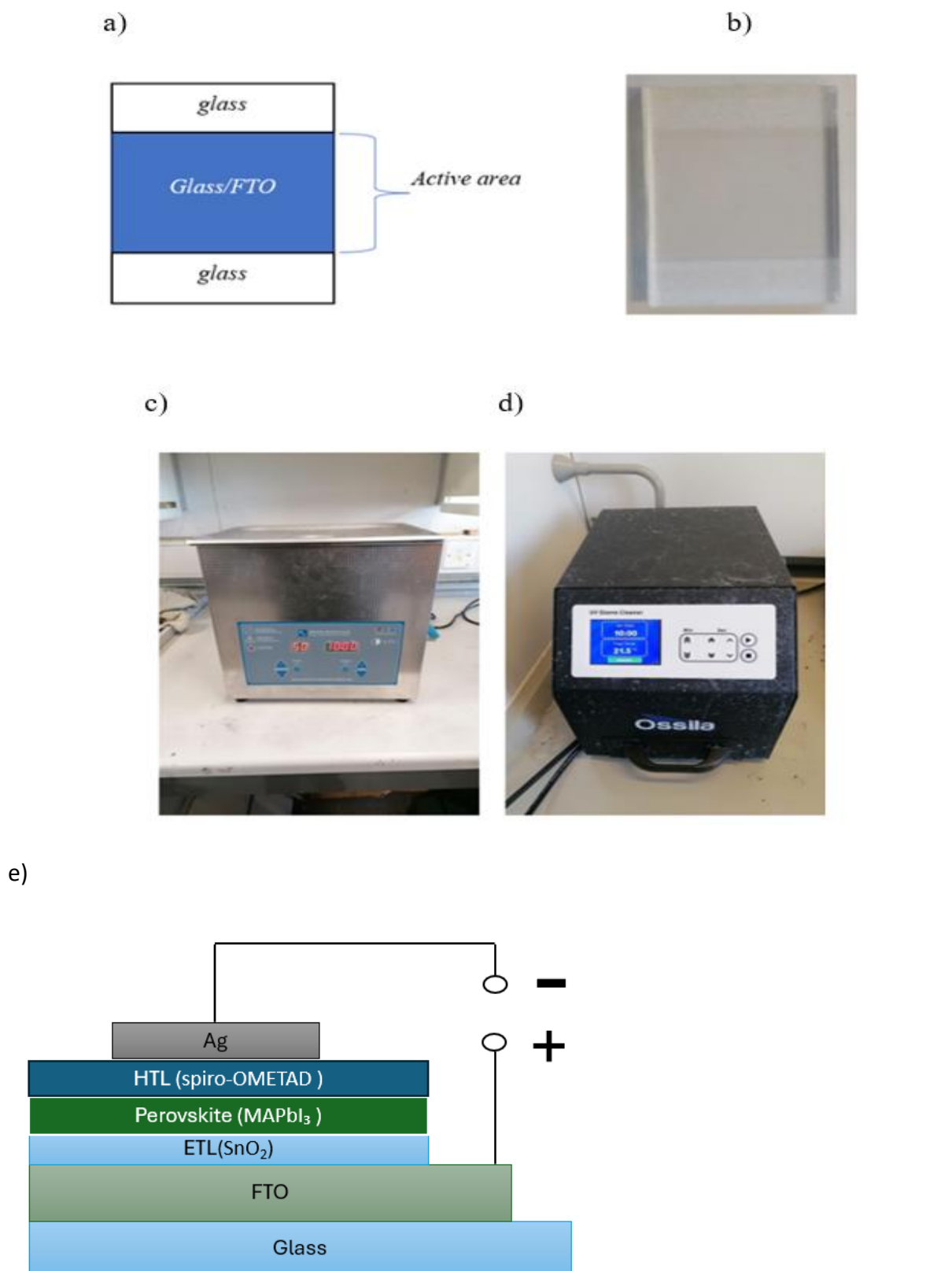


Figure 3-3 a) Schematic diagram showing the design of FTO substrate, (b) Photograph of FTO substrate, (c) Ultrasound bath and (d) UV-ozone cleaner, e) Schematic diagram of the completed device structure of perovskite solar cells.

Steps for Extracting Key Parameters from a JV Curve

Here are the detailed procedures for extracting the values of **PCE**, **JSC**, **VOC**, **FF**, **Pmax**, **RS**, and **RSh** from a typical JV curve:

- **VOC (Open-Circuit Voltage)**: Identify the voltage where the current is zero on the JV curve.
- **JSC (Short-Circuit Current Density)**: Locate the point where the voltage is zero, and take the corresponding current density as JSC.
- **Fill Factor (FF)**: Calculate FF using the formula:
$$FF = \frac{P_{max}}{J_{sc} \times V_{oc}} \times 100$$
- **Pmax (Maximum Power)**: Find the point on the JV curve where the product of voltage and current is maximum.
- **Series Resistance (RS)**: Measure the slope of the JV curve near V_{oc} (flat region at high voltage).
- **Shunt Resistance (RSH)**: Measure the slope of the JV curve near J_{sc} (steep region near zero voltage).
- **PCE (Power Conversion Efficiency)**: Use the formula:
$$PCE = \frac{P_{max}}{P_{in}} \times 100$$
- Here, P_{in} is the incident light power density, usually 100 mW/cm²

3.3.2 Electron transport layer (SnO₂)

To fabricate SnO₂ layers, a solution was prepared using tin (II) chloride dihydrate (SnCl₂·2H₂O, 99.995%) obtained from Sigma Aldrich and dissolved in absolute ethanol from Fisher Scientific. The synthesis process involved dissolving 15 mg of SnCl₂·2H₂O in 1ml of absolute ethanol, followed by stirring the mixture at 450 rpm and maintaining a temperature of 45°C using a Corning Hot Plate Stirrer, Glass Ceramic. This stirring process was carried out for 2 hours to ensure proper homogenization. Subsequently, the solution was filtered through a 0.45 μl syringe filter to remove any impurities.

After the filtration, a volume of 90 μl of the $\text{SnCl}_2 \cdot 2\text{H}_2\text{O}$ solution was spin-coated onto a FTO substrate at a speed of 4000 rpm for precisely 30 seconds using the Laurell spin-coater (WS-650HZ-23NPPB) as shown in Figure 3-4 (a). The FTO/ $\text{SnCl}_2 \cdot 2\text{H}_2\text{O}$ coated films were then subjected to a controlled heating process. As shown in Figure 3-4 (b), the films were carefully heated to 70°C using a Corning Hot Plate Stirrer, Glass Ceramic. This heating procedure was conducted under the cover of a petri dish to ensure uniform heating across the films. Following this, the films were annealed at a temperature of 180°C for a duration of 60 minutes, aiming to form a dense and compact SnO_2 layer.

After the annealing process, the samples were gradually cooled to a temperature of 60°C before carefully removing them from the hotplate. The next step involved subjecting the fabricated SnO_2 layers to a 10-minutes treatment in a UV-ozone cleaner. This treatment step was crucial to prepare the surface before depositing the perovskite layer, enhancing the subsequent layer's union and overall performance. Figure 3-4(c) and (d) show the SnCl_2 solution and the SnO_2 coated FTO glass, respectively.

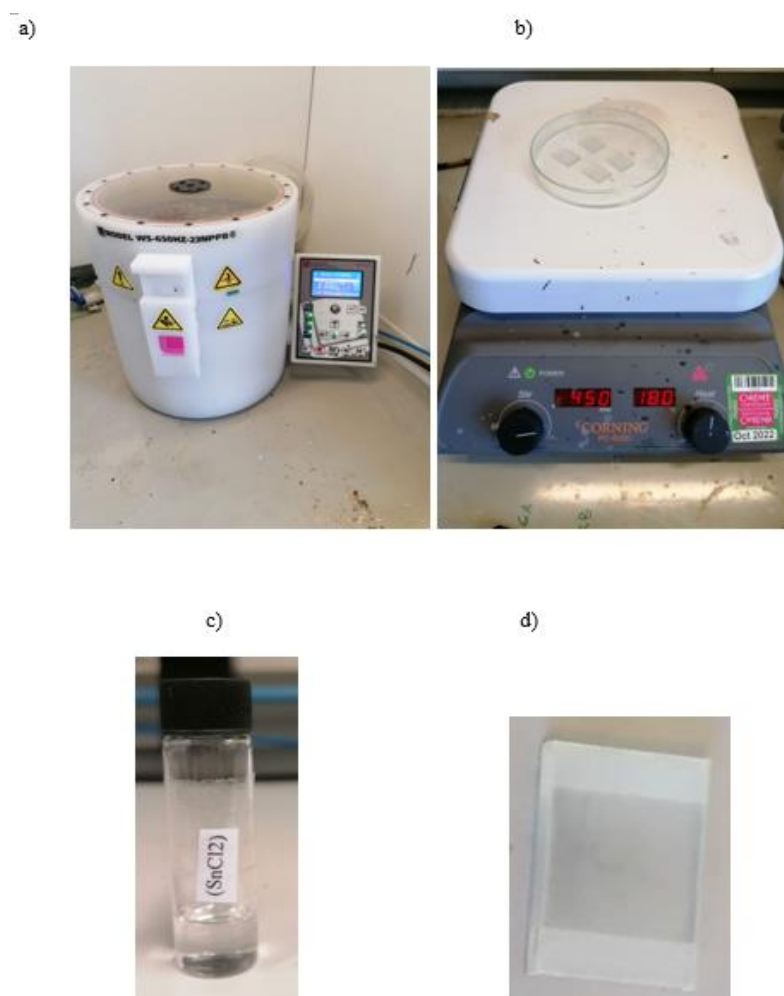


Figure 3-4 a) Laurell spin-coater used for this research, b) Annealing of the SnO_2 coated FTO substrate in a petri dish, c) SnCl_2 solution, and d) FTO glass coated with SnO_2 layer after annealing.

3.3.3 Perovskite active layer (MAPbI_3)

In the fabrication of the Perovskite active layer (MAPbI_3), the following materials were employed: lead (II) iodide (PbI_2 , 99.999%, molar mass of 461 g/mol) procured from Alfa Aesar and methylammonium iodide (MAI, 99%, molar mass of 159 g/mol) purchased from Sigma Aldrich. Solvents were a crucial part of this process, with dimethylformamide (DMF, 99.8%, 720 mg) from Across organics, and dimethyl sulfoxide (DMSO, 99.8%, 240 mg) from Alfa Aesar. Additionally, an volume of 800 μL DMF and 200 μL of DMSO were mixed as part of the solvent composition. For antisolvents, methyl acetate (99%) from Across organics, toluene from Fisher Scientific, ethanol from Fisher Scientific, methyl format and Chlorobenzene (99.6%) from Across organics were employed. Further details regarding the

use of these additives can be found in Chapters 4 and 5. The incorporation of antisolvent additives into the MAPbI₃ layer was a crucial step, aimed at achieving high-quality, uniform, and dense films. These additives played a key role in promoting the formation of larger crystals, improving charge transport and overall efficiency. In addition, they contributed to enhancing the surface morphology and uniformity while reducing defects and increasing stability. The preparation of the perovskite solution involved stirring it at 300 rpm and maintaining a temperature of 50°C for a duration of 15 minutes. Subsequently, the solution was meticulously filtered through a 0.45 μL syringe filter to ensure purity. For the deposition of the perovskite precursor onto the SnO₂ layer, a specific volume of 90 μL was spin-coated at a speed of 2000 rpm (for the exact spin-coated speed, please refer to chapter 4). During the initial 15 seconds of spinning, 150 μL of antisolvent was added dropwise onto the spinning perovskite film. This technique was instrumental in achieving the desired film quality. Adding antisolvent during the spin coating process increases the quality of the perovskite layer, resulting in greater solar cell performance.

Finally, the samples were carefully placed on the hotplate, covered with a petri dish, and annealed for 10 minutes at 90 °C. This annealing process was essential for the formation of dark MAPbI₃ films. Figure 3-5 (a) depicts the prepared MAPbI₃ solution and (b) the photograph of the FTO glass/SnO₂/MAPbI₃ structure.

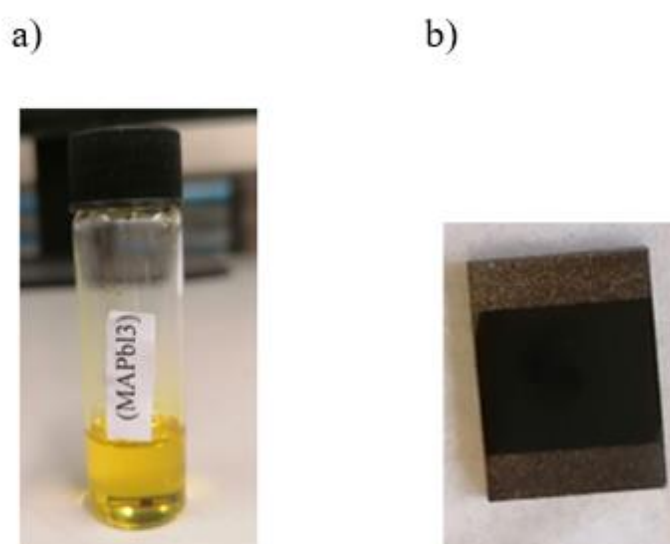


Figure 3-5 a) MAPbI₃ solution and b) FTO glass/SnO₂/MAPbI₃

3.3.4 Hole transport layer (Spiro-OMeTAD)

A specific quantity of 90 mg of Spiro-OMETAD powder from Borun Technology was dissolved in 1 mL of chlorobenzene (99.6%) from Across Organics. Additionally, the additives such as lithium bis(trifluoromethylsulfonyl)imide (Li-TFSI, 98%) from Alfa Aesar and tris(2-(1H-pyrazol-1-yl)-4-tert-butylpyridine)cobalt(III) tris(bis(trifluoromethylsulfonyl)imide) (FK209, 98%) from Sigma Aldrich were used. Specifically, 22 μL of Li-TFSI solution (520 mg/mL in acetonitrile) and the 38 μL of FK209 solution (300 mg/mL in acetonitrile) were added. Moreover, the Spiro-OMETAD solution was doped with 36 μL of 4-tert-butylpyridine (TBP, 96%) from Sigma Aldrich to enhance the film's electrical and energy band properties.

The HTL precursor was then stirred at 450 rpm and a temperature of 30°C for 30 minutes. Afterwards, 90 μL of the HTL solution was spin-coated onto the perovskite layers, with the spinning process lasting for 30 seconds at a speed of 4000 rpm. To ensure the solution's purity, it was filtered through a 0.45 μm syringe filter. Figure 3.7 (a) and (b) shows the Spiro-OMETAD solution and the fabricated FTO glass/SnO₂/MAPbI₃/Spiro-OMETAD structure, respectively.

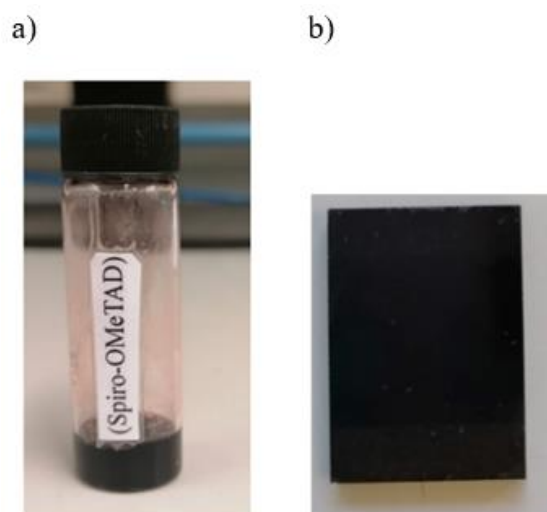


Figure 3-6 a) the Spiro-OMETAD solution and b) the fabricated FTO glass/SnO₂/MAPbI₃/Spiro-OMETAD structure.

3.3.5 Sputtering of silver deposition (Ag)

The process of depositing silver to create the top electrodes was carried out using Titan magnetron sputtering (a subsystem in PLD2000, PVD product) as shown in Figure 3-7(a). The source material for silver deposition was a disc target of 2-inch diameter and 0.125-inch-thick from the Kurt J. Lesker Company Ltd. To initiate the silver deposition, the sputtering chamber underwent an initial evacuation, followed by filling with argon gas. This carefully controlled environment was essential for the precise deposition of Ag electrodes onto the Spiro-OMETAD layer. A 2.2-inch substrate holder shown in Figure 3-7 (b) was used, holding up to four substrates simultaneously. Each substrate accommodates four devices with an active area of 0.15 cm², and the fifth active area served as the common point as illustrated in Figure 3-7 (c). The sputtering process was conducted under specific conditions a power setting of 1.0 W, a gas flow rate of 15.0 standard cubic centimetres per minute (sccm), a chamber pressure of 5.0 mTorr, and a substrate temperature maintained at 26°C for a duration of 1 hour[205]. To facilitate testing, the contact wires are soldered to the ends of the silver pads as shown in Figure 3-7 (d) using a low melting point Bi_{0.54}Sn_{0.26}Cd_{0.2} solder.

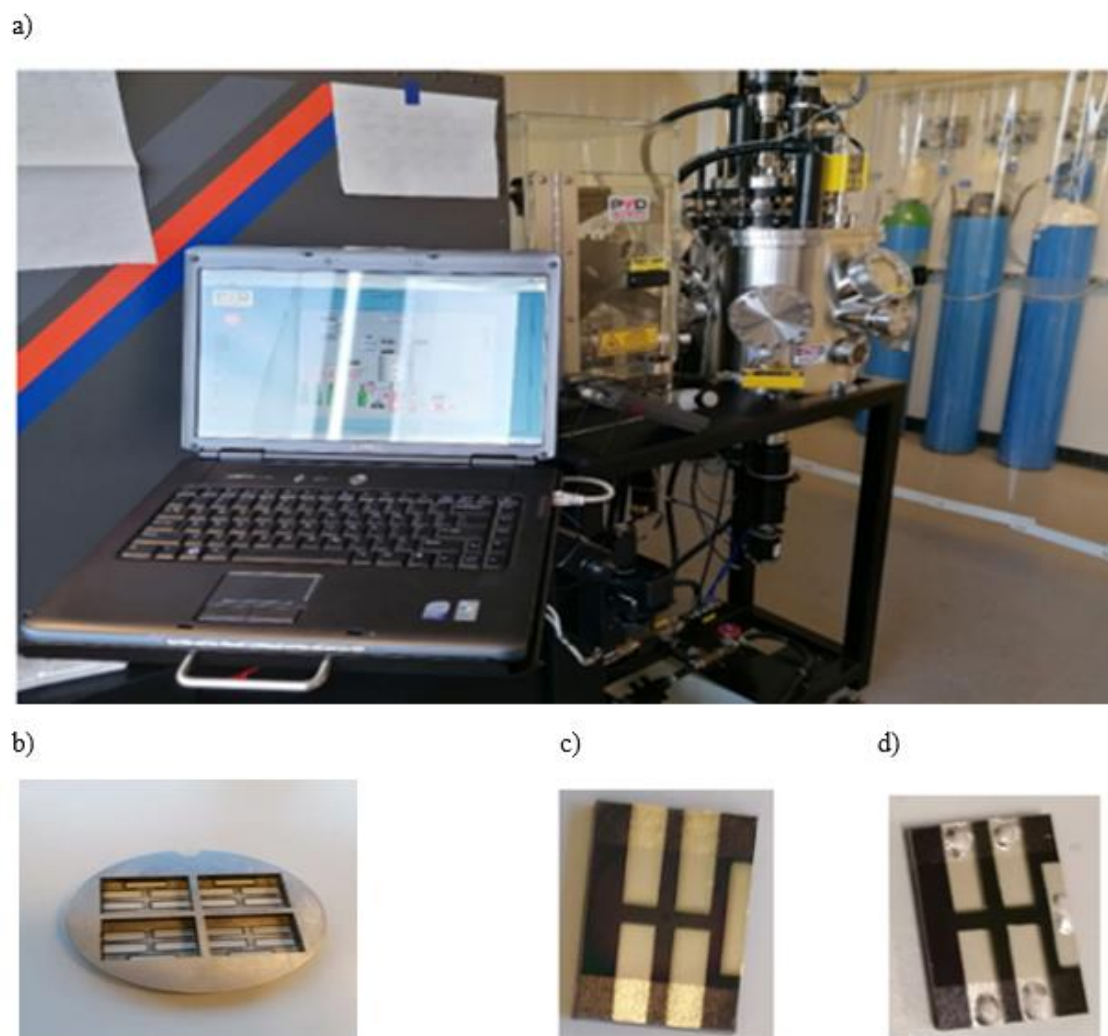


Figure 3-7 a) PLD2000 for magnetron sputtering, b) Substrate holder, c) Photograph of fabricated devices with four perovskite solar cells formed underneath the deposited silver layers, and d) Photograph of the perovskite solar cells with contact wires soldered on silver pads.

3.4 Characterisation of device layers

Five well-known analytical tools are frequently employed to examine the quality of the fabricated device layers in perovskite solar cells. Ultraviolet-visible spectroscopy (UV-Vis-NIR) for assessing absorption and optical properties, X-ray Diffraction (XRD) to examine crystalline structure and phase purity, Atomic Force Microscopy (AFM) for surface morphology and topography analysis, Fourier-Transform Infrared Spectroscopy (FTIR) to study chemical bonding and functional groups, and Scanning Electron Microscopy (SEM) for visualizing microstructure and cross-sectional morphology. These techniques collectively

provide essential insights into the physical, optical, and chemical properties of perovskite materials for assessing the film quality and optimizing device performance.

3.4.1 Ultraviolet-visible (UV-Vis) spectroscopy

Figure 3-8 shows Hitachi U-1900 UV-Visible spectrophotometer available at CLEER Lab at Cardiff University, which covers a wavelength range from 200 nm to 1100 nm. In this work, the Ultraviolet-Visible (UV-Vis) spectroscopy is used to determine the optical properties, including transmittance, absorbance and bandgaps of the materials used in perovskite solar cells, including FTO, SnO₂, and MAPbI₃ films.



Figure 3-8 Hitachi U-1900 Spectrophotometer

During the measurement, samples were carefully prepared and placed between a Xenon lamp light source and a detector. These samples were then exposed to light spanning the UV to NIR regions. The detector measured the light transmission of the sample at each wavelength, generating a transmittance spectrum. The absorbance (A) of the sample can be determined by

$$A = -\log\left(\frac{I}{I_0}\right) \dots\dots\dots \text{Equation3-1}$$

where, I and I_0 denote the intensity of light measured after passing through the sample and before entering the sample, respectively[206]. Transmittance, represented as $(\frac{I}{I_0})$, is illustrated in Figure 3-9, which shows how the transmittance of light decreases exponentially with increasing sample thickness, according to Beer-Lambert's law.

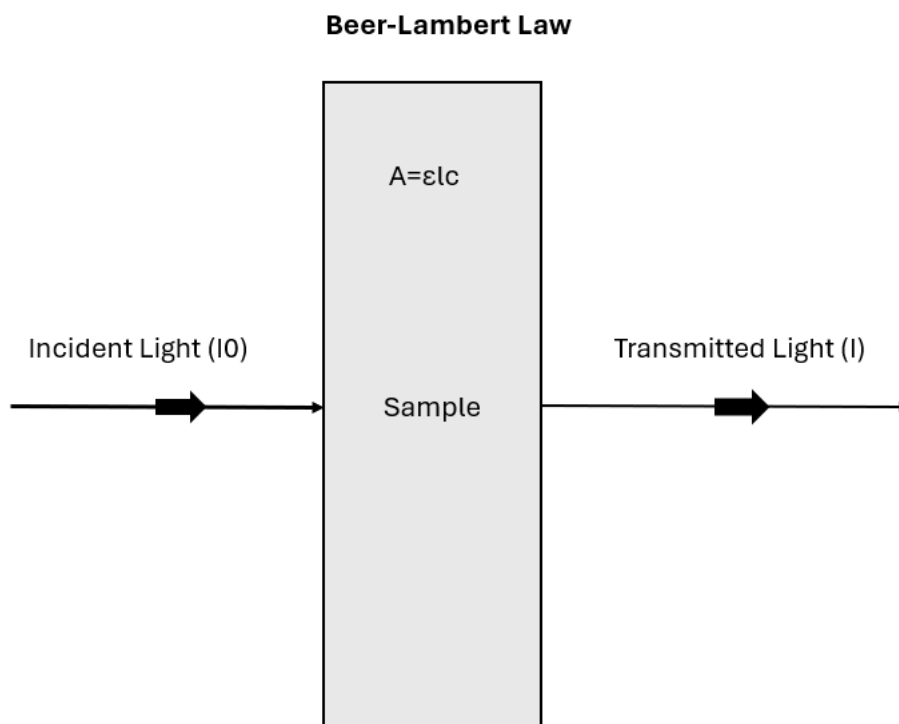


Figure 3-9 Schematic representation of Beer-Lambert law

Using the measured absorbance of MAPbI_3 layers, its energy band gap (E_g) can be estimated using Tauc plots based on Equation 3-2[207]. A Tauc plot is a technique for determining the energy bandgap of a material, which is the energy difference between the top of the valence band and the bottom of the conduction band[208]. The underlying principle of this method is the relationship between the absorption coefficient (α) and the photon energy ($h\nu$) of incident light, as described by the Tauc equation:

$$(\alpha h\nu)^n = A(h\nu - E_g) \text{ Equation 3-2}$$

where, α is the absorption coefficient, indicating how much light is absorbed per unit distance in the material. $h\nu$ is the photon energy (where h is Planck's constant and ν is the frequency of the light). n is a constant related to the type of electronic transition ($\frac{1}{2}$ for direct allowed, and 2 for indirect allowed).

Tauc plot is constructed by plotting $(\alpha h\nu)^n$ against $h\nu$. Figure 3-10 shows an example of MAPbI₃ film with $n=2$. Then the energy bandgap E_g can be determined from the intercept of the linear portion of the plot on the energy axis. The knowledge of the energy band gap of perovskite films is particularly beneficial because it provides information on the range of light wavelengths that the fabricated perovskite layers can absorb.

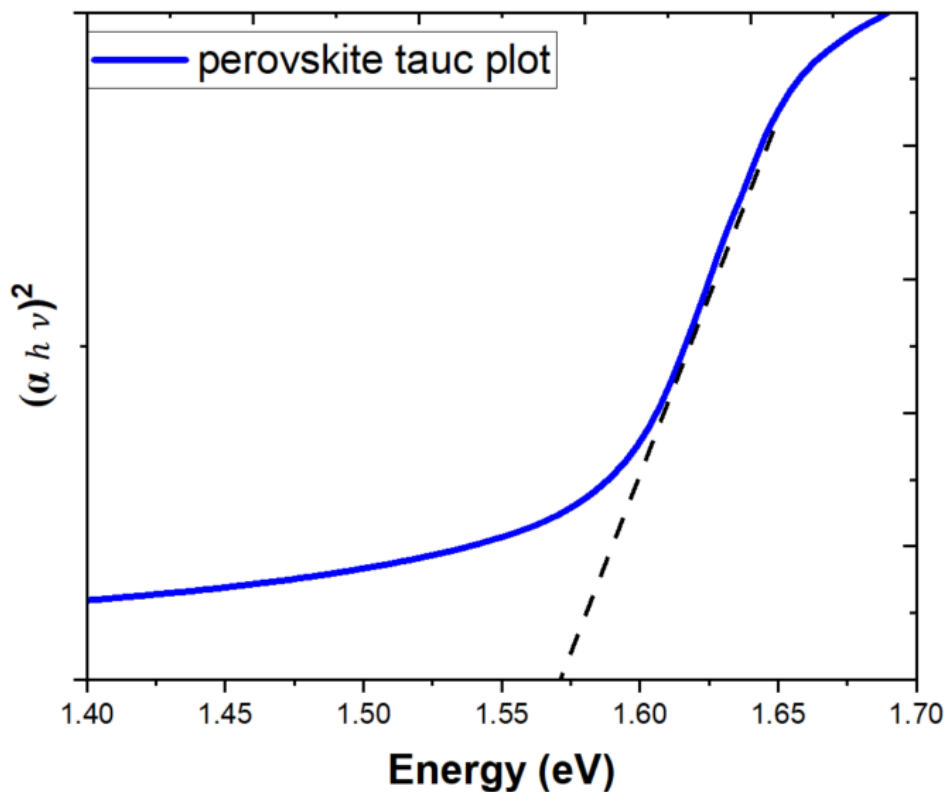


Figure 3-10 Tauc plot of the fabricated MAPbI₃ film showing an energy band gap of 1.55 eV.

3.4.2 X-ray diffraction (XRD)

For X-ray diffraction analysis, a Siemens D5000 X-ray diffractometer was used, which operated at a voltage of 40 kV and a current of 35 mA. Copper (Cu) was used as the target material, generating $\text{CuK}\alpha$ radiation with a wavelength of 1.5418 Å. The primary objective of this analysis was to elucidate the structural characteristics of the FTO, SnO_2 , and MAPbI_3 films through an examination of peak intensity, peak position, and preferred orientation.

For the MAPbI_3 and SnO_2 layers deposited on FTO substrates, we measured diffraction pattern within the range of $10^\circ \leq 2\theta \leq 50^\circ$, as this range encompassed the relevant peaks critical for the samples analysis. Furthermore, we acquired data within the same range ($10^\circ \leq 2\theta \leq 50^\circ$) for both the FTO and FTO/ SnO_2 structures independently. This served as a validation step, allowing us to cross-reference observations from the individual spectra.

The XRD spectra obtained was analysed using X Pert High Score Plus software, and the XRD data were converted into Excel formats using a POWDLL converter. Figure 3-11 shows the Siemens D5000 X-ray diffractometer system used for this work.



Figure 3-11 Siemens D5000 X-ray diffractometer system.

3.4.3 Atomic force microscopy (AFM)

The AFM was used to examine the surface characteristics of the device layers. Essentially, it uses nanoscale probe affixed on to a cantilever moving along a sample surface and ensuing interaction between the surface and the cantilever, which leads to deflection. This deflection induces alterations in the reflected laser beam detected by a quadrant photodiode, which provides valuable information on the variations in surface height, enabling examination of surface morphology and roughness. The AFM can operate in a tapping mode. It is a particularly advantageous approach when dealing with soft or highly uneven samples. Tapping mode entails the probe oscillating and intermittently contacting the sample surface. This method minimizes the risk of the probe dragging along the surface, ensuring accuracy and preserving sample integrity. TESPA-V2 probes by BRUKER.CO were employed in this work. Initially, the FTO surfaces were inspected before the SnO_2 , and MAPbI_3 films were deposited. Then, AFM scans were performed after each layer was deposited to examine the surface morphologies the respective layers.

The AFM images obtained by scans can be further analysed using nasoscope analysis software. This software facilitates the extraction of various surface parameters,

including root-mean-square (RMS) roughness and pit heights. Figure 3-12 shows the Dimension 3100 AFM instrument used for this study.

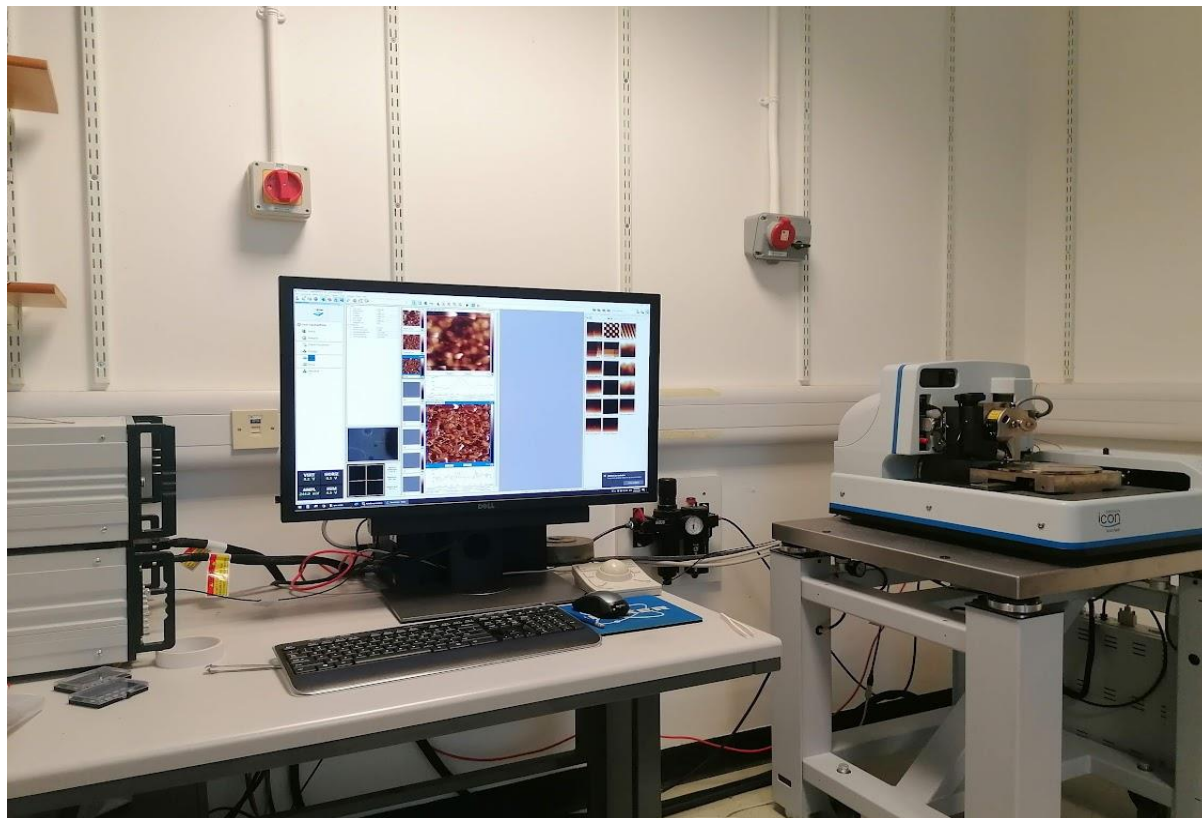


Figure 3-12 Dimension 3100 AFM instrument.

3.4.4 Fourier-transform infrared spectroscopy (FTIR)

Fourier-transform infrared spectroscopy (FTIR) can provide information on the chemical constituent and molecular structure of organic and polymeric materials from the signature peaks of infrared absorption of measurement. In this project, the Shimadzu FTIR-8400S spectrophotometer was used to check the composition of the MAPbI₃ layers. Operated in attenuated total reflection (ATR) mode, the Shimadzu FTIR-8400S spectrophotometer covered a spectral range from 400 to 4000 cm⁻¹. Glass substrates with deposited Ag films were carefully chosen since silver is known for its high reflectivity and is frequently used as

the top electrode in solar cell devices. Figure 3-13 depicts the Shimadzu FTIR-8400S spectrophotometer used for this study.

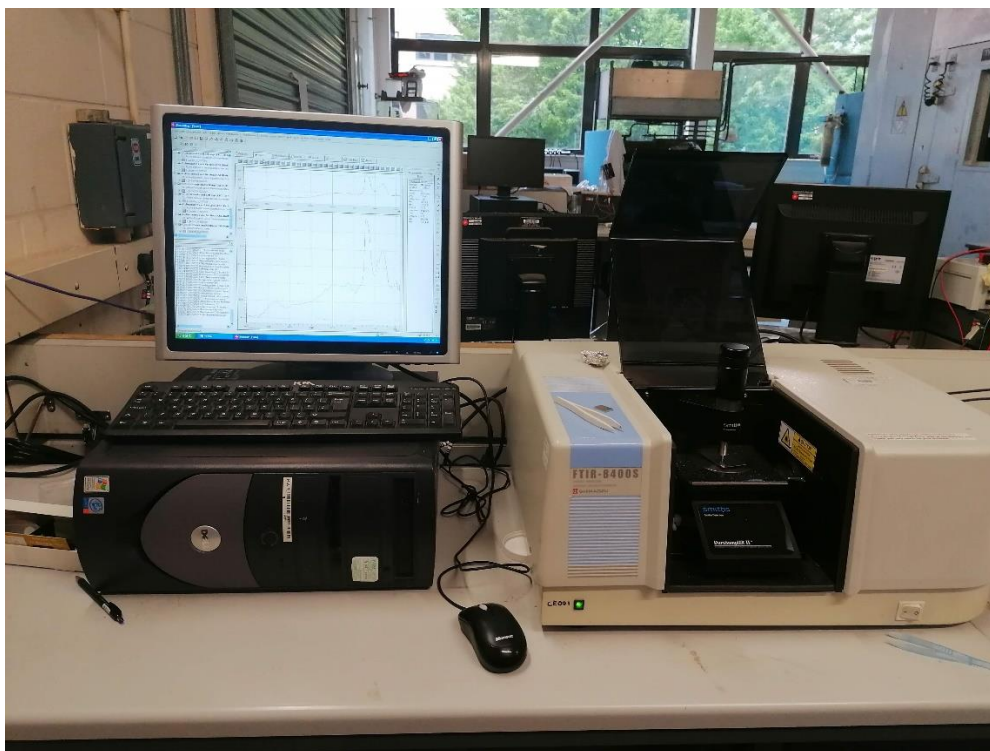


Figure 3-13 Shimadzu FTIR-8400S spectrophotometer

3.4.5 Scanning electron microscopy (SEM)

Scanning electron microscopy (SEM) is used to examine the surface morphology and topography of perovskite materials and their interfaces in the solar cell structure. SEM offers high-resolution imaging capabilities, facilitating the visualization of various aspects such as microstructure, grain boundaries, and defects present in the perovskite layers. SEM can also be used to evaluate the uniformity of the perovskite films, which is important for achieving optimal device performance. Additionally, SEM imaging aids in characterizing interfaces between different layers. The SEM used for this study is Zeiss 1540 XB Crossbeam Field Emission Scanning Electron Microscope (FE-SEM) as shown in Figure 3-14 . It enables to capture top-view micrograph of MAPbI_3 films, detection of grain sizes, morphology, and pinholes. Furthermore, cross-sectional SEM images were utilized to determine the thicknesses of various layers within the perovskite device, including FTO, SnO_2 , MAPbI_3 , Spiro-OMETAD, and Ag layers. To ensure optimal imaging for perovskite materials, the Working

Distance (WD) at 7.1 nm and the Electron High Tension (EHT) at 5.0 kV were selected for top-view SEM measurements.



Figure 3-14 Zeiss 1540 XB Crossbeam Field emission scanning electron microscope (FE-SEM)

3.5 Evaluate the performance of the perovskite solar cells

Evaluating the performance of perovskite solar cells is essential in gaining insights into their efficiency and stability. This section describes the methods employed to evaluate the performance of perovskite solar cells.

3.5.1 Current -Voltage measurements

In this study, the AUTOLAB system (Metrohm, PGSTAT302N) was used to undertake extensive characterizations of perovskite solar cells (PSCs). For illumination, the Newport Oriel LCS-100 solar simulator was used, which employed a xenon lamp as a light source meeting Class ABB standards.

To ensure accurate and consistent results, the vertical distance between the solar simulator and the test samples was carefully calibrated.. This adjustment was facilitated

through the use of the calibrated Reference Si-cell from Sola Survey 200R, SEAWARD, allowing us to achieve the desired total solar intensity, as illustrated in Figure 3-15 Combining the AUTOLAB system with the Newport Oriel LCS-100 solar simulator and the precision adjustments enabled by the Reference Si-cell, enables to obtaining of robust and reliable data for the evaluation of perovskite solar cell performance.

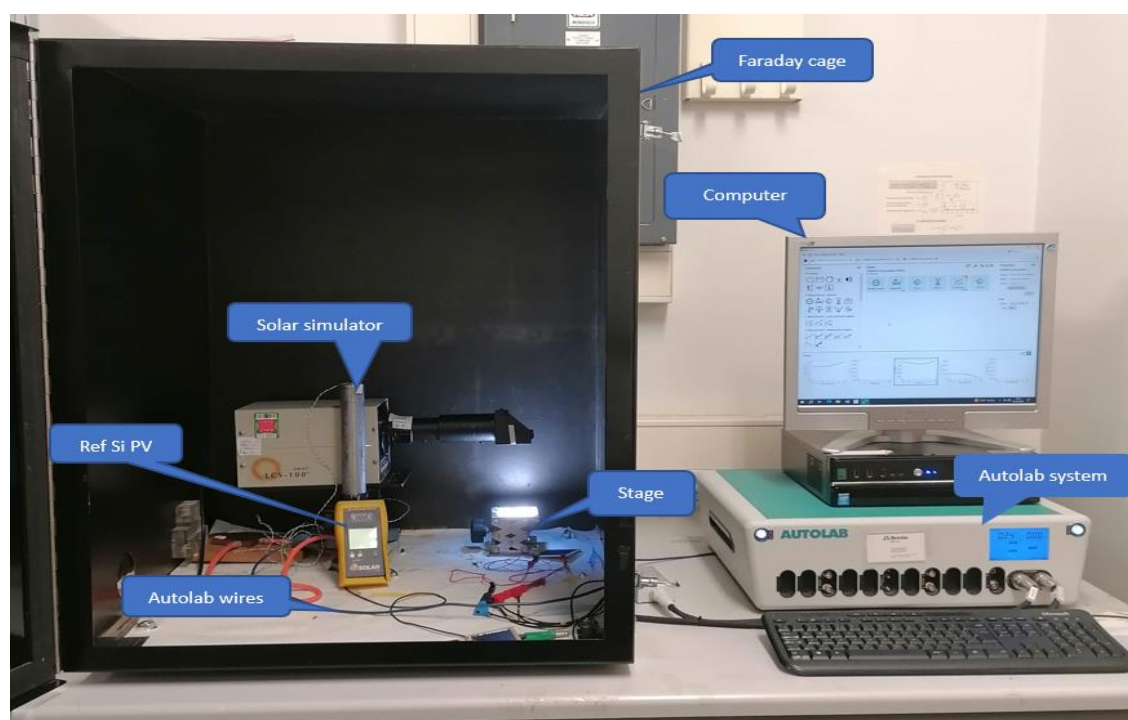


Figure 3-15 Newport Oriel LCS-100 solar simulator/PGSTAT302N Autolab Metrohm setup for I-V measurement system

The current-voltage (IV) curve is an important measure for evaluating solar cell performance. It serves as a graphical representation of the relationship between the current flowing through the solar cell and the applied voltage across it. This curve provides valuable insights into the electrical characteristics and efficiency of the solar cell.

By varying the voltage bias applied to the cell and measuring the corresponding current, various operating points can be determined, including the (V_{oc}) and (J_{sc}). These fundamental parameters, along with the (FF) and (PCE), which summarise the overall cell

performance, play a critical role in determining the power output and efficacy of solar cells. To confirm the accuracy and repeatability of the equipment, a silicon solar cell was tested. As illustrated in Figure 3-16

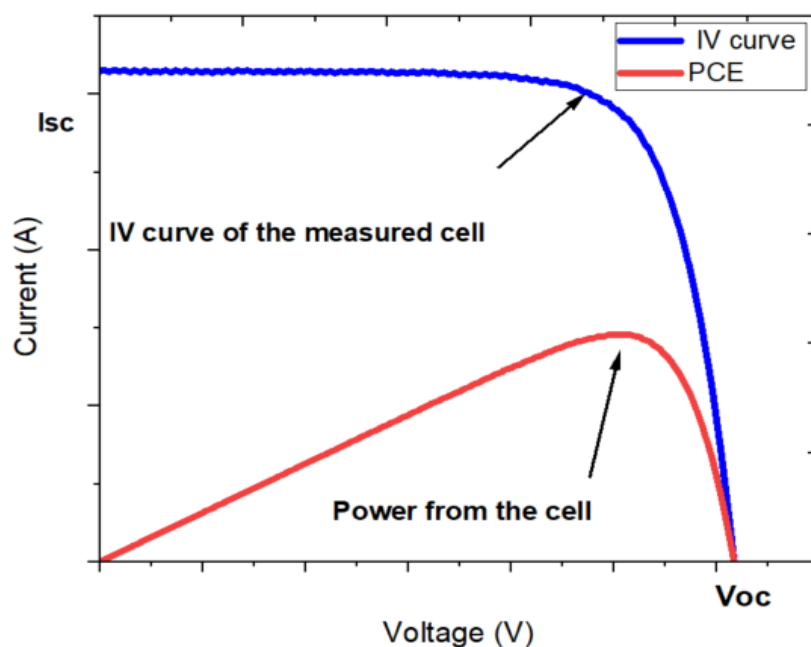


Figure 3-16 the current -voltage (I-V) curve of tested silicon solar cell

NOVA software together with Autolab system (Metrohm, PGSTAT302N allowed to plot the I-V curve of perovskite solar cells (PSCs). Standard solar irradiance conditions of 100 mW/cm² (equivalent to 1000 W/m²), applying a voltage of 1.12V were ensured so that I-V measurements were acquired under standard irradiance. The precision of our measurements was maintained through the use of the calibrated Reference Si-cell from Solar Survey 200R, SEAWARD, as depicted in the preceding section.

3.5.2 Impedance spectroscopy

Impedance spectroscopy (IS) offers additional characterisation for the perovskite solar cells that is complementary to I-V measurements, which enables determination of solar cell capacitance. In addition, the series resistance (R_s) and shunt resistance (R_p) can also be extracted from IS measurement. In this study, sinusoidal signals with an amplitude of 75 mV and a frequency range of 10 Hz to 1.0 MHz were used as the input signal with a DC bias of 0.2

V was simultaneously applied. Measurements were performed under light irradiation at 100 mW/cm² to provide insights on charge extraction, while the measurements in the dark were carried out to investigate recombination resistance (R_p) and transport resistance (R_s).

A particular analysis of the data collected under illumination at 100 mW/cm² allowed us to derive the chemical capacitance, an indirect indicator of charge carrier density, using the Z SimpWin Software 3.2. Figure 3-17 shows an example schematics of impedance spectra for a PSC device.

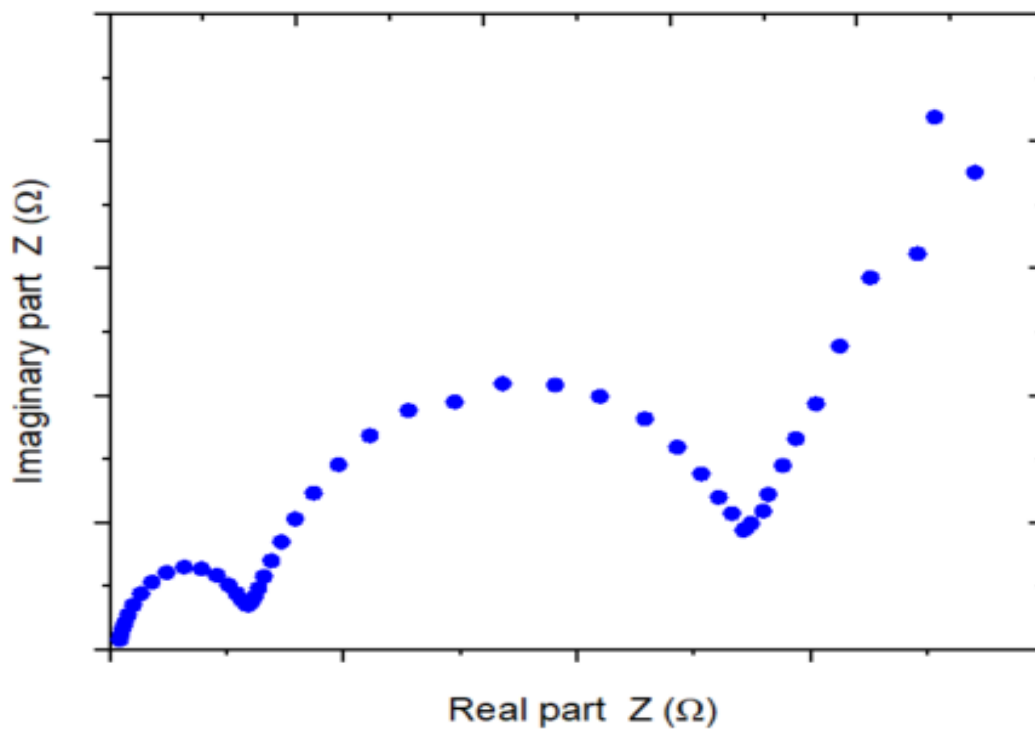


Figure 3-17 an example schematic of impedance spectra for PSC device

3.5.3 Sheet resistance

The 4-probe method for measurement of sheet resistance is used to evaluate the electrical properties of the fabricated thin films, particularly the electrodes in solar cells. Figure 3-18 shows an in-house built 4-probe measurement system. The sheet resistance is defined as the electrical resistance between two opposite edges of a square or rectangular film and is used as a measure for evaluating the electrical conductance of thin films without requiring the knowledge of the film thickness. In this study, the 4-probe technique was employed to check and ensure sufficient electrical conductance of the Ag top-electrode.

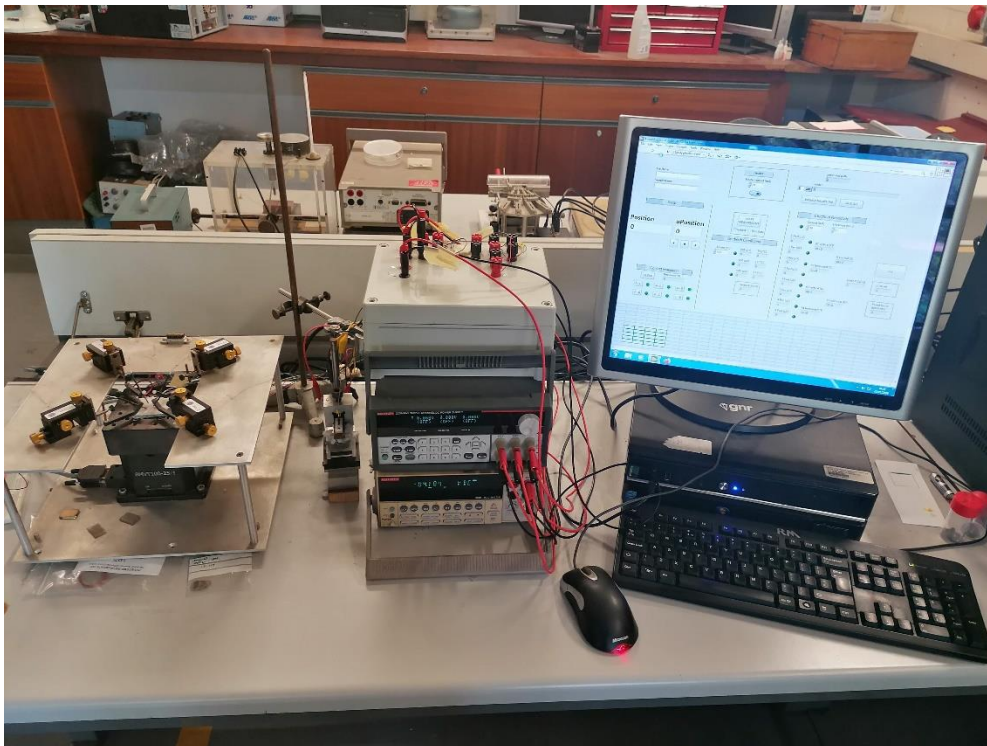


Figure 3-18 In-house built apparatus for 4-probe measurement.

3.6 Summary

This chapter describes the procedures and techniques employed in this study for preparation and characterization of perovskite solar cells. The structure of the perovskite solar cell was adopted from a previous study. Its components and their roles in the devices were discussed. Fabrication processes of perovskite solar cells used in this study were explained, with detailed account on specific procedures for preparation of solutions, additives and PSC layers including SnO₂, perovskite active layer, Spiro-OMeTAD, and silver top-electrode. The techniques and facilities used for characterising PSC layers and device performance were summarised, which include ultraviolet-visible spectroscopy (UV-Vis) for optical properties and energy band gap, X-ray diffraction (XRD) for crystallographic structures and chemical compositions, atomic force microscopy (AFM) for surface morphology and roughness, Fourier-transform infrared spectroscopy (FTIR) for molecular signature of organic materials, scanning electron microscopy (SEM) for morphology and microstructure, and 4-probe apparatus for electric conductance. The power output and photovoltaic parameters were evaluated using the I-V and IS measurements under light irradiation from a solar simulator.

Chapter 4: Establish in air fabrication procedures.

4.1 Introduction

This chapter aims at establishing procedures to fabricate perovskite solar cells in ambient air, starting with exploration of initial fabrication procedures based on the knowledge from the literature [174]. It is anticipated that these efforts will shed light on the key issues and challenges that must be addressed to ensure the production of good quality perovskite solar cells. Although the efforts involve fabrication of complete solar cells, the main focus will be on the perovskite photoactive layer and identifying appropriate processing parameters including annealing temperature, spin-coating speed, and antisolvent. The findings obtained in this study is a crucial step to enable further in-depth research in this endeavour.

4.2 Establish initial fabrication procedure

Initial trials of fabricating perovskite solar cells were carried out to gain the practical knowledge and skills for device fabrication. All perovskite solar cells were fabricated based on a device structure described in section 3.2. Each component layer of the devices was prepared following the procedures explained in section 3.3. The section below provides the specific values of the fabrication parameters used in these initial trials.

4.2.1 Film and device fabrication

For preparation of the SnO₂ electron transport layer, the FTO substrate was cleaned using exactly the same procedures as detailed in section 3.3.1. Then, a specific volume of 90 μ l of SnCl₂H₂O at a concentration of 15 mg/ml was used for spin-coating, followed by annealing at 180 °C for 1 hour, and a further 10-minute treatment in the ozone cleaner.

For the photoactive MAPbI₃ layer, the perovskite precursors were prepared as detailed in section 3.3.3. A volume of 90 μl of the solution was used for spin-coating at 2000 rpm for 30 seconds. During this period, a volume of 0.15 mL of chlorobenzene antisolvent was added onto the film after the initial 15 seconds. Immediately following deposition, the films were annealed at 120 °C for 15 minutes.

To prepare the hole transport layer, a volume of 90 μl spiro-MeOTAD solution was spin-coated on to the MAPbI₃ layer at spin-coating at 4000 rpm for 30 seconds. It is to be noted that all three layers mentioned above were prepared in ambient air (i.e., without controlled environment). The relative humidity during prepared was monitored which was between 35% and 45%.

The Ag layers were deposited using magnetron sputtering using a mask to create active cell area of 0.15 cm². The deposition was carried out at an argon flow rate of 15.0 sccm, a pressure of 5.0 mTorr, and a sputtering duration of 1 hour. The contact leads for device testing was soldered on to Ag pads using a Bismuth Tin Cadmium Alloy.

4.2.2 Performance of the devices

The I-V curves of the perovskite solar cells fabricated from initial trials were measured under 1 sun irradiation using the facilities described in section 3.5. The results of the best performed devices from each substrate (each substrate consists of 4 cells) are in Figure 4-1. The I-V curves enable extraction of photovoltaic parameters, such as V_{oc} , J_{sc} , R_s , R_{sh} and P_{max} , and then PCE and FF can be calculated. Table 4-1 listed the photovoltaic parameters for the 16 devices, along with the average calculated for all devices on each substrate.. Clearly, the values of the output power density (P_{max}) from these devices are significant smaller than the typical value of the perovskite solar cells, indicating the issues with fabrication which needs to be improved. It can be seen that the device designated as Sub 1 has a V_{oc} of 0.62 V and J_{sc} of 18.0 mA/cm², both are smaller than the typical values of around 1.0 V and 25 mA/cm² for the state-of-the-art perovskite solar cells. Furthermore, the series resistance R_s for Sub 1 was 122 Ω , which is more than twice of the reported value (\sim 50 Ω) for the devices with the same area and contributes to a poor FF of 40%. The device Sub 2 has a higher V_{oc} of 0.84 V, but lower J_{sc} of 12.5 mA/cm², with similar R_s and FF, showing big variations in the photovoltaic properties of the devices fabricated under the same conditions.

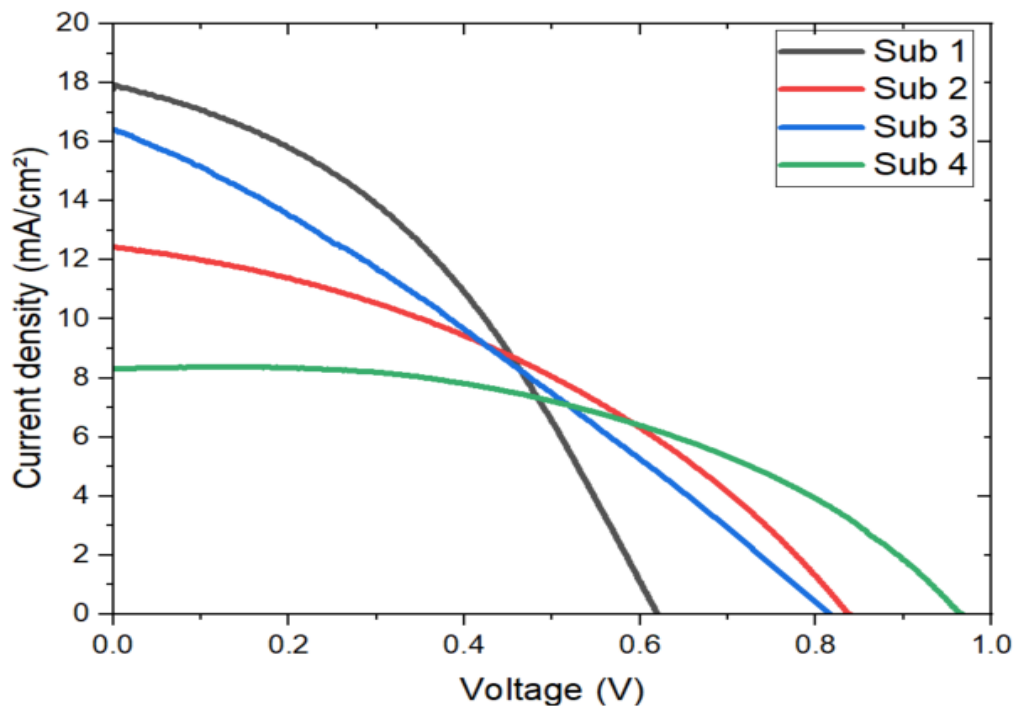


Figure 4-1 J-V characteristics of the initial experiment

Sub 3 exhibits a similar V_{oc} to Sub 2 but slightly higher J_{sc} of $16.4 \text{ mA}/\text{cm}^2$. However, it has a larger series resistance (R_s) of 268Ω and a smaller shunt resistance (R_{sh}) of 654Ω , contributing to a very small FF of 29%. A high series resistance suggests poor conductivity within the cell and a low shunt resistance indicates the presence of leakage paths due to recombination. Sub 4 has a large V_{oc} of 0.97 V , which is close to the reported value. However, the J_{sc} is relatively low at $8.4 \text{ mA}/\text{cm}^2$, resulting in a small output power. The results from this initial experiment show that reasonably high short-circuit current density can be obtained in some cases (e.g., Sub 1) while reasonably larger open-circuit voltage can be obtained in other cases (e.g., Sub 4). However, all of them have relatively small FF with big variations in photovoltaic parameters, indicating a problem of unreliable fabrication that needs to be resolved. Clearly, systematic investigations are necessary to identify optimal fabrication parameters for developing reliable fabrication.

Table 4-1 Photovoltaic parameters of the perovskite devices for the initial experiment

Substrates	V_{oc} (V)	J_{sc} (mA/cm ²)	P_{max} (mW/cm ²)	FF	R_s (Ω)	R_{sh} (K Ω)
Sub 1	0.62	17.95	4.42	40	122	0.75
Ave	0.77±0.15	12.53±4.01	3.91±0.70	43±8	133±80	0.55±0.17
Sub 2	0.84	12.46	4.03	39	29	0.23
Ave	0.83±0.07	10.01±4.13	3.38±0.44	45±13	16±10	0.42±0.32
Sub 3	0.82	16.42	3.87	29	268	0.65
Ave	0.74±0.13	13.40±2.33	3.04±0.86	30±1.42	260±10	0.73±0.18
Sub 4	0.97	8.39	3.86	48	238	1.4
Ave	0.90±0.04	6.25±1.93	2.91±0.65	53±9.5	181±109	6.4±5.5

Sub-1, Sub-2, Sub-3, and Sub-4 represent devices fabricated on different substrates, with each substrate undergoing similar initial fabrication conditions. The differences in their J-V characteristics arise from variations in their photovoltaic parameters. Sub-1, for example, has a relatively low V_{oc} (0.62 V) and high J_{sc} (17.95 mA/cm²), but poor fill factor (40%) due to a high series resistance R_s (Ω) of 122 Ω . In contrast, Sub-4 exhibits the highest V_{oc} of (0.97 V) but significantly lower J_{sc} (8.39 mA/cm²) and a small P_{max} of 3.86 mW/cm². Sub-2 and Sub-3 display intermediate behaviours, with Sub-3 suffering from the highest R_s (Ω) (268 Ω), contributing to its poor fill factor (29%). These differences underline issues with fabrication reproducibility, necessitating further optimization of parameters such as material quality, deposition techniques, and processing conditions to achieve consistent device performance.

4.3 Optimisation fabrication procedure

Based on the outcomes of the above initial trials, it is clear that systematic investigations are needed to identify suitable fabrication parameters in order to improve the fabrication quality. Considering the MAPbI₃ layer is the most sensitive layer to ambient air, the following investigations focused on optimization of the fabrication parameters of the

MAPbI₃ layer, including annealing temperature, spin-coating speed and antisolvent treatment.

4.3.1 Optimising annealing temperature of MAPbI₃ layer

One of the key factors influencing the quality of the MAPbI₃ layer is the annealing temperature. A set of experiments with different annealing temperatures was planned and carried out to investigate its impact on the efficiency and overall stability of the perovskite layers and devices. MAPbI₃ layers and devices were prepared at different annealing temperature. The fabricated devices were characterized in terms of V_{OC} , J_{SC} , P_{max} , FF, R_s , and R_{sh} . The average values and standard deviations were calculated from multiple measurements.

4.3.1.1 Film and device fabrication

In the fabrication process, SnO₂ layers were deposited onto FTO substrates using a solution containing 15 mg/ml of SnCl₂.2H₂O. Subsequently, the MAPbI₃ films were prepared onto the SnO₂ layers by spin-coating, followed by annealing, as described in section 3.3.3, at temperatures of 60 °C, 90 °C, 120 °C, and 150 °C, respectively. Afterward, the hole transport layers were spin-coated on the top of the MAPbI₃ layers using a 90 μl of Spiro-OMETAD solution, consisting of 90 mg of Spiro-OMETAD, 36 μl of MPPD, 38 μl of FK209, and 22 μl of Li-TFSI, and all dissolved in 1 ml of chlorobenzene.

All the solution-processed procedures were executed in ambient air with the relative humidity within a range of 22% to 55%. The Ag top electrodes were deposited using the same deposition parameters as described in section 3.3.5.

4.3.1.2 Result and discussion

I-V curves of the fabricated devices were measured and the corresponding photovoltaic parameters were extracted as described in section 3.5.2. The results are displayed in Table 4-2, showing variations of V_{oc} , J_{sc} , P_{max} , FF, R_s , and R_{sh} with different annealing temperatures of the MAPbI₃ layers. It can be seen that the annealing temperature of the MAPbI₃ layer has a clear influence on all photovoltaic parameters of the fabricated devices. Although the outcomes appear to be complex due to the fact that other processing conditions can affect the performance of the devices, the results of this experiment indicate an optimal annealing temperature at around 90°C, where the device has the highest J_{sc} of 19.37 mA/cm², highest FF of 45%, smallest R_s of 150 Ω, and reasonable V_{oc} of 0.83 and R_{sh} of 2 k Ω, leading among to the highest P_{max} of 7.27 mW/cm² (corresponding to a PCE of 7.27%) among all devices fabricated in this experiment.

Table 4-2 Photovoltaic parameters of the fabricated perovskite devices for different MAPbI₃ annealing temperatures ("Best" denotes the data obtained from the best-performing devices and "Ave" denotes the average performance of 16 PSCs and the area of each device is 0.15 cm²)

Anneal temp.	V_{oc} (V)	J_{sc} (mA/cm ²)	P_{max} (mW/cm ²)	FF	R_s (Ω)	R_{sh} (KΩ)
60 °C (Best)	0.76	15.93	4.94	41	154	2
(Ave)	0.70±0.19	15.25±1.10	3.53±1.31	33±5.53	207±73	0.81±0.51
90 °C (Best)	0.83	19.37	7.27	45	150	2
(Ave)	0.78±0.07	19.49±0.76	5.72±1.12	43±3.73	130±	0.92±0.20
120 °C (Best)	0.98	17.60	6.81	39	201	1.7
(Ave)	0.82±0.09	16.04±2.18	5.52±1.07	42±6.03	41±44	0.55±0.45
150 °C (Best)	0.92	15.24	6.40	46	194	2.5
(Ave)	0.78±0.12	15.22±3.19	4.62±1.61	38±5.1	190±46	1.46±0.86

Table 4-2 shows the measured J-V curves of the best performing devices fabricated in this experiments for different annealing temperatures of MAPbI₃ layers. The plots on this figure indicate that the J_{sc} is optimised at around 90°C while the V_{oc} is around 120°C. In order to identify if the annealing temperature at 90°C is better choice, further analysis is needed.

Figure 4-3 a) shows the absorbance of the MAPbI₃ films, which were deposited on the FTO/SnO₂ substrates and annealed at temperature of 60°C, 90°C, 120°C, and 150°C, respectively. It can be seen that the annealing at 90°C and 120°C produced the films with better light absorption than those annealed at 60°C and 150°C, confirming that appropriate annealing temperature is within a range from 90°C to 120°C. Furthermore, Tauc plots of the annealed MAPbI₃ films can be constructed as shown in Figure 4-3b), from which the energy band gap of the fabricated MAPbI₃ films can be determined. The energy bandgap (E_g) for all annealed films falls within the range of 1.58-1.59 eV, which is in agreement with the values reported in [187].

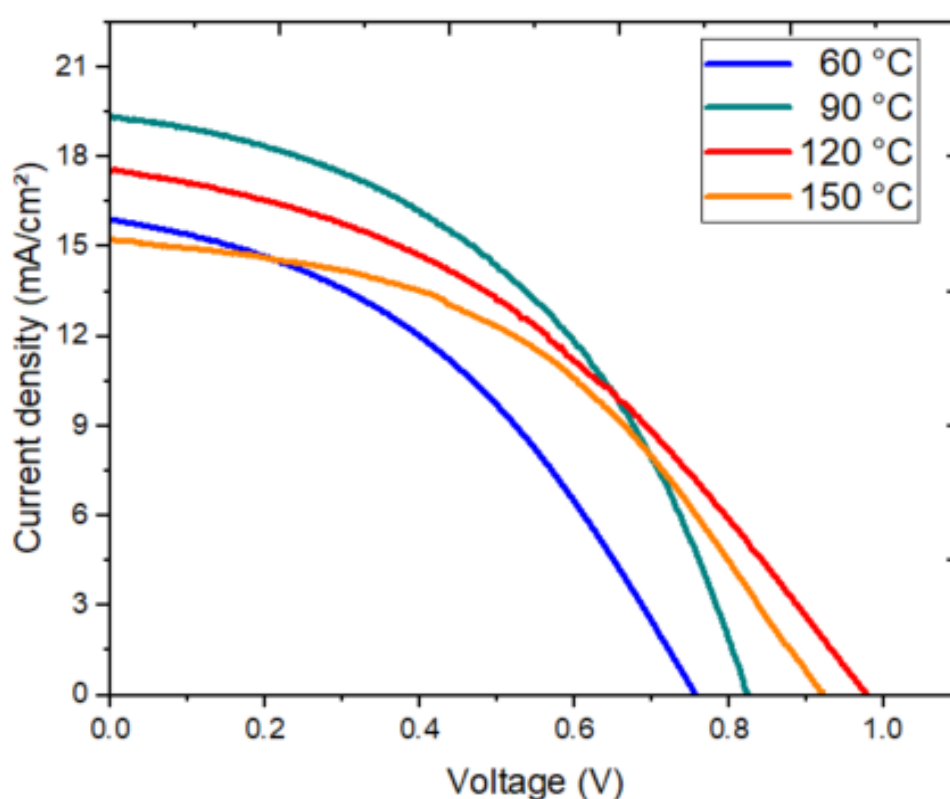


Figure 4-2 J-V characteristics of the best performing devices for different annealing temperatures of MAPbI₃ layers.

The differences in the J-V curves stem from how annealing temperatures affect the MAPbI₃ film's quality. At 90°C, optimal crystal growth and minimal defects lead to the highest J_{sc} , FF, and overall performance. At 60°C, incomplete crystallization causes higher defects and R_s , lowering J_{sc} . At 120°C, non-uniform crystals and pinholes reduce FF despite decent J_{sc} , while at 150°C, smaller crystals and rougher surfaces increase recombination and resistance, further degrading performance.

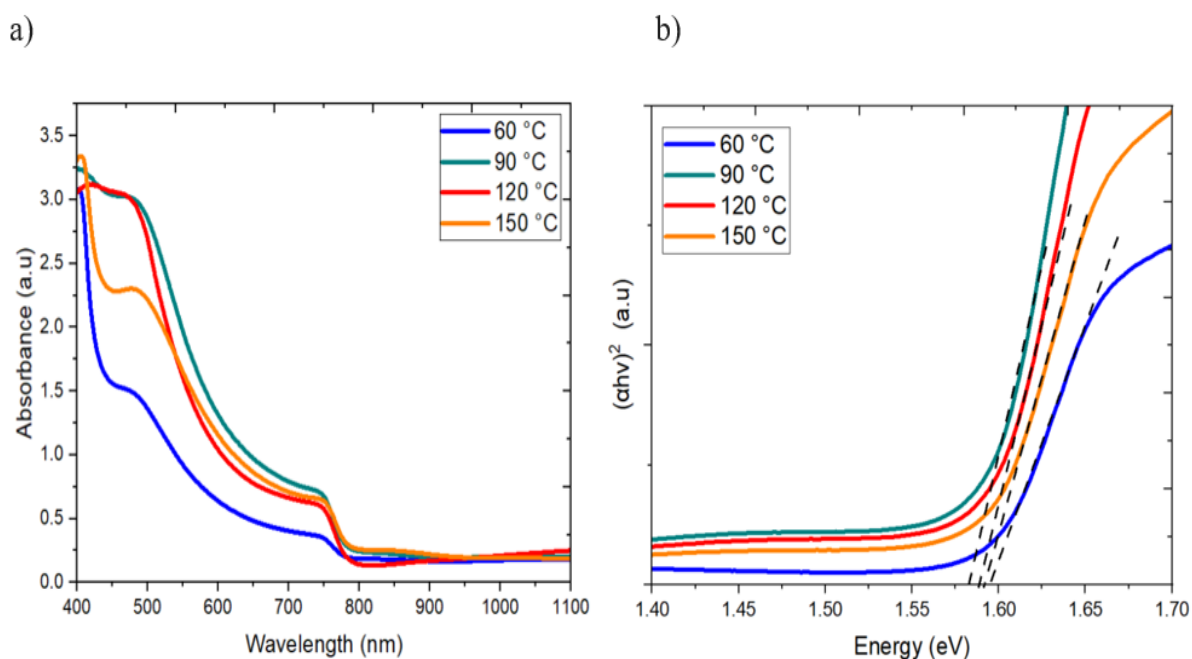


Figure 4-3 a) Absorbance spectra of MAPbI₃ layers fabricated at different annealing temperatures b) Tauc plot of MAPbI₃ layers at different annealing temperatures

Figure 4-4 a) presents the XRD spectra of the MAPbI₃ films deposited on FTO/SnO₂ substrates at different annealing temperatures (60°C, 90°C, 120°C, and 150°C). The diffraction peaks observed at 14.38(110), 20.32(211), 28.18(220), and 32.18(310) correspond to specific crystal planes of the perovskite films of the tetragonal phase as reported in [188]–[190]. While the peaks at 24.80(110), 35.53(101), and 38.06 (200) correspond to the FTO/SnO₂ films. It can be seen that the typical perovskite peaks are presented in all the films regardless annealing temperatures, indicating the formation of perovskite crystals. However, the peaks of the films annealed at 90°C appear to be more pristine, suggesting the better quality of crystals. Furthermore, the films annealed at 90°C exhibit a relatively small FWHM (Full Width at Half Maximum) as shown in Figure 4-4 b). This implies that relatively large crystals were formed after annealing at 90°C, compared to other annealing temperatures. In solar cell applications, large perovskite crystals

are preferred due to their high carrier mobility. The results from this analysis indicates that 90°C is a favourable annealing temperature to obtain good quality perovskite films.

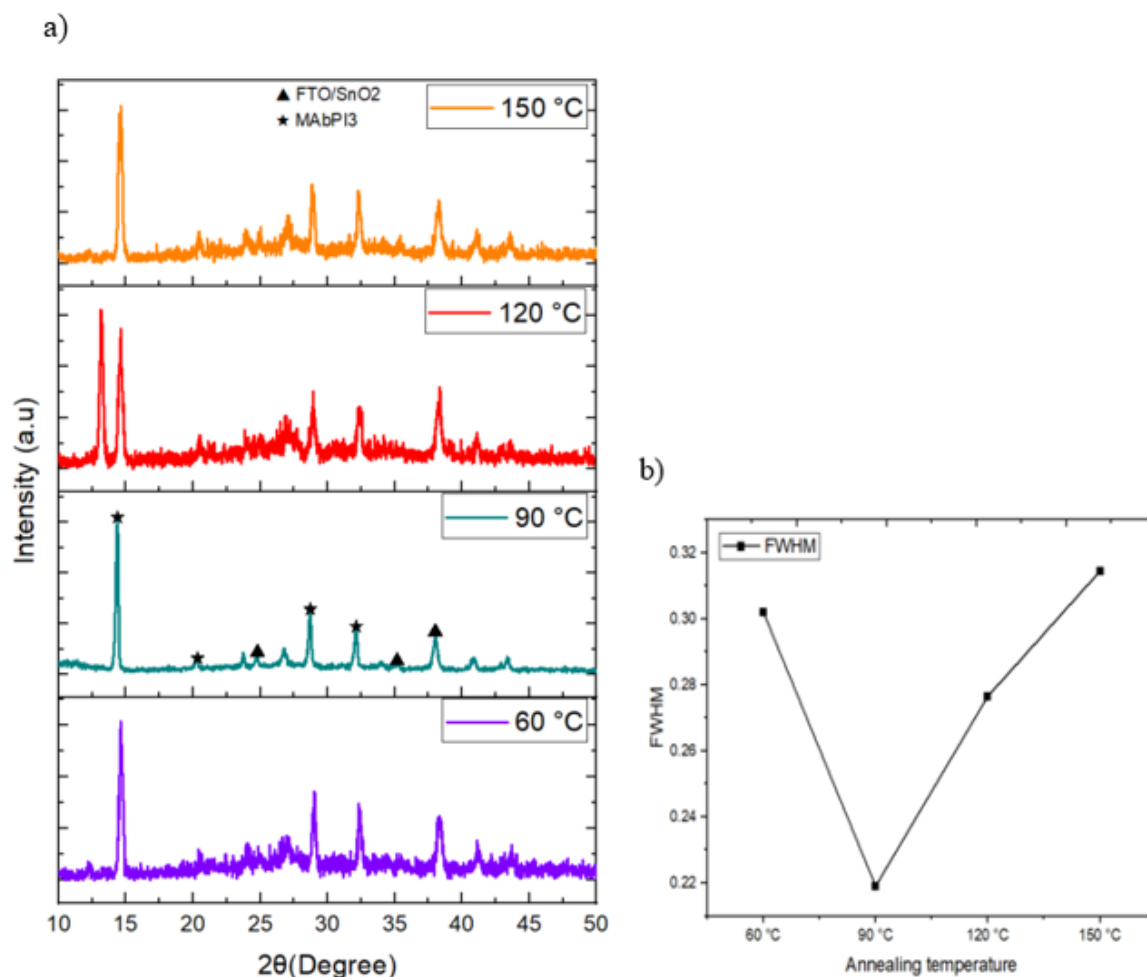


Figure 4-4 a) XRD spectra of FTO/SnO₂/MAPbI₃ at different annealing temperatures b) The Full Width at Half Maximum (FWHM) of the MAPbI₃ peaks of different annealing temperatures.

Atomic Force Microscopy (AFM) was employed to examine the morphology and surface roughness of the MAPbI₃ films annealed at temperatures (60°C, 90°C, 120°C, and 150°C). AFM images corresponding to these temperatures are presented in Figure 4-5 (a-d). It is evident that the films exhibit different morphologies at different annealing temperatures. Careful inspection of the AFM images of these films reveals that the films annealed at 90°C displayed a relatively large and uniform crystals with less pinholes. In contrast, the films

annealed at 60°C and 120°C show similar large grain but non-uniform crystals with more pinholes, while the films annealed at 150°C exhibit smaller crystals.

The quantitative measure of surface roughness can be obtained from AFM image analysis using NanoScope software. Figure 4-5 e) presents the calculated RMS roughness, showing the lowest surface roughness of 21 nm obtained from the films annealed at 90°C. A smooth surface encourages a well-defined interface and minimise formation of pinholes, preferred for solar cell fabrication to obtain improved performance. In summary, all the above data analysis indicates that 90°C is the optimal annealing temperature for fabrication of MAPbI₃ films.

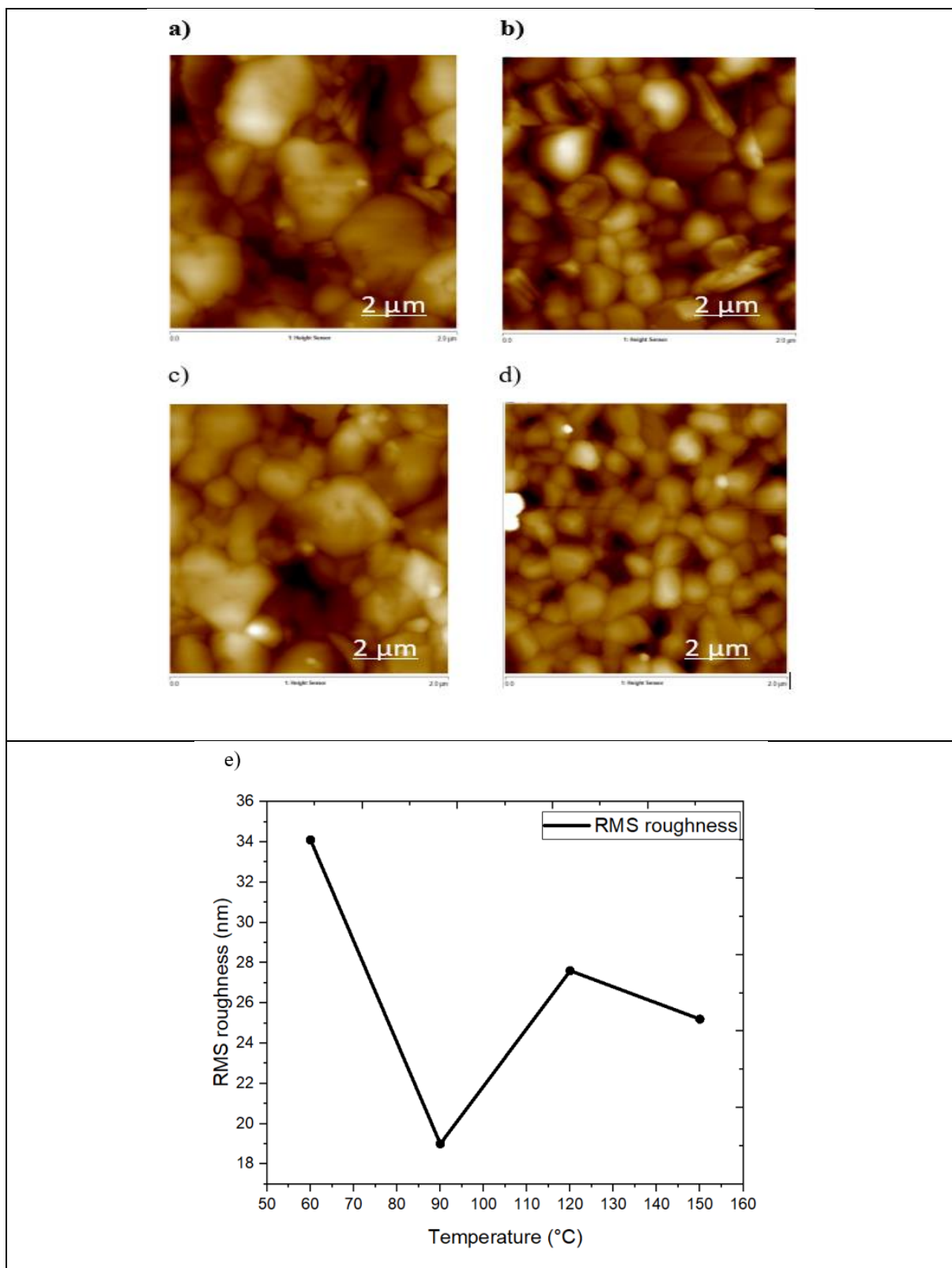


Figure 4-5 a-d) AFM topography images of MAPbI₃ at different annealing temperatures e) RMS roughness of MAPbI₃ film vs annealing temperatures

4.3.2 Optimising spin-coating speed of MAPbI₃ layer

The spin-coating speed is anticipated to have significant impact on the formation of the MAPbI₃ films. This experiment investigates the influence of spin-coating speed on the quality of the MAPbI₃ films in order to identify the optimal spin-coating speed. The MAPbI₃ layers and perovskite solar cells were fabricated and their photovoltaic parameters (i.e., V_{OC} , J_{SC} , P_{max} , FF, R_s and R_{sh}) were determined.

4.3.2.1 Film and device fabrication

Fabrication of MAPbI₃ films and photovoltaic devices followed the same procedures and conditions outlined in section 4.3.1.1, with the only difference in the spin-coating speed. The MAPbI₃ films were prepared at a spin-coating speed of 2000 rpm, 3000 rpm, 4000 rpm and 5000 rpm, respectively. The annealing temperature was fixed at 90°C.

4.3.2.2 Result and discussion

Table 4-3 presents the results of the experiment, showing the some correlations between the spin-coating speed and photovoltaic parameters of the fabricated perovskite solar cells. Despite the photovoltaic parameters of the devices are affected many factors, the results shows a clear influence of the spin-coating speed on the short-circuit current density, J_{SC} , which increases initially with increasing the spin-coating speed to reach a peak value of 23.22 mA/cm² at 4000 rpm and then decreases with further increasing the spin-coating speed. It appears that the spin-coating speed has less impact on the other photovoltaic parameters. As a result, the maximum power output and hence the PCE also follow the same trend, with an improved value of 8.67 mW/cm² obtained. This result indicates that the spin-coating speed at 4000 rpm is a favourable value for preparation good quality MAPbI₃ layers.

Table 4-3 Photovoltaic parameters of the perovskite devices fabricated using the MAPbI₃ layers prepared at different spin coating speeds ("Best" denotes the data obtained from the best-performing devices and "Ave" denotes the average performance of 16 PSCs and the area of each device is 0.15 cm²)

Speed (rpm)	V _{oc} (V)	J _{sc} (mA/cm ²)	P _{max} (mW/cm ²)	FF	R _s (Ω)	R _{sh} (KΩ)
2000 (Best)	0.92	14.69	6.58	48	106	2.2
(Ave)	0.72±0.25	13.60±1.04	4.16±2.40	37.00±8.00	186±103	1.14±1.06
3000 (Best)	0.86	17.16	8.45	57	75	50.0
(Ave)	0.80±0.07	14.86± 6.41	5.36±2.38	48.83±15.09	170±90	19±25
4000 (Best)	0.86	23.22	8.67	43	27	6.7
(Ave)	0.85±0.01	20.56±1.98	7.95±0.63	46.00±5.16		3.6±2.5
5000 (Best)	0.74	22.01	7.66	47	160	2.2
(Ave)	0.70±0.17	16.14±4.64	4.44±2.81	37.00±8.58	280±250	1.5±0.50

Figure 4-6 shows the J-V characteristics of the best-performing devices fabricated using the MAPbI₃ layers at different spin coating speeds. The J_{sc} value of 23.22 mA/cm² obtained at spin-coating at 4000 rpm is approaching the typical value of good quality perovskite devices reported. However, its corresponding V_{oc} is noticeably smaller than the typical value of 1.07 V. On the other hand, the device fabricated at a spin-coating speed of 2000 rpm shows a larger V_{oc} of 0.92 V but much smaller J_{sc}. Considering both have similar order of R_s and R_{sh}, it is likely that the small J_{sc} in the device fabricated at 2000 rpm has a poorer light absorption. The devices fabricated at a spin-coating speed of 5000 rpm exhibit a significantly reduced V_{oc} but a large J_{sc}. It appears that optimal spin-coating speed is a compromise between V_{oc} and J_{sc}.

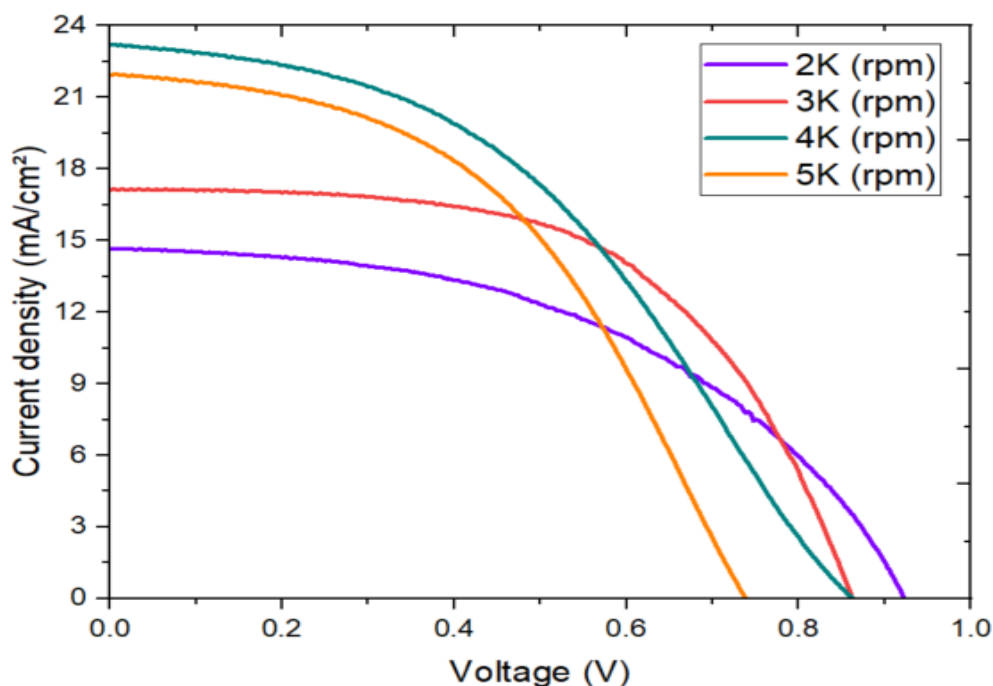


Figure 4-6 J-V characteristics of the best devices as a function of different spin coating speeds

Figure 4-7 a) presents the absorbance spectra of the MAPbI₃ films deposited on FTO/SnO₂ using spin-coating at a speed of 2000, 3000, 4000, and 5000 rpm, respectively. The results show that the MAPbI₃ films obtained good absorption for all spin-coating speeds investigated, with only a small difference. In fact, only the film prepared at a speed of 2000 rpm exhibits a slightly low curve in visible region, which may explain the lowest J_{SC} obtained in the devices fabricated at this speed.

Figure 4-7 b) shows the Tauc plots of the corresponding MAPbI₃ films. The plots were constructed using the same sets of data of Figure 4-8 a), which reveal that the energy band gap of these films is around at around 1.58 and 1.59 eV. Clearly, within the investigated range, the spin-coating speed has little impact on the energy band gap of the films. On the other hand, the J_{SC} of the devices showed a strong correlation to the spin-coating speed. The results suggest that large variations in J_{SC} among these devices are likely to due to the difference in charge transport and collection, rather than charge generation.

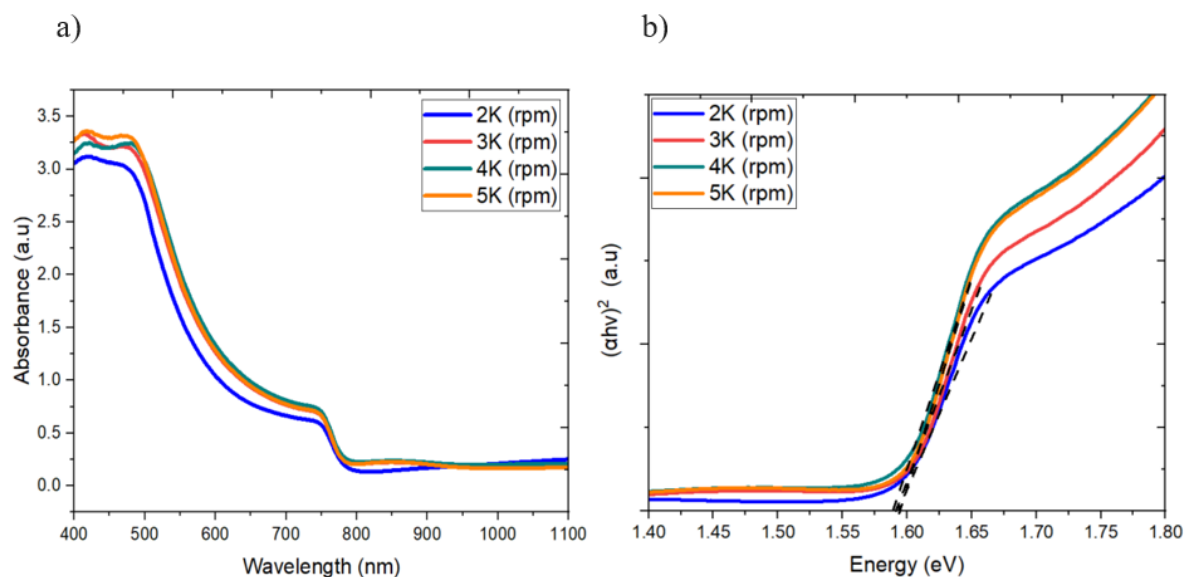


Figure 4-7 a) MAPbI₃ absorbance spectra at various spin coating speeds. b) MAPbI₃ Tauc plot as a function of different spin coating speed

Figure 4-8 a) presents XRD pattern of the MAPbI₃ films prepared using four different spin-coating speeds (i.e., 2000, 3000, 4000, and 5000 rpm, respectively). All films exhibit characteristic XRD peaks of MAPbI₃ crystals, with sharp and strong peaks centred at 14.58°, 20.40°, 28.98°, and 32.44° corresponding to the planes (110), (210), (220), and (305). These results confirm that the fabricated films have the same preferential orientation and good crystallinity. Figure 4-8 b) shows the Full Width at Half-Maximum (FWHM) data of the corresponding films. It is interesting to note that the films fabricated at a speed of 4000 rpm exhibit a small FWHM compared with the films prepared at other three speed (i.e., 2000, 3000, and 5000 rpm). A small value of FWHM corresponds to a larger grain size of crystals. This, in turn, leads to better charge transport, contributing to the observed high J_{sc} in the devices fabricated at a speed of 4000 rpm.

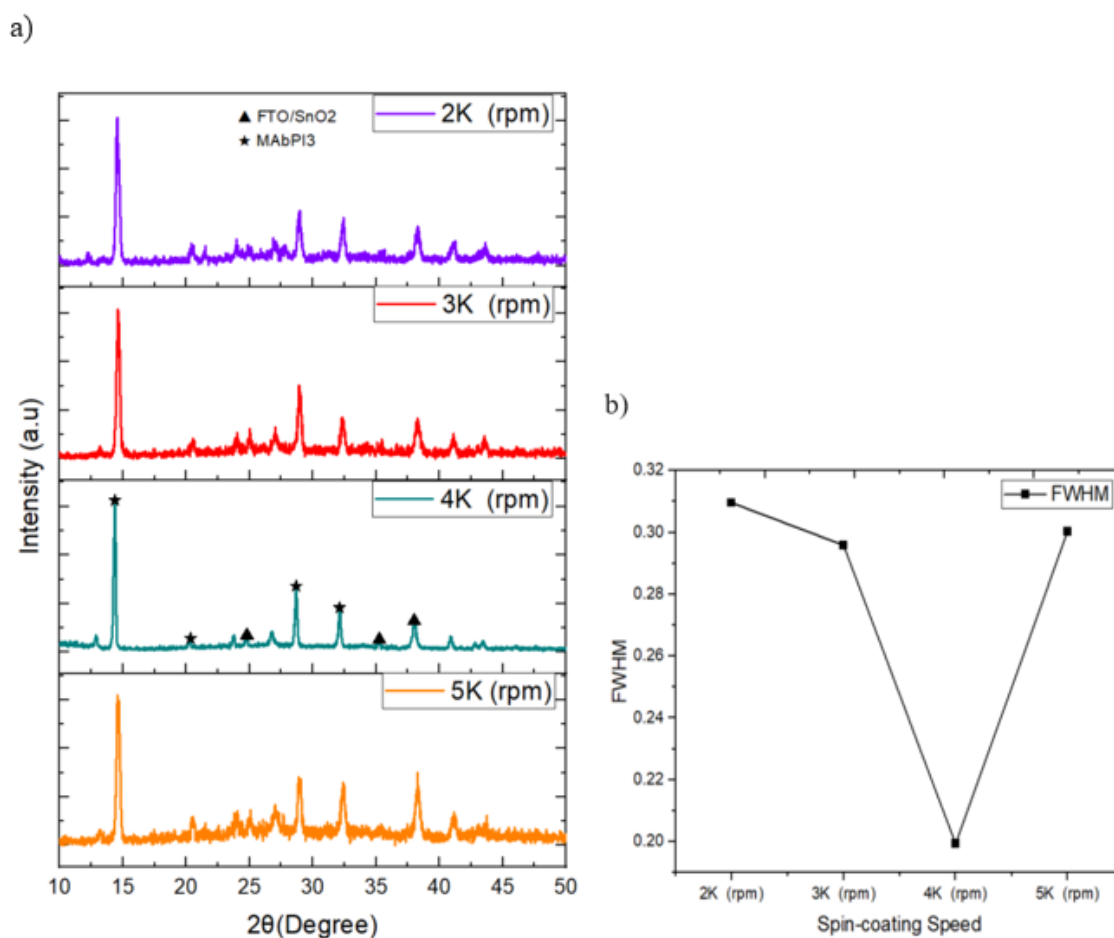


Figure 4-8 a) XRD spectra of FTO/SnO₂ / MAPbI₃ prepared at different spin-coating speeds. b) The full width at half-maximum (FWHM) of the MAPbI₃ peaks vs spin-coating speed.

The influence of the spin-coating speeds on the surface morphologies of the films was further examined using AFM. The results are shown in Figure 4-9 (a-d). The images of all films display similar crystalline morphology. Nevertheless, some variations were observed as the spin-coating speed changing from 2000 rpm to 5000 rpm. The films prepared at a spin-coating speeds of 2000 and 3000 rpm appeared to be rough with deep pits, while these fabricated at speed of 4000 and 5000 rpm appeared to be more uniformity and less rough. The observation was confirmed by the quantitative analysis of the surface roughness using NanoScope software as shown in Figure 4-9 e). It can be seen that the films fabricated at a spin-coating speed of 4000 rpm has the lowest roughness value. A less-rough MAPbI₃ layer facilitates better quality contact with other thin films, which in turn improves the charge

transport across interfaces and hence a high J_{sc} in the devices fabricated at a speed of 4000 rpm.

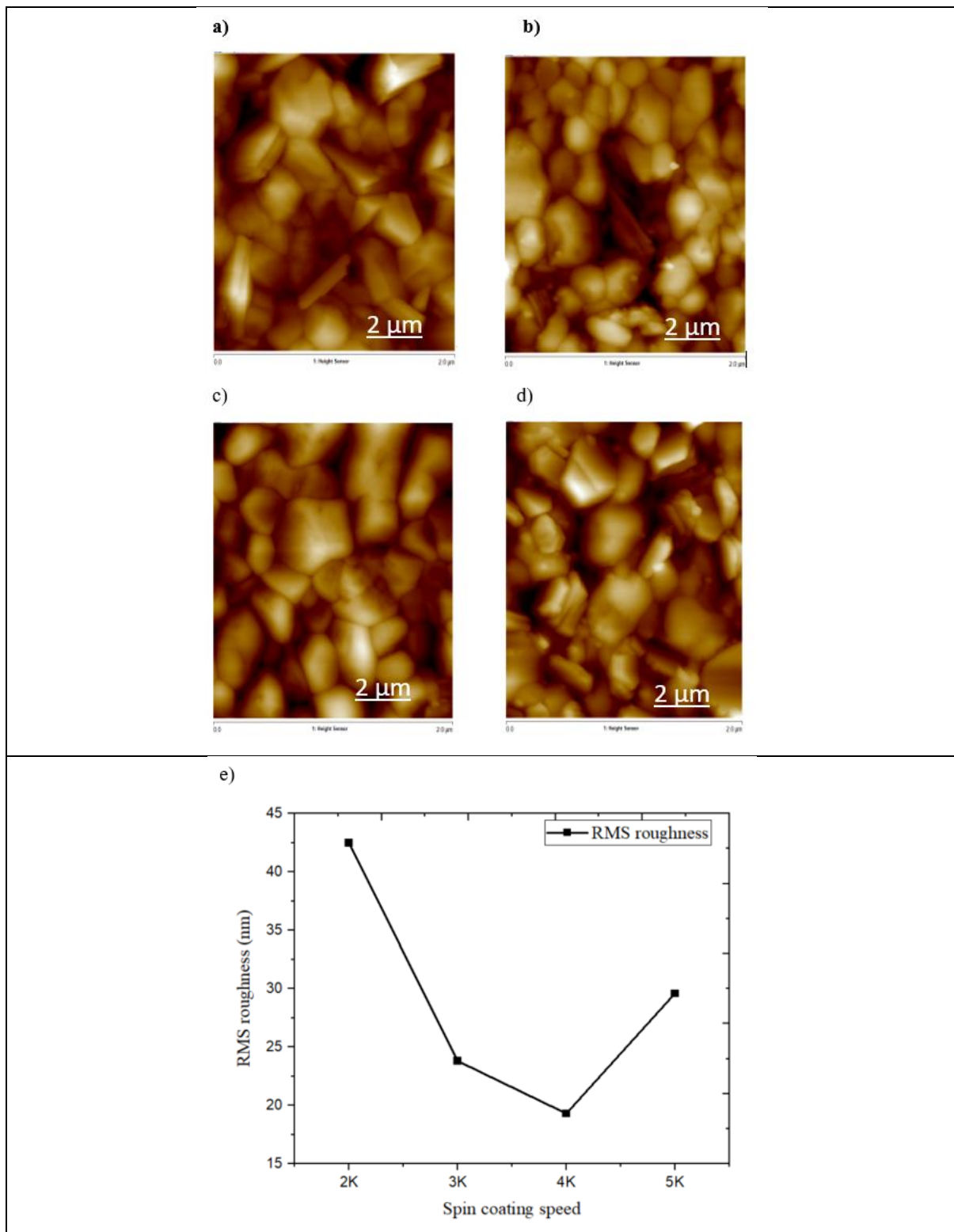


Figure 4-9 (a-d) AFM images of MAPbI₃ at different spin coating speed. e) RMS roughness of MAPbI₃ film vs different spin coating speed.

In summary, the experimental results and data analysis obtained in this study provide sufficient evidences to conclude that the optimal spin-coating speed for preparing good quality MAPbI₃ layers is 4000 rpm. However, it should be noted that this conclusion is only valid for the specific fabrication procedures and conditions described in this study.

4.3.3 Treatment of MAPbI₃ layer with various antisolvents

Antisolvent treatment plays an important role in preparation of MAPbI₃ layer, particularly crucial for fabrication in ambient air. This experiment investigates the effect of various antisolvents on the photovoltaic parameters of MAPbI₃ perovskite solar cells. The purpose is to identify the suitable antisolvents for fabrication of good quality MAPbI₃ layers.

4.3.3.1 Film and device fabrication

The fabrication of MAPbI₃ layers and devices followed the same procedures and conditions outlined in section 4.3.1.1, except for using different antisolvents. These include methyl acetate (MA), methyl formate (MF), ethyl acetate (EA), ethanol (EtOH), toluene (TL), and chlorobenzene (CB), respectively. Each of these antisolvents has unique properties that influence the quality and performance of the perovskite layers. Methyl acetate and ethyl acetate, for example, are particularly suitable for fabrication in air due to their rapid evaporation rates which help in forming high-quality films under ambient conditions. During the spin-coating, 0.15 mL of a specific antisolvent was carefully applied onto the MAPbI₃ film after the initial 15 seconds. All fabrication processes were conducted in ambient air. I-V curves of the fabricated devices were measured, and the photovoltaic parameters were extracted from the I-V curves for analysis.

4.3.3.2 Result and discussion

Figure 4-10 presents the measured J-V curves of the best performing devices obtained for different antisolvent treatments. It appears that the antisolvent treatments do not cause large variations in photovoltaic parameters of the fabricated devices for the

antisolvents used in this experiment. Nevertheless, it can be seen that the devices treated using methyl acetate, or methyl formate, or ethyl acetate exhibits slightly better I-V curve (in terms of photovoltaic performance) than those treated with ethanol, or toluene or chlorobenzene.

Table 4-4 displays the photovoltaic parameters extracted from the measured I-V curves of the devices treated by different antisolvents mentioned above. The table listed both the values from the best performing devices and the average values of the batches. The average values shows a similar trend of the photovoltaic performance of the devices to the antisolvent used for the treatments, indicating that methyl acetate, methyl formate and ethyl acetate are more suitable for fabrication of better quality MAPbI₃ layers in ambient air. Although all these antisolvents have been reported to be beneficial in making good quality MAPbI₃ crystals, the results of this experiment show that some are more suitable for fabrication in ambient air due to their capability to minimise reaction between the moisture and perovskite crystals.

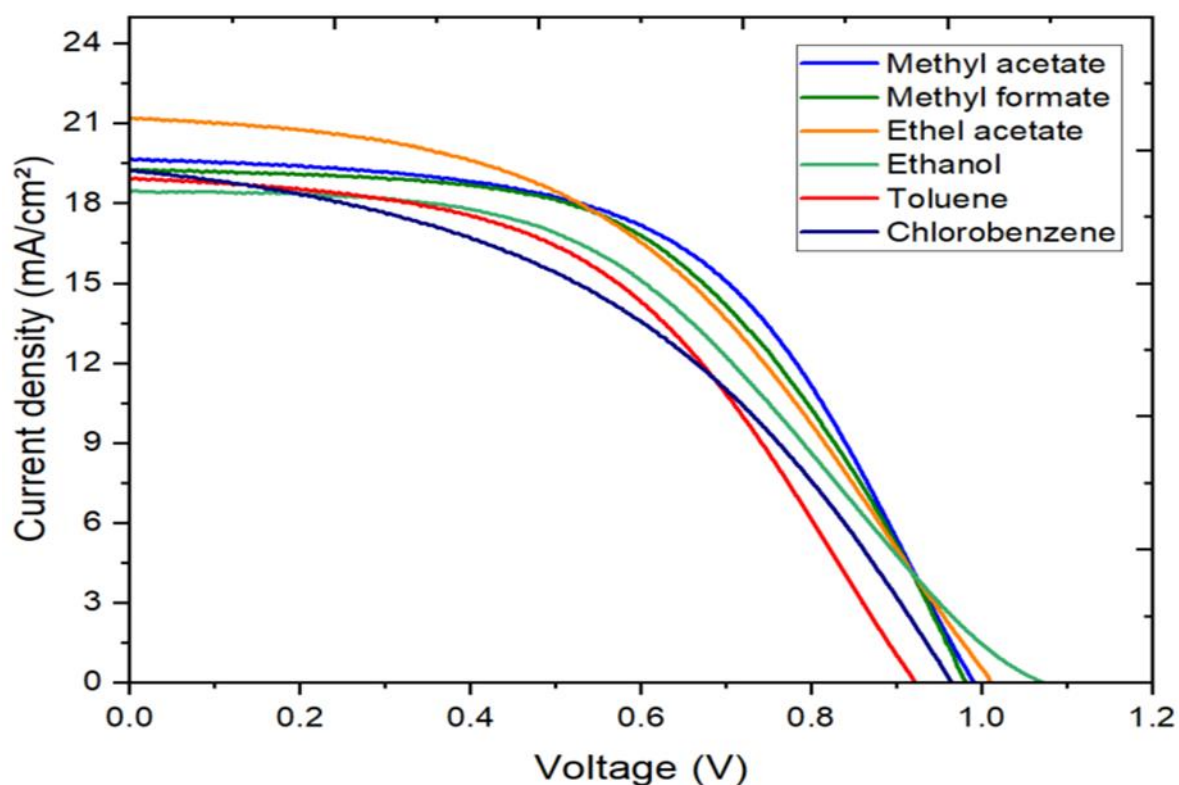


Figure 4-10 J-V characteristics of the best performing devices treated using different antisolvents

Table 4-4 Photovoltaic parameters of the perovskite devices treated using different antisolvent ("Best" denotes the data obtained from the best-performing devices and "Ave" denotes the average performance of 16 PSCs and the area of each device is 0.15 cm^2).

Antisolvent	V_{oc} (V)	J_{sc} (mA/cm ²)	P_{max} (mW/cm ²)	FF	R_s (Ω)	R_{sh} (K Ω)
MA (Best)	0.99	19.66	10.63	55	117	13
(Ave)	0.96 \pm 0.05	19.35 \pm 1.44	9.77 \pm 0.83	52.9 \pm 3.6	94 \pm 20	6.9 \pm 4.4
MF (Best)	0.98	19.30	10.18	54	103	50
(Ave)	0.97 \pm 0.06	19.20 \pm 1.47	9.88 \pm 0.45	53.3 \pm 4.8	99 \pm 36	14 \pm 20
EA (Best)	1.01	21.20	9.96	46	156	7
(Ave)	0.95 \pm 0.06	21.06 \pm 1.83	9.62 \pm 0.35	38.23 \pm 3.18	132 \pm 19	5 \pm 1.55
EtOH (Best)	1.07	18.50	9.07	46	400	5
(Ave)	1.00 \pm 0.06	17.33 \pm 2.03	8.16 \pm 1.00	45.70 \pm 2.4	205 \pm 132	5.6 \pm 0.8
TL (Best)	0.92	18.96	8.61	50	143	4.2
(Ave)	0.90 \pm 0.06	16.30 \pm 3.58	6.87 \pm 1.16	47.59 \pm 2.73	123 \pm 21	3.2 \pm 0.74
CB (Best)	0.97	19.30	8.14	44	131	2
(Ave)	0.87 \pm 0.11	18.07 \pm 2.02	7.11 \pm 1.00	42 \pm 6.2	144 \pm 54	8.20 \pm 17

Figure 4-11 (a) shows the UV-vis absorption spectra of the MAPbI₃ films deposited on FTO/SnO₂ and treated by different antisolvent. Over the UV-visible spectrum range of 400 to 1100 nm, the MAPbI₃ films treated with methyl acetate exhibits highest light absorption, compared to the films treated using other antisolvents. As a polar solvent, methyl acetate has a high solubility for perovskite precursors of lead iodide (PbI₂) and methylammonium iodide (MAI), ensuring the efficient dissolution of perovskite precursors and promoting nucleation and crystal growth [193]. This led to sufficient light absorption and a large J_{sc} , resulting in the highest P_{max} of 10.63 mW/cm² among all devices investigated.

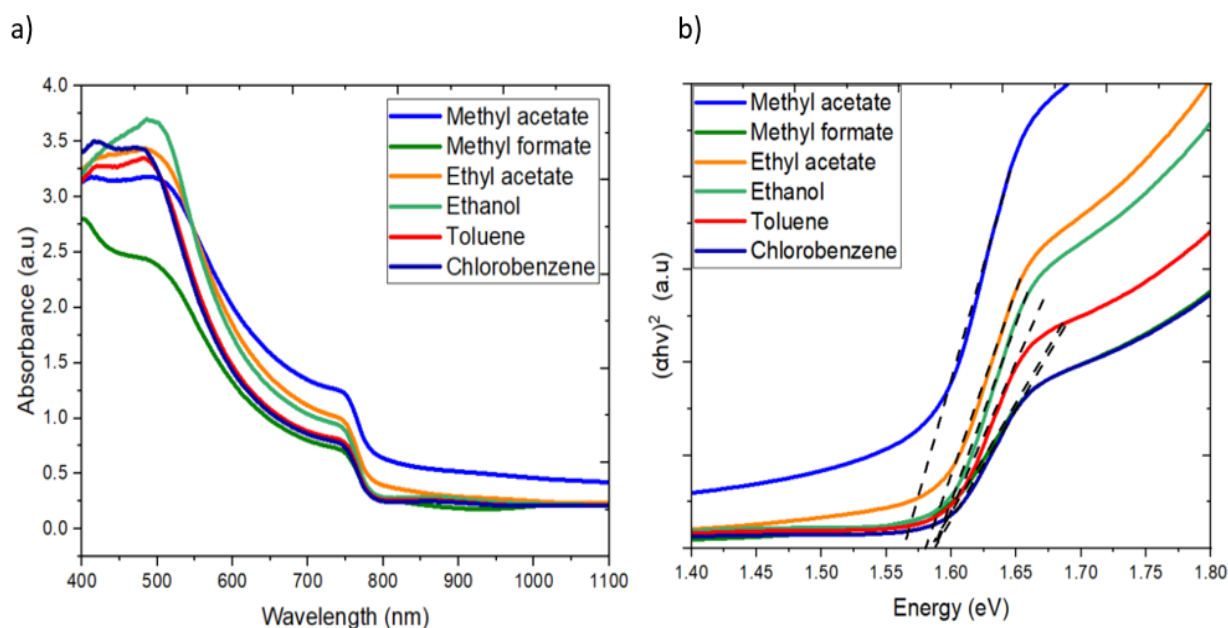


Figure 4-11 a) Absorbance of MAPbI₃ films treated by different antisolvents. b) Tauc plots of the MAPbI₃ films treated by different antisolvents.

Figure 4-11 a) provides direct evidence that the absorption characteristics of the MAPbI₃ layers can be affected by antisolvent treatment and it varies by using different antisolvents. In general, higher light absorption corresponds to more effective generation of charge carriers. Therefore, the photoactive layers with high absorbance is preferred to solar cell applications. It can be seen that methyl acetate, methyl formate and ethyl acetate exhibit large absorbance over the visible light spectrum compared to chlorobenzene, toluene and ethanol. Therefore, methyl acetate, methyl formate and ethyl acetate are considered preferred antisolvents for fabrication of MAPbI₃ layers in ambient air.

Figure 4-11 b) shows the Tauc plots of the MAPbI₃ films treated using different antisolvents, on which the energy gap of the corresponding films can be determined. It can be seen that the energy bandgap of the MAPbI₃ films is between 1.58 eV and 1.59 eV, except for the MAPbI₃ films treated using methyl acetate. The energy bandgap of the films treated using methyl acetate has a bandgap of 1.56 eV, which enables absorption of the photons at longer wavelength, enhancing charge carrier generation.

The XRD spectra of the MAPbI₃ films treated with different antisolvents is presented in Figure 4-12 a), in which two most distinctive peaks of MAPbI₃ crystals can be

seen at 14.62° and 29.0° , corresponding to the (110) and (220) planes, respectively. These peaks are sharp and well-defined, indicating formation of MAPbI_3 crystals aligned mainly in these directions for all the films regardless the type of the antisolvent used for treatment. It can also be seen that the perovskite peaks are narrower in the films treated using methyl acetate, methyl formate, toluene and chlorobenzene. This is clearly displayed in Figure 4-14 b), where the FWHM values of the highest XRD peaks were obtained for different antisolvents. The FWHM values of the XRD peaks are indicative of the crystalline quality and grain size. Among the examined antisolvents, the films treated with methyl acetate display the smallest FWHM, indicating good crystalline quality with large grains. Similarly, it can be said about the films treated by methyl formate, toluene, and chlorobenzene, which also have small FWHM values (only slightly higher than methyl acetate). In contrast, the films treated with ethyl acetate and ethanol exhibit relatively larger FWHM values, suggesting smaller crystalline size [213]. These results demonstrated clearly the influence of antisolvent treatment on the structural properties of the MAPbI_3 films. The choice of antisolvent plays a role in the crystalline quality and grain size of the fabricated perovskite layers, which is important for optimising the performance of the devices[214].

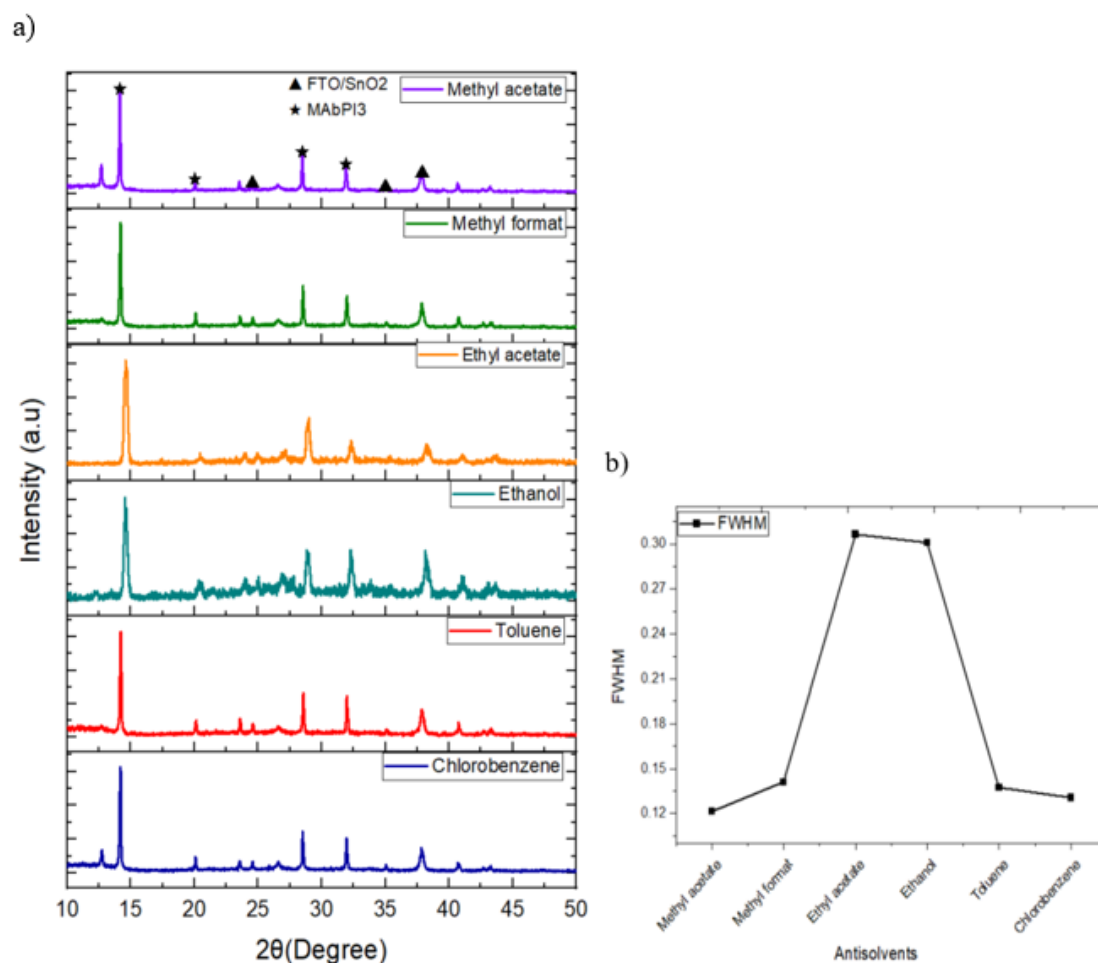
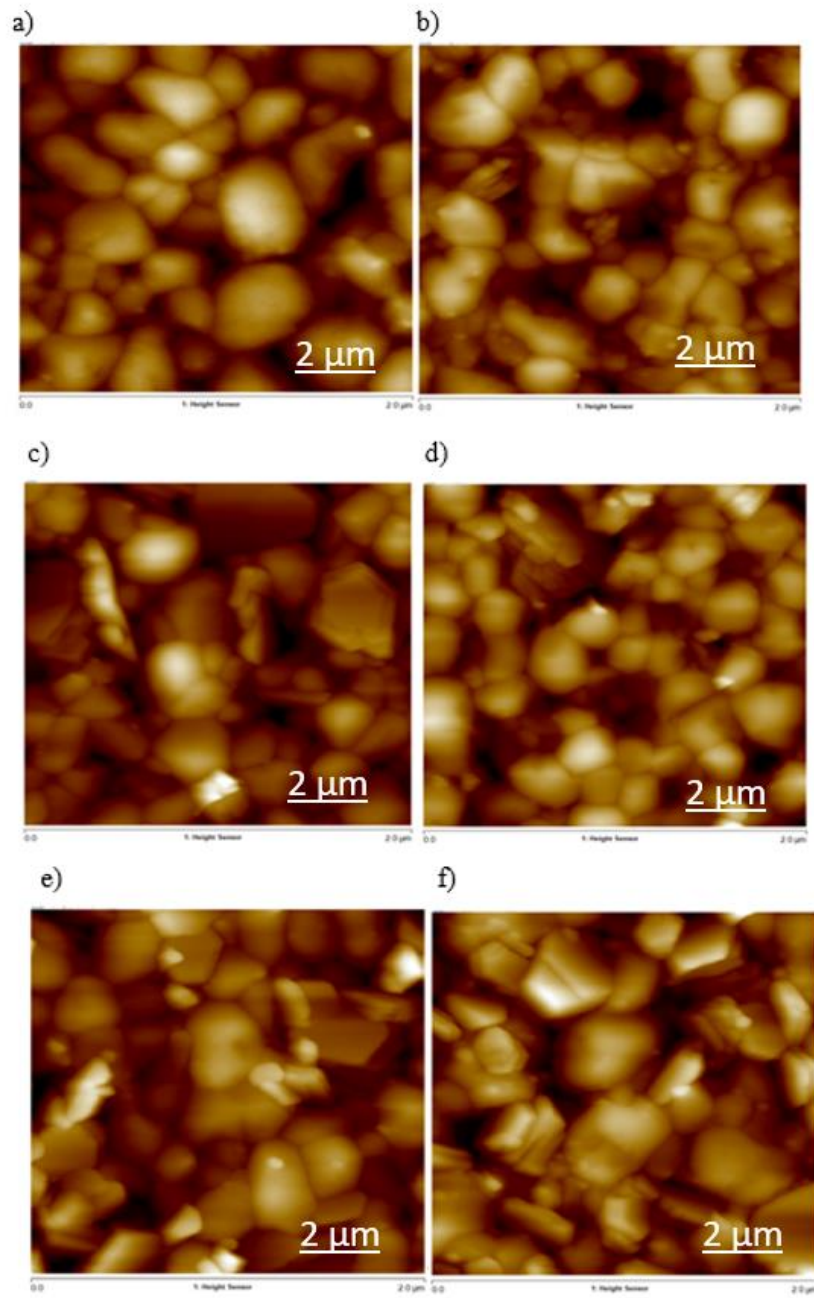


Figure 4-12 a) XRD spectra of the MAPbI₃ layers on FTO/SnO₂ substrates with different antisolvent treatment b) FWHM values of the XRD peaks of the MAPbI₃ films treated using different antisolvents.

Figure 4-13 (a-f) present AFM images of the MAPbI₃ films on FTO/SnO₂ substrates, showing nanoscale surface morphology of the films prepared using various antisolvents. The images show that all substrates are completely covered by reasonable dense crystals with grain size in a range of 200 nm to 500 nm. It is noted that the preferred grain size for perovskite solar cells is around 400 nm. It can be seen that the films treated with methyl acetate display an overall better surface morphology in terms of grain size, uniformity, density, smooth grain edges and surface roughness, contributing to better photovoltaic performance of the devices. Compared to methyl acetate, the films treated with other antisolvents display a morphology with less uniform grain size, less smooth grain edges and poor surface roughness with more pinholes.



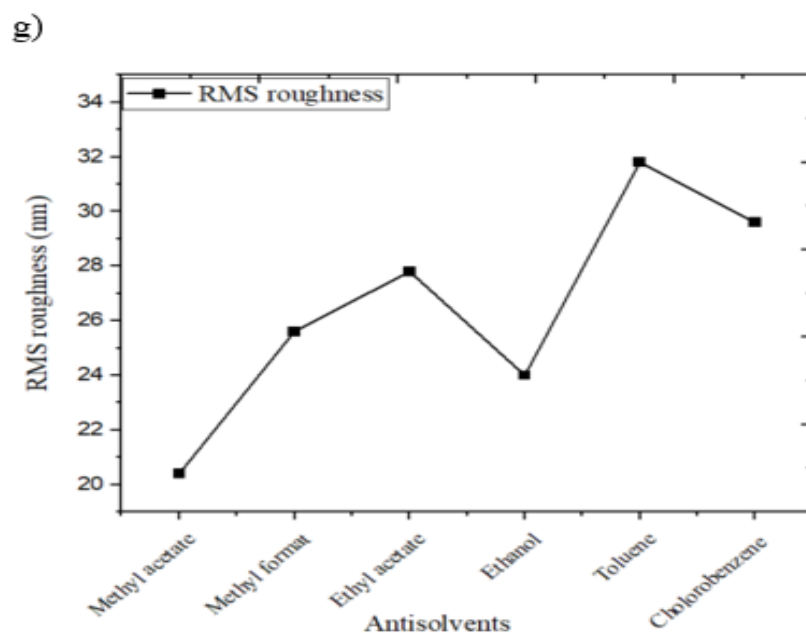


Figure 4-13 AFM images of MAPbI₃ films treated by a) methyl acetate, b) toluene, c) ethyl acetate, d) ethanol, e) methyl formate and f) chlorobenzene; g) RMS roughness of corresponding MAPbI₃ films.

Figure 4-13 g) presents the Root Mean Square (RMS) roughness values of the corresponding films obtained through AFM analysis using NanoScope software. The results show that the surface roughness is affected by different antisolvent treatment. Among the investigated antisolvents, methyl acetate exhibited the lowest RMS roughness at 20.4 nm, indicating a smooth surface. On the other hand, toluene and chlorobenzene displayed significantly higher RMS roughness values of 31.8 nm and 29.6 nm. A rough surface requires a relative thicker HTL to completely cover the perovskite layer, which will lead to a reduction in photovoltaic performance of the devices. Clearly, the choice of antisolvent affects the surface quality of perovskite films, which in turn affect the performance of perovskite solar cells. The findings from this experiment provide useful information in selecting suitable antisolvent treatment for fabrication of high quality perovskite layers.

4.4 Effect of humidity on device performance

During the initial work to establish fabrication procedures and determine appropriate processing conditions/parameters (sections 4.2 and 4.3), a significant number of devices have been fabricated in a uncontrolled environment of ambient air (approximately 160 devices), where the humidity was monitored but not controlled. The analysis of the initial results led to a speculation on a possible correlation between the humidity levels and the performance of perovskite solar cells. To confirm this speculation, the performance (P_{\max}) of the initially fabricated devices were plotted against the relative humidity level under which the devices were fabricated. The results are shown in Figure 4-14. It can be seen that the highest performance was achieved from the devices fabricated within a relative humidity of 35% to 45%. When the humidity is below 30% or beyond 50%, the performance of the devices is clearly reduced. In particular, the performance of the devices is significantly reduced when the humidity is higher than 60%. This result indicates that the high humidity has a detrimental impact on the performance of the devices fabricated using the procedures and conditions described in sections 4.2 and 4.3. Considering the frequently high humidity weather in the UK, it is beneficial to explore the suitable fabrication conditions for making good quality perovskite solar cells under high humidity environment. To my knowledge, no effort has been made and reported in this aspect. This knowledge gap provides a motivation that led to a research effort described in the next chapter.

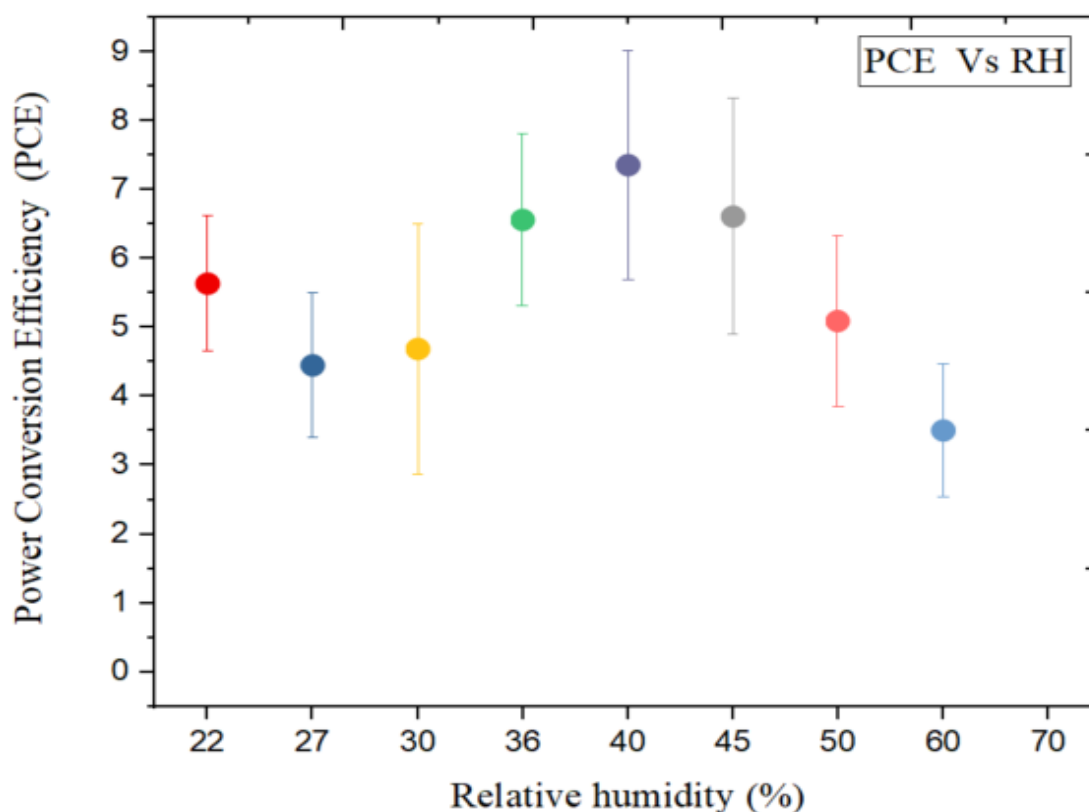


Figure 4-14 Improvements in power conversion efficiency comparing to relative humidity

4.5 Summary

This investigation focused on establishing in-air fabrication procedures for perovskite solar cells, with a primary emphasis on the fabrication of the perovskite active layer. Initial fabrication procedures were explored and established, involving cleaning the substrate, spin-coating photoactive and charge transport layers, and depositing metal electrodes. Through evaluation of the performance of the fabricated devices, the issues and challenges of the initial fabrication procedures was identified and subsequent systematic investigations were performed in order to identify the optimal fabrication conditions/parameters, aiming at fabricating the devices with improved efficiency and stability.

Systematic investigations focused on fabrication of high quality MAPbI_3 layer. The experimental results show that the annealing temperature have significant impact on the quality of the MAPbI_3 layers and the optimal annealing temperature is 90°C . This conclusion was supported by further data analysis of UV-Vis absorption, XRD patterns, and AFM images.

The study on spin-coating speed reveals that the films prepared at a speed at 4000 rpm produced the best MAPbI₃ layers among all other spin-coating speeds investigated. The study also show that the antisolvent treatment plays a role in the quality of the MAPbI₃ layer and consequently the performance of the devices. The outcome of this research indicates that methyl acetate and methyl formate are suitable antisolvents for in-air fabrication.

Additionally, the results of this work revealed a clear pattern on how the humidity level affect the quality of MAPbI₃ layers under uncontrolled fabrication environments. For a device fabricated in an uncontrolled environment, the best performance is obtained when the relative humidity level is between 35% and 45%. There is a need to explore the possibility of fabricating high performance perovskite solar cells under high humidity conditions.

Chapter 5: Fabrication under high relative humidity

5.1 Introduction

Fabrication of high-performance perovskite solar cells has encountered many enduring difficulties thus far, with a significant factor being their intrinsic sensitivity to humidity. This problem was clearly highlighted in Figure 4-14 of the previous chapter. The perovskite solar cells fabricated under high humidity of > 60% has a significantly reduced power output (P_{\max}), compared to these fabricated under a humidity between 35% and 45%. High humidity indicates more water vapour in the environment where the photoactive layers were prepared. To minimise the influence of the water vapor during fabrication, conventional strategy is to ensure a water-vapor-free environment, which inevitably increase the fabrication cost. To realise fabrication in uncontrolled environment, other strategies has to be sought. Antisolvent treatment has proved a promising countermeasures. In this chapter, an advanced approach by using a mixture of two different antisolvents to minimise the influence of water vapor, among other functions, were investigated in order to produce high-performance perovskite solar cells in ambient air.

5.2 Mixed antisolvent of ethyl acetate and methanol

In this section, ethyl acetate is mixed with methanol as a combined antisolvent to treat the MAPbI_3 layer during spin-coating. The rationale behind the addition of methanol to ethyl acetate solution lies in the possibility of increasing the solubility of water in the mixed solution due to a large water solubility in methanol, encouraging the water on the perovskite surface during formation to be extracted by methanol and evaporated. The different ratios of mixed solution of ethyl acetate and methanol were used to investigate their impact on the structural and photovoltaic properties of the perovskite devices. Experimental investigation was carried out to find out if this idea could work and determine the optimal ratio of the mixture if proved feasible.

The ratios selected for this study starts with pure ethyl acetate (i.e., 0% methanol), followed by incremental addition of 15%, 30%, and 45% methanol to ethyl acetate solution, respectively. The fabrication of the MAPbI₃ perovskite films was carried out in the lab when a high-humidity (> 70% RH) atmosphere was recorded.

5.2.1 Film and device fabrication

The fabrication process followed the exact same procedures described in section 3.3, except using the mixed antisolvent of ethyl acetate and methanol with a ratio of 0%, 15%, 30% and 45%, respectively. All solution-processed procedures were executed under ambient air, and the relative humidity was within the range of 70% to 75%.

5.2.2 Properties of the prepared MAPbI₃ films

The fabricated MAPbI₃ films were first characterised using UV-Vis Spectrophotometer. The absorbance spectra of MAPbI₃ films are shown in Figure 5-1(a), demonstrating clearly the effect of the ratio of the mixed solutions (ethyl acetate and methanol) on the optical properties of the treated films. Compared with the MAPbI₃ films treated with only ethyl acetate [215], the films treated using the mixed antisolvent with 30% methanol resulted in a noticeable increase in the absorbance over the whole visible light range of 400 nm to 750 nm, with a significant increase in the wavelength range of 450 nm – 500 nm. The results demonstrated the benefit of treatment using the mixed antisolvent, which improves light absorption of the MAPbI₃ films.

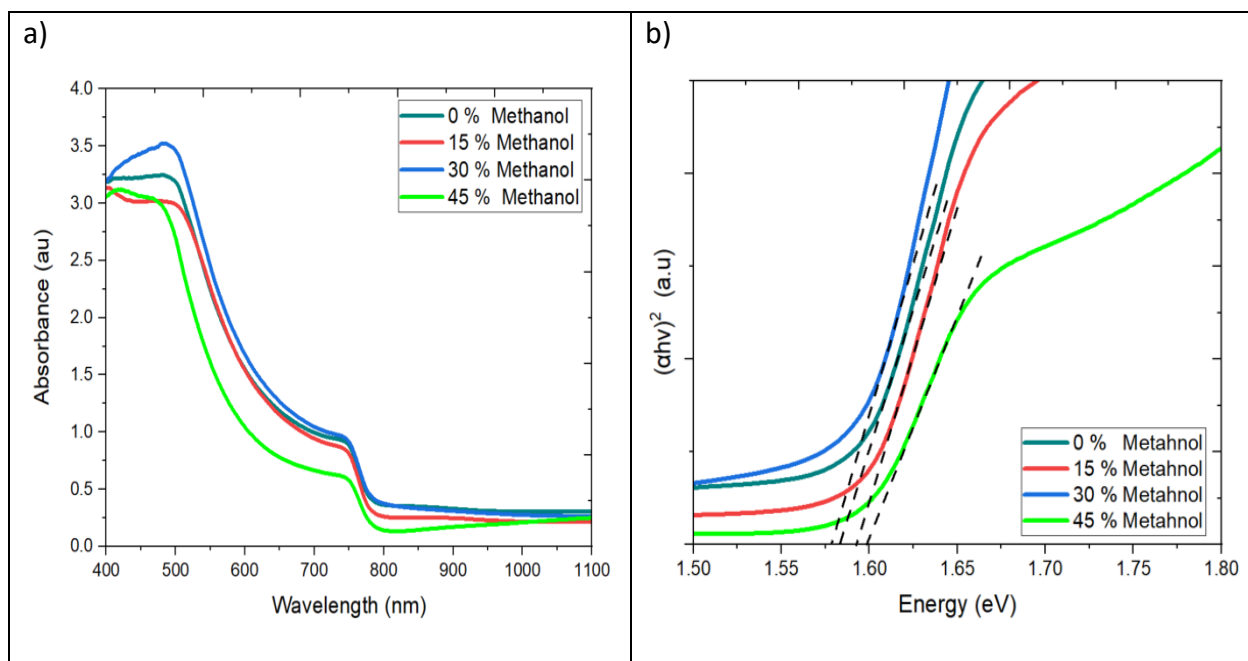


Figure 5-1 (a) Absorbance of the MAPbI₃ films treated using the mixed ethyl acetate-methanol antisolvent with a varied ratio of 0%, 15%, 30% and 40% methanol, respectively; (b) Tauc plots of the corresponding films.

The results also reveal that the ratio of the mixture is also important. The films treated using the mixed antisolvent with the ratios of 15% and 45% methanol resulted in a reduced absorbance, compared to these treated using pure ethyl acetate. It appears that the optimal ratio for the ethyl acetate-methanol mixture is around 30%. Figure 5-1(b) presents the Tauc plots of the corresponding films, which derived from the absorbance data. The results show that the energy bandgap (E_g) is slightly affected by the ratio of the mixed antisolvent. The films treated by the mixed antisolvent of 30% methanol has the lowest energy bandgap of 1.57 eV.

The XRD patterns of the fabricated perovskite films, treated using a varied ratio of the mixture at 0%, 15%, 30%, and 45% methanol, respectively, are illustrated in the Figure 5-2 (a). The characteristic peaks of the MAPbI₃ crystals are clearly present at 14.10, 28.42, 31.84, and 37.82 corresponding to the (110), (210), (222), and (225) planes, confirming the formation of crystalline perovskite films. Furthermore, a characteristic peak of PbI₂ at 12.70 can be seen

clearly in the films treated using the pure ethyl acetate solution. It is known that disassociation of the MAPbI₃ into PbI₂ phase usually take place in the presence of the moisture and water . The above observation indicates that significant formation of PbI₂ phase occurred when the films was prepared in a high humidity environment without using the mixed antisolvent. However, it can be seen from the XRD pattern that the height of the PbI₂ peak decreases with increasing the ratio of the mixed antisolvent solution, suggesting that the formation of PbI₂ phase was gradually reduced due to increased presence of methanol in the mixed solution, which prevents the water from reacting with MAPbI₃ surface. As a result, pure MAPbI₃ phase were obtained when the films were treated using the mixed antisolvent. This result provides direct evidence in support of the strategy to use mixed antisolvent for improving high quality MAPbI₃ layer fabrication in high humidity environments.

The FWHM values of XRD peaks of the corresponding films were obtained from the XRD data presented above. The results indicate the films prepared using the mixed antisolvent with a ratio of 15% and 30% methanol have large grain size compared to these prepared with a ratio of 0% and 40% methanol.

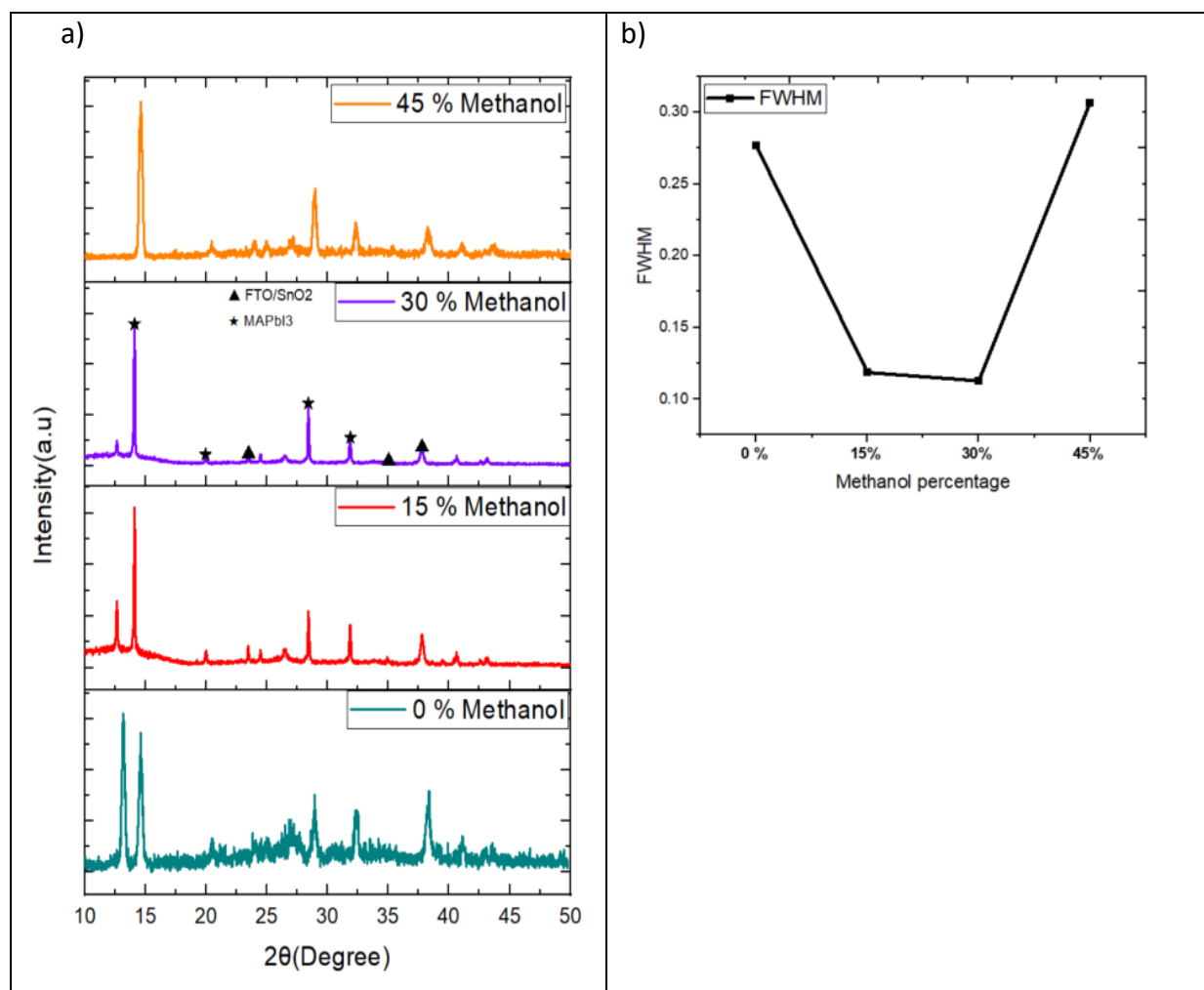


Figure 5-2 a) XRD pattern of MAPbI₃ films treated using the mixed antisolvent of ethyl acetate and methanol at the ratio of 0%, 15%, 30% and 45% methanol, respectively. b) The FWHM values of the corresponding films.

The AFM analysis was performed to examine the morphology of MAPbI₃ films, treated using the mixed antisolvents of ethyl acetate with 0%, 15%, 30%, and 45% methanol, respectively. Figure 5-3(a) presents the AFM images of the fabricated films, confirming the characteristic morphology of typical MAPbI₃ films. Notably, the films treated with the ratio with 15% and 30% methanol exhibit relatively smooth crystals with large grain size around 500 nm. In particular, the films treated with the ratio of 30% shows most smooth surface and largest, densely packed grains, which are favorite feature for high photovoltaic performance. On the other hand, the films treated with the ratio of 0% and 45% methanol show significantly smaller grain size, which is consistent with the results from Figure 5-3e).

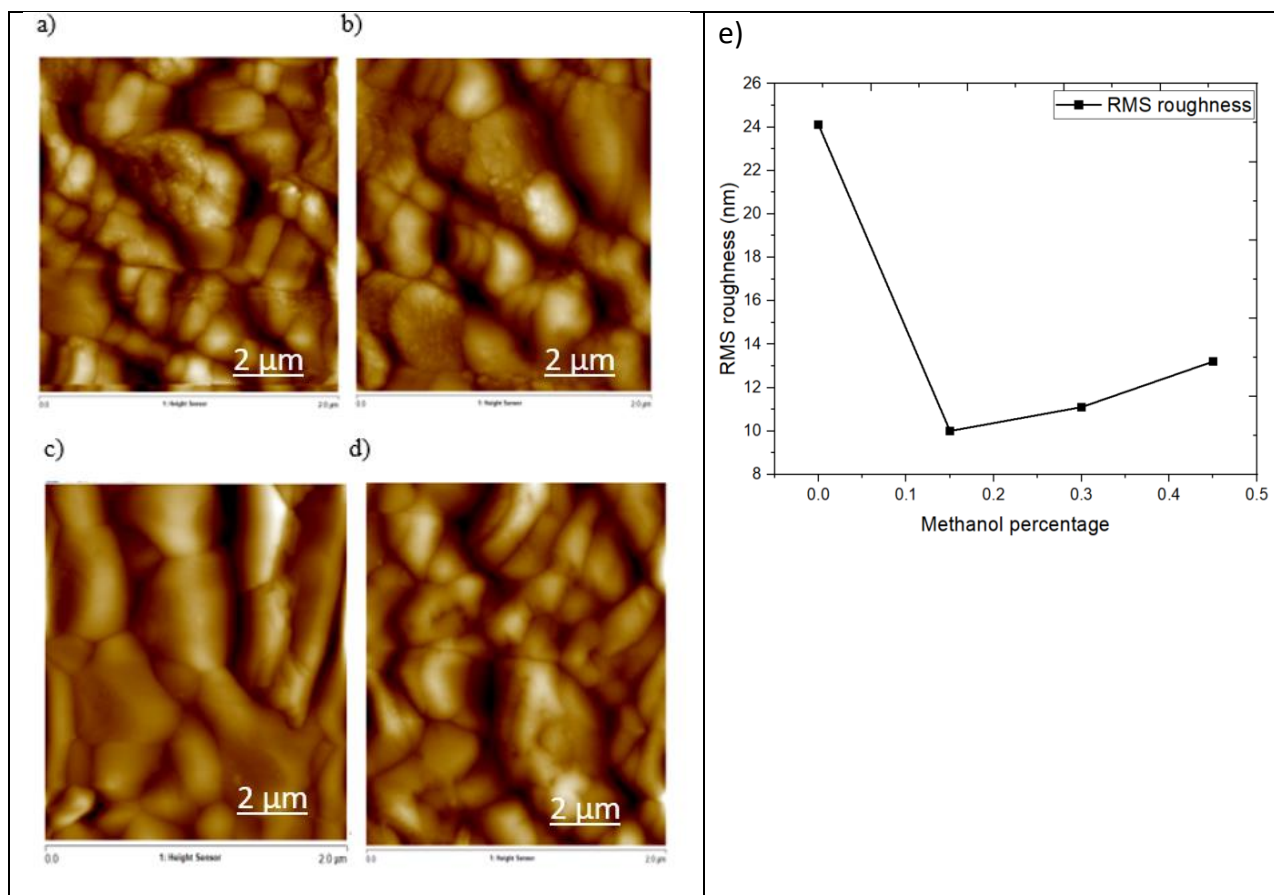


Figure 5-3 a) AFM images of MAPbI₃ with different antisolvent concentrations of Ethyl acetate and methanol. b) RMS roughness of the films

The RMS roughness of the corresponding films were determined from AFM image analysis using NanoScope software and the results are illustrated in Figure 5-3(b). It can be seen that the films treated using the mixed antisolvent have significantly reduced RMS roughness, with the lowest value of 10 nm obtained in the films treated using the ratio of 15% methanol. The RMS roughness is 11.1 nm for the films treated using the ratio of 30% methanol, offering additional benefit for using this type of mixed antisolvent treatment in fabrication of perovskite films in high humidity environments.

5.2.3 Photovoltaic performance of the devices

Figure 5-4 illustrates the J-V curves of the best-performing devices fabricated with their MAPbI₃ layers treated utilizing a mixed antisolvent of ethyl acetate and methanol, with the ratio of 0%, 15%, 30%, and 45% methanol, respectively. Clearly, all the devices treated using the mixed antisolvent exhibit better photovoltaic performance than the devices treated using ethyl acetate only, with the best performance from the devices fabricated using the ratio of the mixture at 30% methanol. This result is consistent with the outcomes of the films discussed in the above sections.

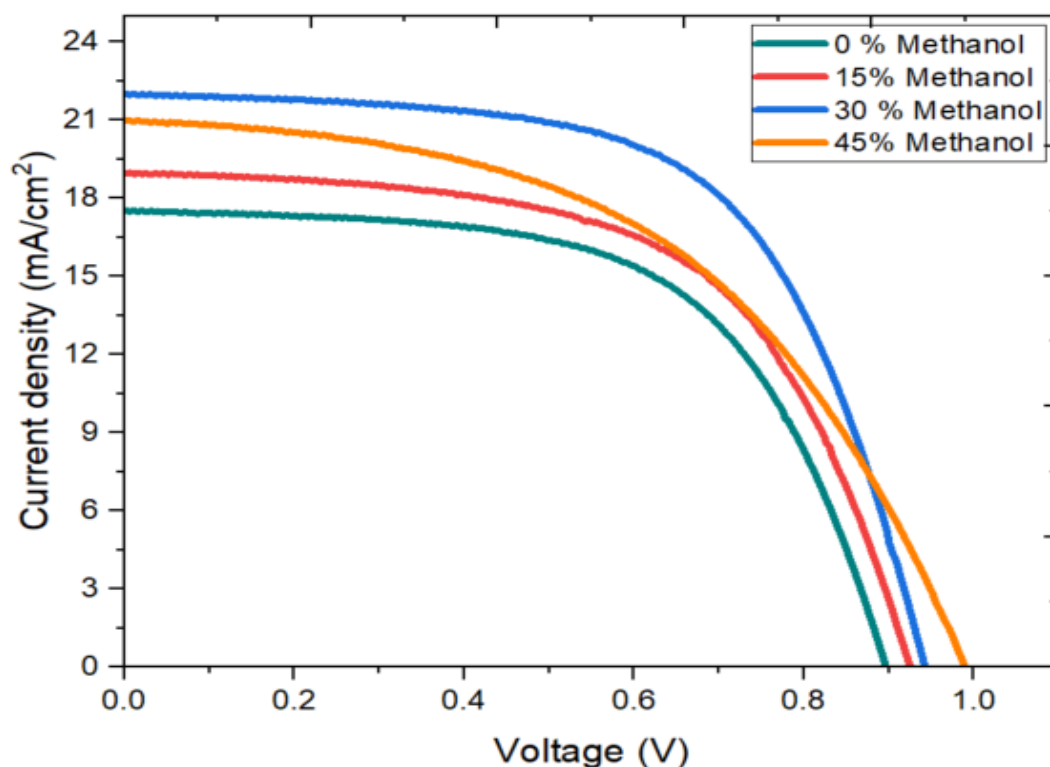


Figure 5-4 J-V characteristics of the best-performing devices fabricated using mixed antisolvent of ethyl acetate and methanol with different mix ratios.

Table 5-1 presents the key photovoltaic parameters extracted from J-V measurements, showing the data of the best-performing devices and the average values of the devices in a batch. Although the average values are generally smaller than the corresponding best-performing data, they show the similar trends in the relationship between the photovoltaic performance and the mixed antisolvent treatment. The results

show that the optimal mixture is approximately 70% of ethyl acetate and 30% of methanol (i.e., the ratio of 30% methanol), which led to a significantly improved maximum power output (P_{\max}) of 12.70 mW/cm², compared to 9.42 mW/cm² from the devices using the pure ethyl acetate antisolvent. By employing appropriate ratio of the mixture, not only the short-circuit and open-circuit voltage are increased, the FF is also improved, indicating an overall improvement in the quality of the MAPbI₃ films after mixed antisolvent treatment. This again confirms that the idea and benefits of the strategy in exploring mixed antisolvents to improve the performance of perovskite solar cells, particularly for these fabricated in high humidity environments.

on the other hand, The study demonstrates that a 30% methanol concentration in the mixed antisolvent yields optimal results for MAPbI₃ films. This ratio significantly enhances absorbance (450-500 nm range) and structural quality, as evidenced by smoother surfaces and larger grain sizes from AFM and reduced PbI₂ formation in XRD. Photovoltaic performance was highest at 30% methanol, achieving a P_{\max} of 12.70 mW/cm², a 35% improvement over pure ethyl acetate treatment. Lower (15%) or higher (45%) methanol ratios showed suboptimal results due to insufficient or excessive interaction, confirming 30% methanol as the ideal concentration.

Table 5-1 Photovoltaic parameters of perovskite solar cells fabricated using mixed antisolvent of ethyl acetate and methanol and tested under AM1.5 G illumination. ("Best" denotes the data obtained from the best-performing devices and "Ave" denotes the average performance of 16 PSCs and the area of each device is 0.15 cm^2)

Methanol percentage	V_{oc} (V)	J_{sc} (mA/cm ²)	P_{max} (mW/cm ²)	FF	R_s (Ω)	R_{sh} (K Ω)	RH(%)
0 % (Best)	0.90	17.53	9.42	60	67	3.8	70-75
(Ave)	0.90±0.02	17.61±1.70	9.12±0.45	59±10	81±32	8.2±7.3	
15% (Best)	0.93	18.99	10.32	59	66	33.3	70-75
(Ave)	0.88±0.03	19.85±0.59	10.29±0.16	59±0	62±3	13.3±13.5	
30 % (Best)	0.94	22.02	12.70	61	56	33.5	70-75
(Ave)	0.90±0.05	21.49±0.81	11.86±0.83	62±1.5	54±2.6	38.6±4.3	
45% (Best)	0.99	21.00	10.43	50	90	4.5	70-75
(Ave)	0.87±0.09	19.56±1.47	9.75±0.70	58±7	70±15	16±12.5	

5.3 Mixed antisolvent of methyl acetate and toluene

The combination of methyl acetate and toluene as a mixed antisolvent is investigated in this section. The rationale of using methyl acetate with toluene is different from the mixing of ethyl acetate with methanol investigated in previous section. Since the methyl acetate has high water solubility of 25%, it is already suitable for the use in high humidity environment to minimise the influence of moisture and water on the crystallization of the MAPbI₃ layer. However, an issue with methyl acetate is its very high polar moments, which leads to small grains. On the other hand, toluene has very small polar moments. It is expected that the mixture of methyl acetate and toluene will be able to maintain the high water solubility with smaller polar moment. The purpose of the work is to demonstrate the effectiveness of this mixed antisolvent on the quality of the MAPbI₃ films and the performance of the devices fabricated in high humidity environments.

5.3.1 Film and device fabrication

The MAPbI₃ films and devices were fabricated using the same procedures and parameters as described in section 3.3, except that the antisolvent treatment was performed using a mixed antisolvent of methyl acetate and toluene. The treatment started with pure methyl acetate (i.e., 0% toluene) and followed by varied ratios of 15%, 30%, and 45% toluene,

respectively. All solution-processed procedures were executed in ambient air and the relative humidity was within the range of 70% to 75%.

5.3.2 Properties of the prepared MAPbI₃ films

Figure 5-5 (a) displays the UV-Vis absorption spectra of the MAPbI₃ perovskite layers deposited on FTO/SnO₂ substrates and treated using the mixed antisolvent of methyl acetate and toluene with a varied ratio of the mixture. The absorbance of the films treated by the mixed antisolvent with the ratio of 30% toluene is clearly higher than the films treated using the pure methyl acetate over a wide wavelength range of 400 nm–900 nm. This result demonstrates that the light absorption can be increased by employing the mixed antisolvent treatment with the appropriate ratio of mixture, and consequently an increase in charge generation .

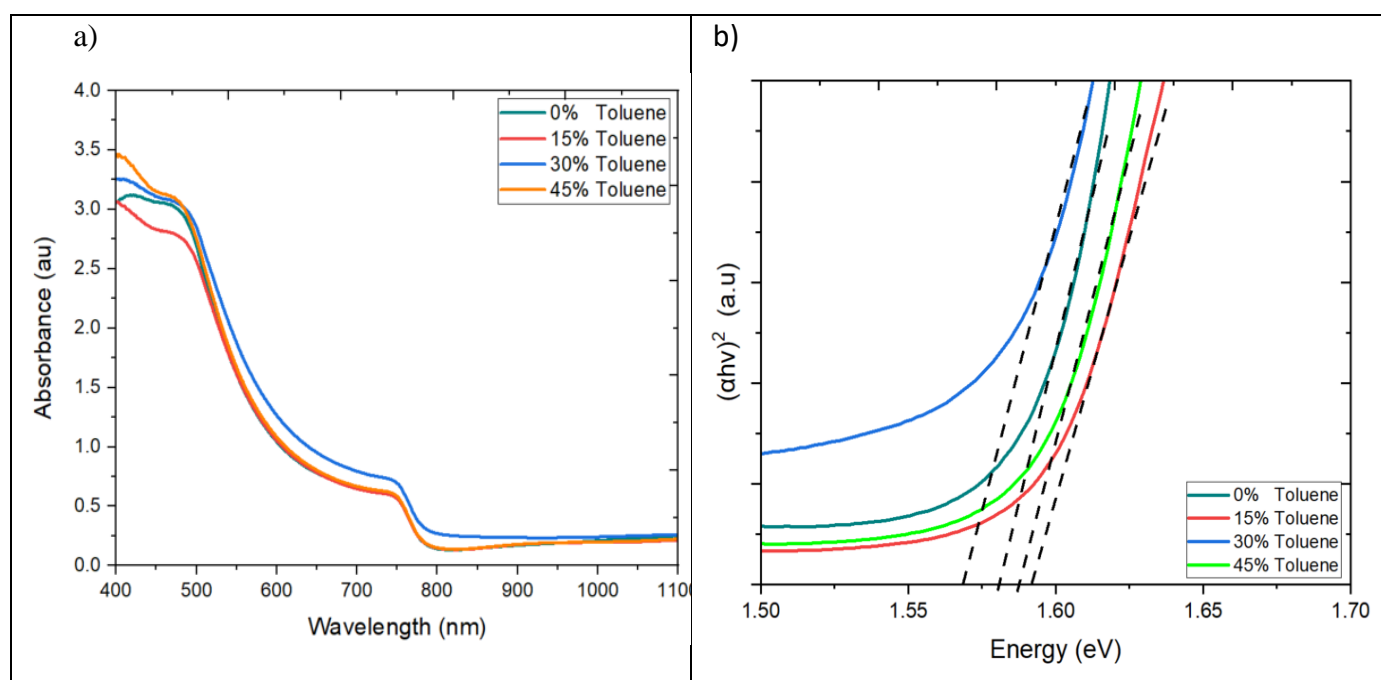


Figure 5-5 (a) The absorbance of MAPbI₃ films treated with pure methyl acetate and varying ratios of added toluene (b) Tauc plots films.

On the other hand, the films treated with the ratio of 45% exhibit only a slight increase in the absorbance while the films treated with the ratio of 15% display a decline over the

wavelength range of 400 nm - 550 nm, compared with the films treated using the pure methyl acetate. This result indicates that the observed improvement is strongly dependent on appropriate ratio of the mixture. In this case, it is around 30% of toluene.

Figure 5-5(b) presents the Tauc plots of the corresponding films, which were derived using the same data of absorbance in Figure 5-5 (a). The energy bandgap of the films can be determined from the Tauc plots. It can be seen that all films exhibit an energy bandgap of 1.57 eV to 1.59 eV. These are the values expected from typical MAPbI₃ crystals. Furthermore, the films treated using the mixed antisolvent with 30% toluene exhibit a lower *E_g* value of 1.57 eV, contributing to higher absorbance over the visible light range.

Figure 5-6 (a) presents the XRD patterns for the fabricated films treated using the mixed antisolvent of methyl acetate and toluene with varied ratios of the mixture. The peaks of 14.14°, 20.06°, 28.48° ,and 31.86° correspond to the (110), (220),(225), and (320) crystal planes of the tetragonal perovskite structure[216], [217], [218]. This confirms the formation of the MAPbI₃ perovskite crystals in these films. The XRD patterns for the films treated with the ratios of 0%, 15%, and 30% of toluene look very similar. However, the films treated with the of 45% toluene exhibit reduced heights of perovskite peaks. This may indicate that the fabricated film is thinner due to a slow crystallization when treated with high percentage of toluene.

The FWHM values of the corresponding films were determined from the XRD data and the results are shown in Figure 5-6(b). The FWHM values of the films treated using the mixed antisolvent of methyl acetate and toluene are significantly lower than that of the films treated using the pure methyl acetate (i.e., 0% of toluene), indicating that the average grain size of the perovskite crystals are increased when treated using the mixed antisolvent of methyl acetate with toluene. This outcome is in agreement with the concept of increasing the crystal grain size by reducing the polar moment of the antisolvent. As a result of increased grain size of the MAPbI₃ layer, the charge carrier transport of the devices will be improved.

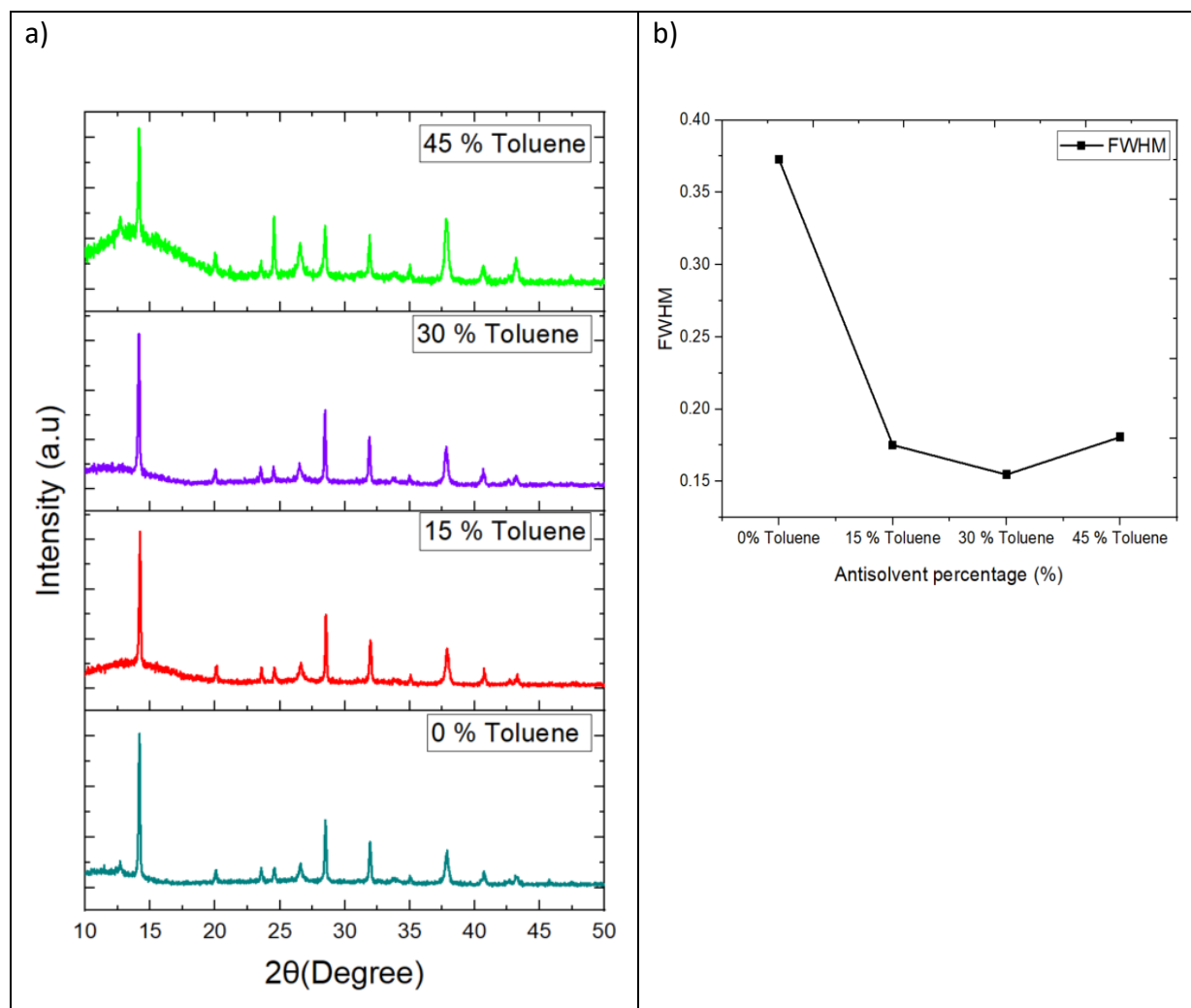


Figure 5-6 a) XRD patterns of MAPbI₃ films treated by the mixed antisolvent of methyl acetate and toluene with different ratio of mixture, b) The FWHM values of the corresponding films.

The surface of the fabricated films were examined using AFM to investigate the effect of the mixed antisolvent treatment on the morphology of the perovskite films. Figure 5-7 (a-d) presents the AFM images corresponding to antisolvent concentrations of 0%, 15%, 30%, and 45%, respectively. The films treated with the ratio of 30% toluene displays a desirable surface morphology with large and uniform grains, which is in clear contrast to small and less-uniform grains in these treated with the ratios of 0%, 15% and 45%. The RMS roughness values of these films were also determined, as shown in Figure 5-7 (b). Compared with the films treated using pure methyl acetate (i.e., 0% toluene), the surface of the films treated using the mixed antisolvent (i.e., 15%, 30% and 45%) become significant smooth, which is another desirable feature for perovskite device fabrication. Notably, larger grain size,

reduced grain boundaries, and smoother surfaces of the perovskite layer will lead to an enhancement of J_{sc} and reduction in recombination at the perovskite/charge transfer interface [219], [220], [221][219], [220], [221].

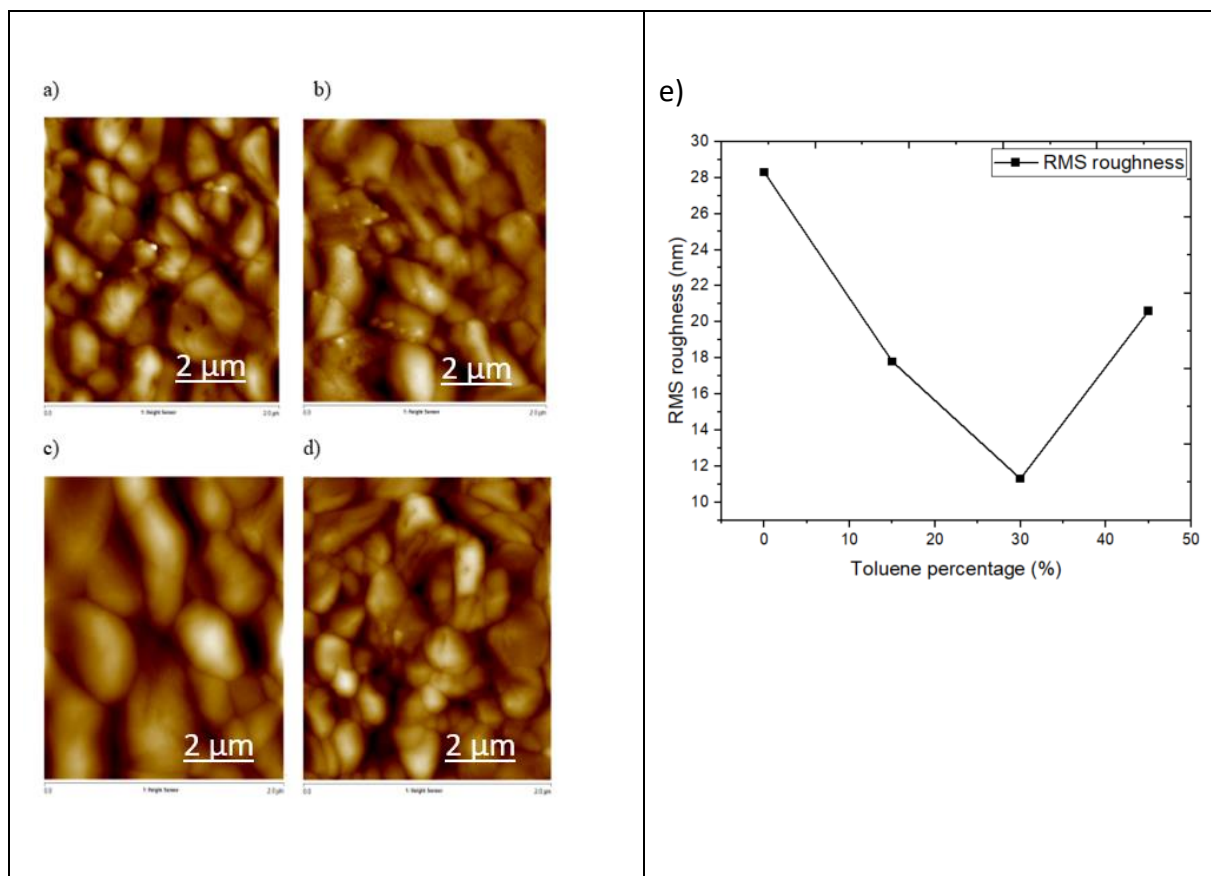


Figure 5-7 AFM images of the MAPbI₃ films treated using the mixed antisolvent with the ratio of a) 0% toluene, b) 15% toluene, c) 30% toluene, d) 45% toluene; and e) RMS roughness of the corresponding films

5.3.3 Photovoltaic performance of the devices

Table 5-2 summarizes the photovoltaic parameters of the PSCs fabricated using the mixed antisolvents of methyl acetate and toluene and tested under AM1.5 G illumination. The measured J-V curves of the best-performing devices are illustrated in Figure 5-8. The results show clearly that the devices treated with the mixed antisolvent exhibit an improved performance, compared with the devices treated using the pure methyl acetate. The highest

power output of $P_{\max} = 13.31 \text{ mW/cm}^2$ was obtained from the devices fabricated using the ratio of 30% toluene, which represents a 37% increase from the devices treated using the methyl acetate only.

Overall, the results of this investigation suggest that the mixed antisolvent treatment using methyl acetate and toluene with a ratio of 30% toluene enhances the performance of the perovskite solar cells, even at high relative humidity. This improvement is attributed to the higher absorption of the films, the larger grain size, fewer boundaries between perovskite grains, and smoother surfaces. This is consistent with the outcomes obtained from the studies of the film properties described in previous sections.

The findings of this work confirm the strategy of employing the mixed antisolvent to meet the challenging requirements that a single antisolvent cannot satisfy. In this case, the methyl acetate meets the requirement of high water solubility but has a undesirable large polar moment, which is reduced by addition of an appropriate percentage of toluene (30% in this study).

Table 5-2 Photovoltaic parameters of the PSCs fabricated using the mixed antisolvent of methyl acetate and toluene ("Best" denotes the data obtained from the best-performing devices and "Ave" denotes the average performance of 16 PSCs and the area of each device is 0.15 cm^2).

Toluene percentage	V_{oc} (V)	J_{sc} (mA/cm ²)	P_{\max} (mW/cm ²)	FF	R_s (Ω)	R_{sh} (K Ω)	RH(%)
0% (Best)	1.02	16.42	9.70	57.9	137	10	70-75
(Ave)	0.95±0.05	18.75±1.73	9.01±0.64	50.9±	119±16	2.6±4.9	
15% (Best)	1.00	16.77	10.03	59.5	112	7.2	70-75
(Ave)	0.96±0.09	18.75±2.10	8.99±1.88	50.3±10.3	90±70	5.8±4.2	
30 % (Best)	1.06	22.07	13.31	57.1	91	6	70-75
(Ave)	1.04±0.02	19.86±1.82	12.07±0.84	58.5±2.0	73±50	3.8±2.7	
45 % (Best)	0.99	19.66	10.63	54.5	118	4.8	70-75
(Ave)	0.91±0.09	19.02±2.18	9.59±0.96	55.8±8.1	82±13	2.2±2	

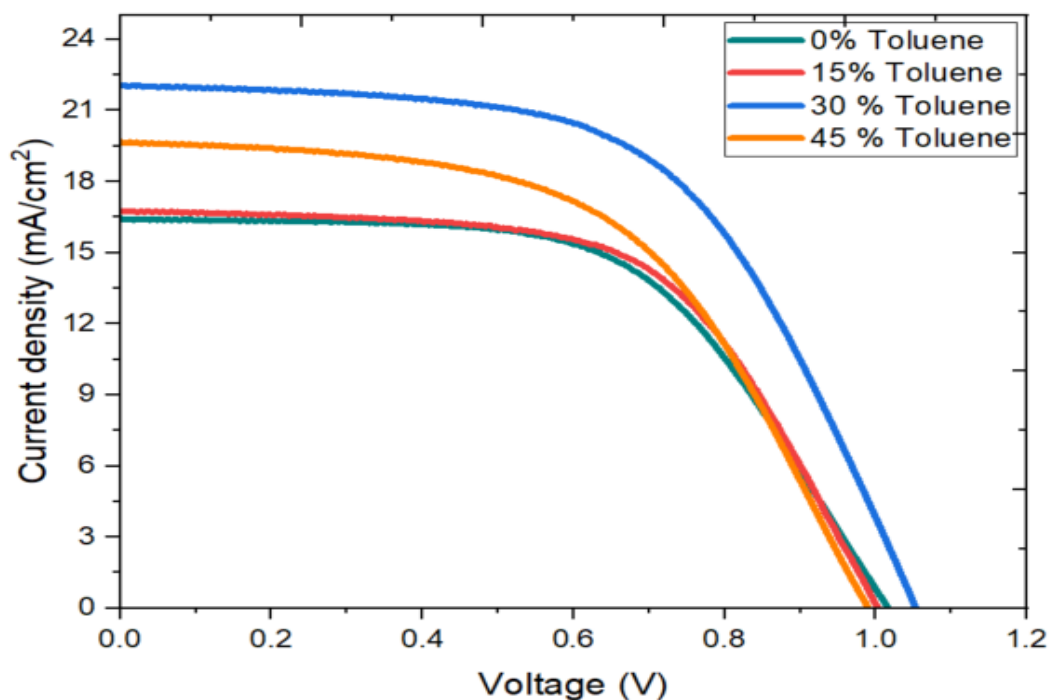


Figure 5-8 J-V characteristics of the best devices as a function of different antisolvent concentrations of Methyl Acetate and Toluene

5.4 Mixed antisolvent of methyl formate and chlorobenzene

The combination of methyl formate and chlorobenzene as an antisolvent presents a unique approach to influencing the perovskite crystallization process. Within this combination, methyl formate, acting as a polar solvent, influences perovskite crystallization, while chlorobenzene, a non-polar solvent, helps in controlling perovskite film precipitation. This combination contributes to establish equilibrium between the effects of polar and non-polar solvents, thereby creating a potentially controlled environment conducive to perovskite crystal growth. By optimizing antisolvent concentration ratios, both resulting in improve morphology and performance of the perovskite layer which can be enhanced, potentially improving the efficiency and stability of perovskite devices.

5.4.1 Film and device fabrication

The films and devices in this study were made using the same procedures and conditions/parameters (section 3.3), except that the antisolvent used for treatment of the

MAPbI₃ layers is a mixed antisolvent of methyl formate and chlorobenzene. The ratios of the mixture employed for this study are 0%, 15%, 30% and 45% chlorobenzene, respectively. All solution-processed procedures were carried out in high humidity air of 70% - 75% RH.

5.4.2 Properties of the prepared MAPbI₃ films

Figure 5-9 (a) illustrates the absorbance of the MAPbI₃ films prepared using the mixed antisolvent of methyl formate and chlorobenzene with the ratio of the mixture at 0%, 15%, 30%, and 45% chlorobenzene, respectively. The films treated with methyl formate only and those containing 15% and 30% chlorobenzene exhibited very similar absorption values, with a slightly higher performance seen in the films treated at 30% chlorobenzene. For the films treated at 45% of chlorobenzene, a marked decrease in absorption was evident. Figure 5-9(b) presents the Tauc plots of the corresponding films, showing that the mixed antisolvent treatment has little impact on the energy bandgap of the treated films.

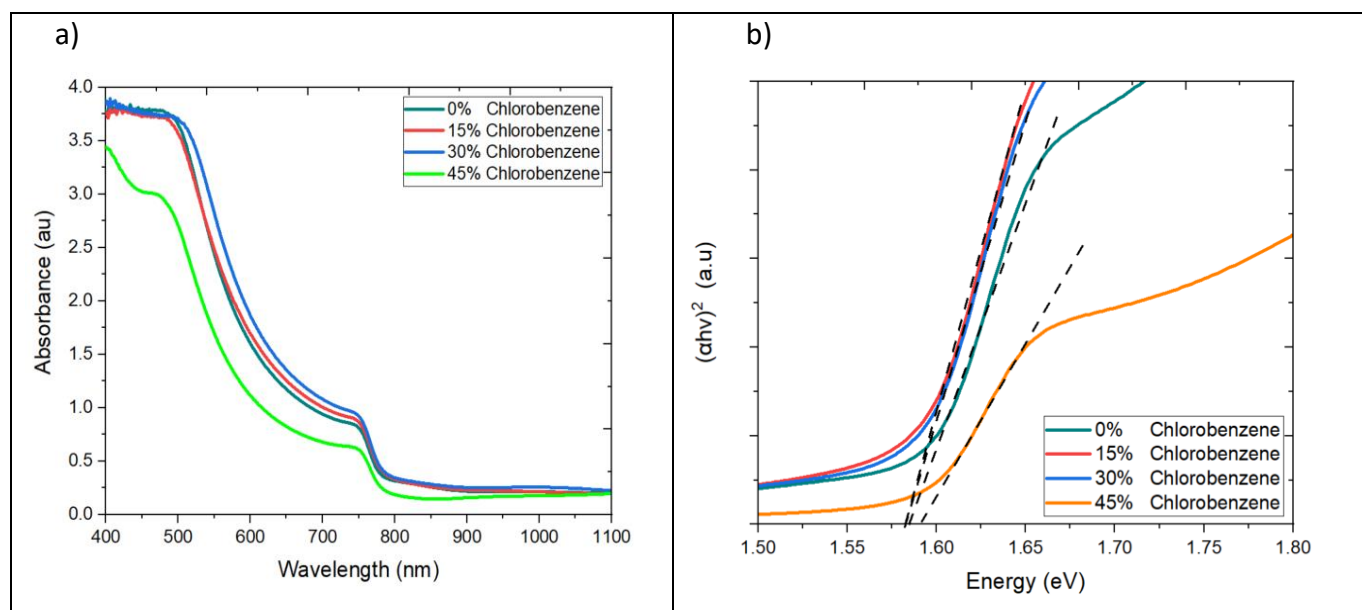


Figure 5-9 (a) Absorbance of MAPbI₃ films treated with pure methyl formate and different mixture of methyl acetate with chlorobenzene (b) Tauc plots of the corresponding films.

Figure 5-10(a) shows the XRD spectra of the MAPbI₃ films treated using the mixed antisolvent of different mixture of methyl formate with 0%, 15%, 30%, and 45% chlorobenzene, respectively. The characteristic peaks of the MAPbI₃ films can be seen clearly on the XRD pattern at 14.34°, 20.24°, 28.66°, and 32.08° for all the films, indicating formation of the MAPbI₃ crystals for all the cases investigated. It can be seen that the XRD patterns of the films treated using the mixed antisolvent with the ratio of 15% and 30% chlorobenzene are very similar to that of pure methyl acetate. This result indicates that this mixture had little influence on the crystal structure.

The intensity of the characteristic peaks are reduced for the films treated with the ratio of 45% chlorobenzene. Also, the FWHM value for this film is higher than the other films as shown in Figure 5-10 (b), indicating that the films have smaller grains. Nevertheless, the changes in this case are not significant compared to the cases described in sections 5.2 and 5.3, where different set of mixture were used. The smallest FWHM values was obtained in the films treated with the ratio of 30% chlorobenzene, indicating a relative large grain size in this film.

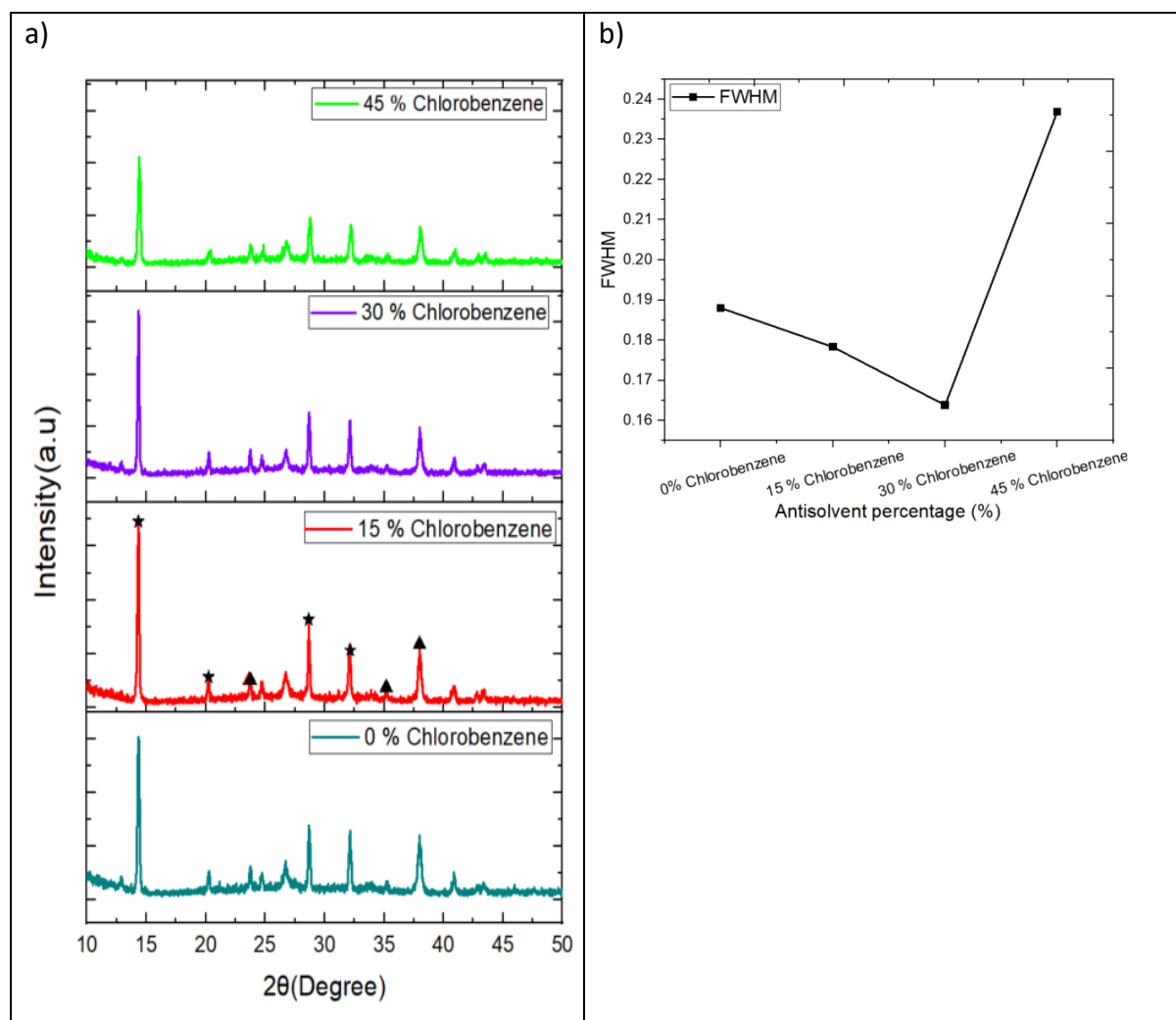


Figure 5-10 a) XRD pattern of MAPbI₃ films treated using the mixed antisolvent of methyl acetate and chlorobenzene with different ratio of mixture , b) The FWHM values as a function of the ratio of mixture.

Figure 5-11(a)-(d) present AFM images of the MAPbI₃ films treated with the ratio of 0%, 15%, 30%, and 45%, respectively. It appears that the average grain size of the MAPbI₃ crystals is increased after treatment using the mixed antisolvent. However, only the films treated with the ratio of 15% exhibit more uniform grain sizes, while the films treated at the ratio of 30% and 45% appears to show a morphology of less smooth grain surfaces consisting of small grains within large crystals. An increase in the grain size may be related to a slightly reduced dipole moment of the mixed antisolvent because the dipole moment of chlorobenzene (1.55D) is smaller than that of methyl acetate (1.77D). The RMS roughness of these films were determined as shown in Figure 5-12 (e). The films treated with the mixed

antisolvent exhibit smoother surfaces. The best result was obtained from the films treated at 30% chlorobenzene.

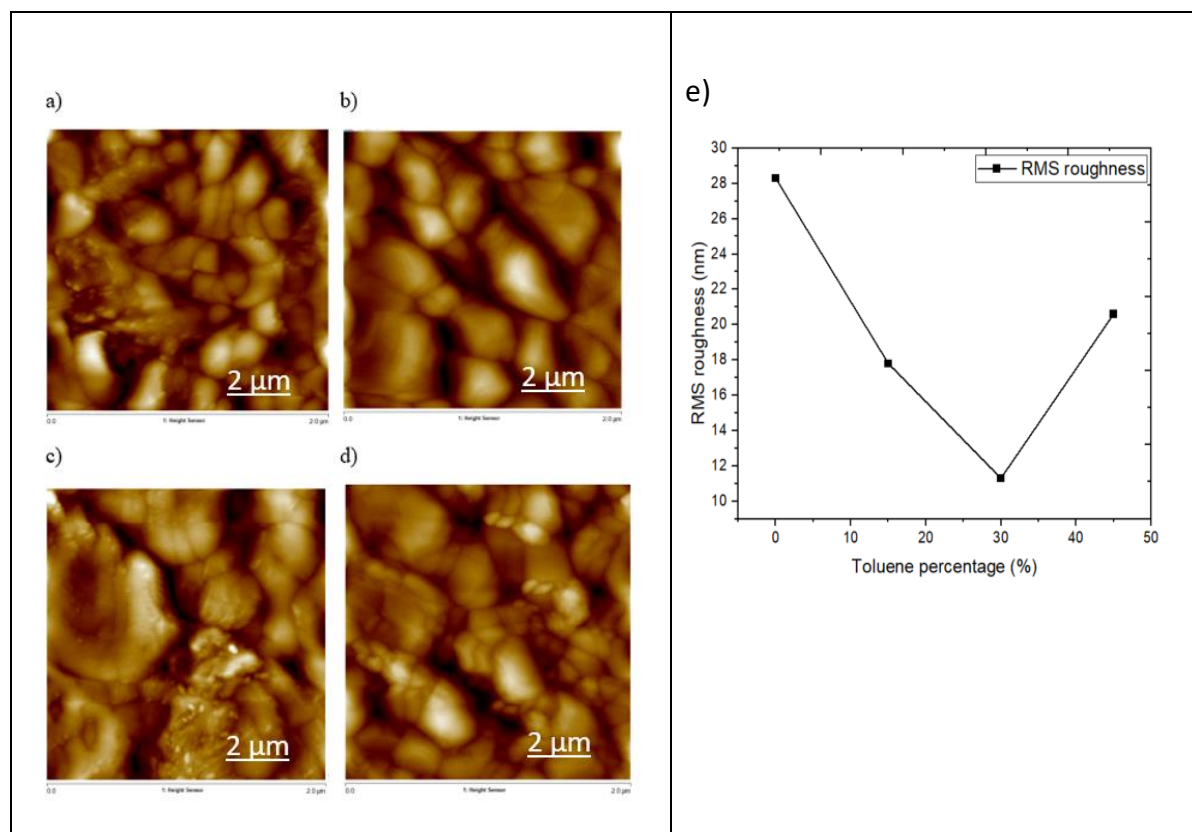


Figure 5-11 AFM images of the MAPbI₃ films treated using the mixed antisolvent of methyl acetate and chlorobenzene with different percentage of chlorobenzene at a) 0%, b) 15%, c) 30%, and d) 45%, e) RMS roughness of the films.

5.4.3 Photovoltaic performance of the devices

Figure 5-12 depicts the J–V curves of the best performing devices treated using the mixed antisolvent of methyl acetate and chlorobenzene with the varied ratio of the mixture. The corresponding photovoltaic parameters for both the best performing devices and the average values of the devices in a batch are summarized in Table 5-3. The devices treated with the ratio at 15% and 30% exhibit improvement in the maximum power output (P_{max}), with the largest value of 9.82 mW/cm² obtained from the devices treated with the ratio

of 15%. The improvement is mainly due to a significant increase in the short-circuit density. Since the absorbances (consequently the charge generation) are very similar in the devices treated with the ratio of 0%, 15%, and 30%, a large short-circuit current density obtained in the devices treated with the ratio of 15% is possibly due to the better transport in these cells, which is supported by the AFM image shown in Figure 5-11 (b), where the relatively uniform and smoother grains are evident.

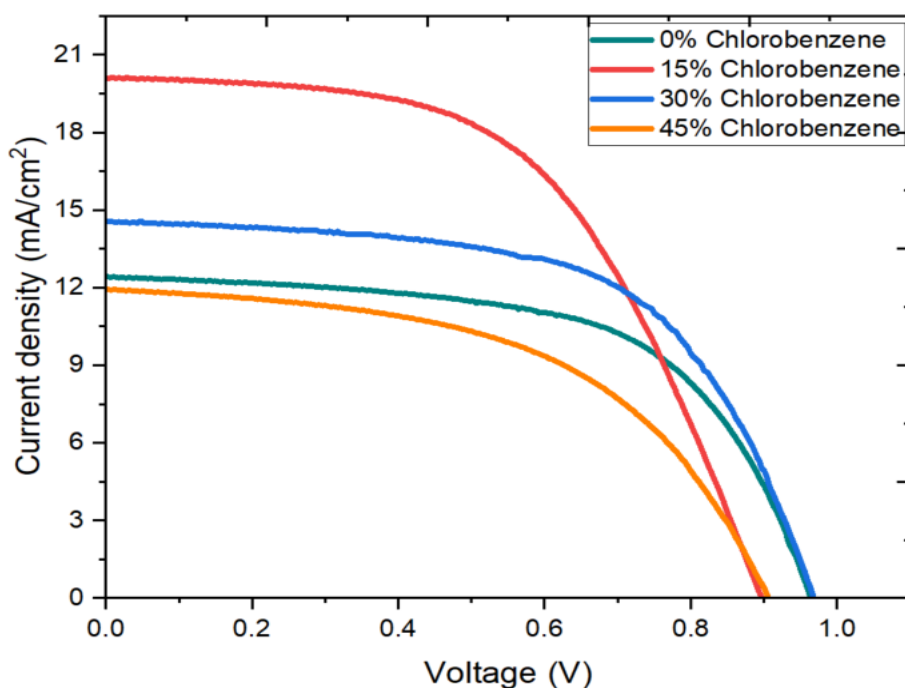


Figure 5-12 J-V characteristics of the best-performing devices treated using the mixed antisolvent of methyl acetate and chlorobenzene with a varied ratio of mixtures.

It is to be noted that the the maximum power output of the devices treated with only the methyl formate is significantly smaller in this experiment than the corresponding the value in Table 4-4. The difference is likely due to the devices prepared in this experiment were under high humidity of 70% - 75%RH, while the devices of Table 4-4 were prepared under a humidity of 22% - 55% RH. Since methyl formate has much large vapor pressure, its moisture prevent effect would be quickly lost due to fast vaporation into environment. As a result, its function as an antisolvent is more servely affected in high humidity environment.

Table 5-3 summarizes the photovoltaic performance parameters of PSCs fabricated with a methyl formate and chlorobenzene anti-solvent combination ("Best" denotes the data obtained from the best-performing devices and "Ave" denotes the average performance of 16 PSCs and the area of each device is 0.15 cm^2).

Chlorobenzenes percentage	V_{oc} (V)	J_{sc} (mA/cm ²)	P_{max} (W/cm ²)	FF	R_s (Ω)	R_{sh} (K Ω)	RH (%)
0% (Best)	0.96	12.42	7.19	60	93	7.7	72-75
(Ave)	0.90 \pm 0.06	13.47 \pm 1.54	6.82 \pm 0.86	56 \pm 3.61	56 \pm 3.6	3.1 \pm 4	
15 % (Best)	0.90	20.12	9.82	54	94	25	72-75
(Ave)	0.91 \pm 0.02	18.99 \pm 1.30	9.69 \pm 0.12	56 \pm 2	156 \pm 105	17.5 \pm 7	
30 % (Best)	0.97	14.58	8.42	60	88	5.5	72-75
(Ave)	0.91 \pm 0.06	15.38 \pm 1.90	8.36 \pm 0.59	60 \pm 3	80 \pm 24.5	11 \pm 5.2	
45% (Best)	0.90	11.94	5.64	52	126	5.6	72-75
(Ave)	0.65 \pm 0.51	10.62 \pm 7.56	5.79 \pm 4.50	41 \pm 33	65 \pm 8	1.5 \pm 0.7	

5.5 Stability of the best-performing devices

Humidity has significant influence on fabrication of perovskite solar cells. It also affects the performance of the devices during operation in ambient air. The stability of operation in humid environment is another key issues of the perovskite solar cells in terms of their practical applications. For this reason, it is useful to compare the effect of different mixed antisolvents on the stability of the fabricated devices. The best-performing devices subjected to 3 different antisolvent treatments were selected and stored in uncontrolled humidity conditions (45-75% RH) at room temperature, with J-V curves of each devices measured daily over a period of 10 days (i.e., 240 hours). Figure 5-13 illustrates the change of the maximum power output of the devices as a function of time. It can be seen that the degradation rate in the power output differs for the devices treated with different mixed antisolvents. For the devices treated using the mixed antisolvent of ethyl acetate and methanol, the power output reduced to 33.24% of its original value after 240 hour, while it reduced to only 10.90 % of the initial power for the devices treated using the mixed antisolvent of methyl formate and chlorobenzene. However, the devices treated using the mixed antisolvent of methyl acetate and toluene exhibit a relatively slow degradation rate, with its power reduced to 72.75% of the initial power remained after 240 hours. Although the

stability of all 3 devices are extremely poor in terms of practical applications, the devices treated using the methyl acetate and toluene has relatively better stability than the other two. This results demonstrated that the antisolvent treatment not only has impact on the fabrication quality but also influences the stability of the devices. Identifying suitable antisolvent, in particular, design appropriate mixed antisolvent could have benefits for both the performance and stability of the perovskite devices.

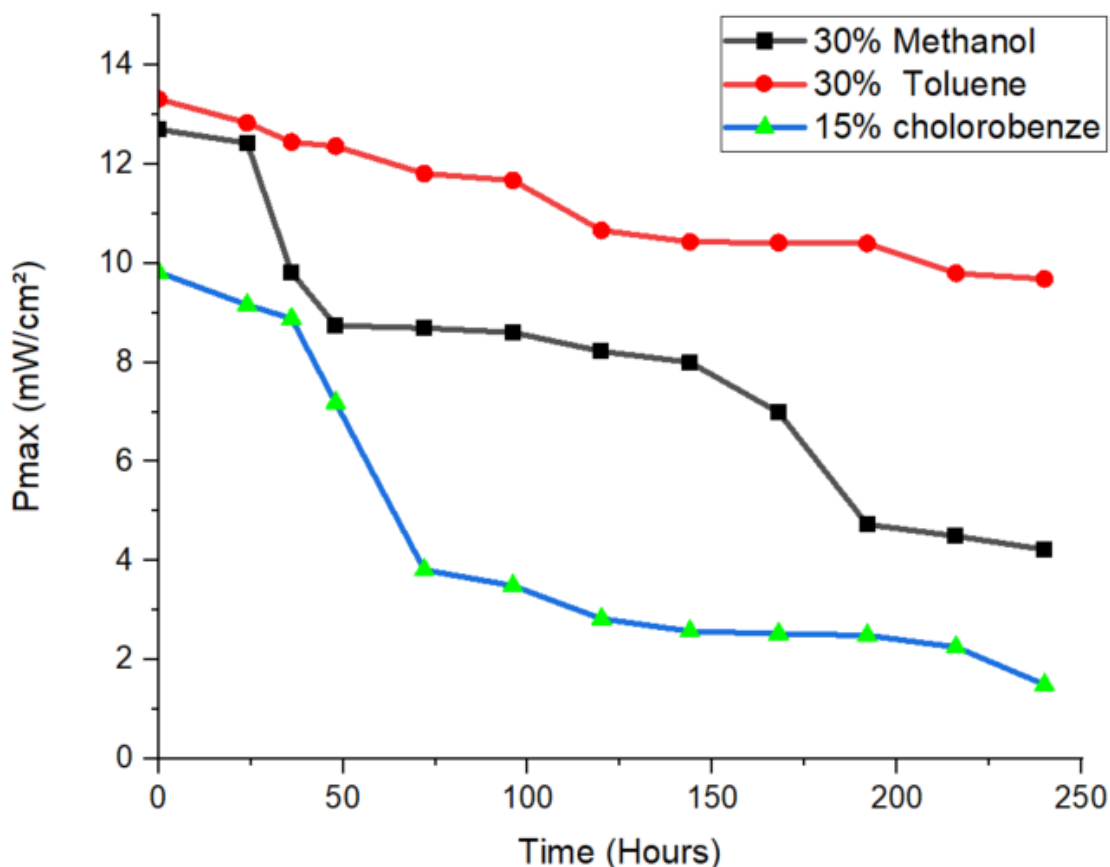


Figure 5-13 The maximum power outputs as a function of operating period for the best-performing devices treated by three different mixed antisolvents.

5.6 Summary

This chapter explore the effectiveness of the mixed antisolvents in fabricating perovskite solar cells in high humidity environment. Three combinations were selected to address the challenges of high humidity fabrication, which include “ethyl acetate and methanol,” “methyl acetate and toluene,” and “methyl formate and chlorobenzene.” Systematic experimental investigations were conducted to determine the most effective mixture and to demonstrate their effectiveness and benefits. The results show that the combined use of two antisolvents can improved fabrication quality of perovskite solar cells if appropriate combination is identified. In particular, a mixed antisolvent of ethyl acetate (70%) and methanol (30%) can improve the power output from 9.42 mW/cm² to 12.70 mW/cm² for fabrication in high humidity environment of 70% - 75% RH. Similarly, the power output can be increased from 9.70 mW/cm² to 13.31 mW/cm² or from 7.19 mW/cm² to 9.82 mW/cm² if mixed antisolvents of methyl acetate (70%) and toluene (30%) or methyl formate (85%) and chlorobenzene (15%) are employed.

The experimental outcomes also provide strong evidence to support the strategy of using the mixed antisolvent to meet the multiple requirements that a single antisolvent cannot. The improvement obtained from the combination ethyl acetate and methanol is likely due to improved water solubility in the mixture as a result of adding methanol that has very high water solubility. While the improvements obtained from the combinations of methyl acetate and toluene or methyl formate and chlorobenzene are likely due to a reduced dipole moment in the mixtures as a result of adding toluene or chlorobenzene, both of which have smaller dipole moments. Furthermore, this work also demonstrates that the different antisolvents may bring the similar improvement in the performance but very different impact on the stability of the devices. The devices treated using the mixed antisolvent of methyl acetate (70%) and toluene (30%) has much better stability than these treated using other two mixed antisolvents investigated in this study.

Chapter 6: Conclusion

6.1 Conclusion

The quest for clean and sustainable energy sources is paramount in addressing global climate challenges. Perovskite solar cells (PSCs) have emerged as a frontrunner in this pursuit, captivating researchers with their remarkable potential for high efficiencies and cost-effective production. This thesis has delved into this exciting realm with a goal to develop air fabrication procedures of PSCs, particularly in high humidity ambient air of >70%, paving the way for a more convenient and economic approach for production. The main outcomes of this research project are summarised as follows.

An preliminary investigation was performed to determine the methodologies, fabrication procedures and device structures that are suitable for the research purposes of this project. Exploratory experiments were conducted to identify the challenging issues related to fabrication in ambient air, particularly under high humidity environments. An correlation between the humidity of fabrication and the performance of the devices was identified, which show that using fabrication procedures available at the start of this project, the fabricated devices exhibited better performance when fabricated under the humidity between 35% and 55%. The performance was significantly poor for the devices fabrication in ambient air with humidity of >70%.

Systematic investigations were conducted to determine the key optimal processing parameters to enable reliable preparation of the MAPbI₃ layers and fabrication of perovskite solar cells in ambient air. It was found that the most suitable parameters for in-air fabrication are a spin-coating speed of 4000 rpm and annealing temperature of 90 °C with antisolvent treatment using methyl acetate. This work established benchmark processing procedures and paved a groundwork for preparation of the MAPbI₃ layers and perovskite solar cells for further studies in this aspect.

An experimental study was performed to improve the quality of the MAPbI₃ layers and the performance of perovskite solar cells fabricated under high humidity (>70%)

environment. This is achieved by following a strategy of using mixed antisolvents. A new mixed antisolvent, which consists of ethyl acetate and methanol, were designed based on the principle of increasing the water solubility of ethyl acetate by adding methanol that has high water solubility. A systematic experiment were conducted to determine the optimal ratio of the mixture. The results of this study demonstrate that the devices treated using the mixed antisolvent resulted in an improved performance compared to the devices treated using a single antisolvent (i.e., pure ethyl acetate). The optimal ratio of the mixture is 70% of ethyl acetate and 30% of methanol. This outcome offers new mixed antisolvent to the fields of perovskite solar cell research, particularly useful for fabrication in high humidity environment.

A further study was carried out following the strategy of mixed antisolvent based on the idea of reducing the dipole moment in methyl acetate or methyl formate. Two sets of new mixed antisolvent were designed. One consists of methyl acetate and toluene, and the other consists of methyl formate and chlorobenzene. Systematic investigations were performed and the results demonstrate the improved performance of the devices treated using these mixed antisolvents compared to the devices treated with respective single antisolvents. It is found that the optimal ratio is 70% of methyl acetate and 30% of toluene, and 85% of methyl formate and 15% of chlorobenzene, respectively. The outcomes from this study provide further two sets of new antisolvents for in-air fabrication of perovskite solar cells under high humidity environment.

The effect of these new mixed antisolvents on the stability of the fabricated perovskite solar cells were investigated. The results show that the devices treated using two different antisolvents may lead to similar performance but they can lead to significant different degradation rate. Therefore, selecting suitable antisolvent requires considering its effect on both the performance and stability.

6.2 Future work

The following recommendations outline areas for further research based on the findings of this study:

- Refine processing parameters by conducting systematic studies to optimize in-air fabrication conditions for electron and hole transport layers, as well as Ag electrode deposition. These layers, though not the focus of this study, are crucial for maximizing the benefits of improved MAPbI₃ film quality.
- Investigate mixed antisolvent ratios on a finer scale (e.g., 1% increments) to accurately determine the optimal ratio for each combination tested.
- Explore new antisolvent combinations, including combinations of three or more antisolvents, to study their effects on the performance and stability of perovskite devices.
- Conduct detailed studies to understand why different antisolvents yield similar performance enhancements but have significantly different impacts on device stability.
- Apply the mixed antisolvents developed in this study to other humidity-sensitive perovskite solar cells or optoelectronic devices to evaluate their broader effectiveness and suitability.
- Perform extensive stability assessments of devices under diverse environmental conditions to ensure real-world applicability and durability.
- These directions will provide deeper insights, enable technological advancements, and guide the development of more efficient and stable perovskite-based devices

References

- [1] I. E. A. (IEA), “World Energy Outlook 2022 (WEO),” <https://www.iea.org/>.
- [2] Q. A. Akkerman, G. Rainò, M. V Kovalenko, and L. Manna, “Genesis, challenges and opportunities for colloidal lead halide perovskite nanocrystals,” *Nat Mater*, vol. 17, no. 5, pp. 394–405, 2018.
- [3] S. A. Veldhuis *et al.*, “Perovskite materials for light-emitting diodes and lasers,” *Advanced materials*, vol. 28, no. 32, pp. 6804–6834, 2016.
- [4] C.-H. A. Li, Z. Zhou, P. Vashishtha, and J. E. Halpert, “The future is blue (LEDs): why chemistry is the key to perovskite displays §,” *Chemistry of Materials*, vol. 31, no. 16, pp. 6003–6032, 2019.
- [5] O. Pfingsten, J. Klein, L. Protesescu, M. I. Bodnarchuk, M. V Kovalenko, and G. Bacher, “Phonon interaction and phase transition in single formamidinium lead bromide quantum dots,” *Nano Lett*, vol. 18, no. 7, pp. 4440–4446, 2018.
- [6] D. Baranov *et al.*, “Aging of self-assembled lead halide perovskite nanocrystal superlattices: effects on photoluminescence and energy transfer,” *ACS Nano*, vol. 15, no. 1, pp. 650–664, 2020.
- [7] Q. Cheng *et al.*, “High-Efficiency and Stable Perovskite Solar Cells Enabled by Low-Dimensional Perovskite Surface Modifiers,” *Solar rrl*, vol. 6, no. 8, p. 2100805, 2022.
- [8] J. Kim, S. Kim, C. Zuo, M. Gao, D. Vak, and D. Kim, “Humidity-tolerant roll-to-roll fabrication of perovskite solar cells via polymer-additive-assisted hot slot die deposition,” *Adv Funct Mater*, vol. 29, no. 26, p. 1809194, 2019.
- [9] A. Demirbas, “Recent advances in biomass conversion technologies,” *Energy Edu. Sci. Technol*, vol. 6, pp. 19–40, 2000.
- [10] N. S. Rathore and N. L. Panwar, *Renewable energy sources for sustainable development*. New India Publishing, 2007.

References

- [11] R. A. Zakhidov, "Central Asian countries energy system and role of renewable energy sources," *Applied Solar Energy*, vol. 44, pp. 218–223, 2008.
- [12] A. Bergmann, S. Colombo, and N. Hanley, "Rural versus urban preferences for renewable energy developments," *Ecological economics*, vol. 65, no. 3, pp. 616–625, 2008.
- [13] N. H. Ravindranath and D. O. Hall, *Biomass, energy and environment: a developing country perspective from India*. Oxford University Press, 1995.
- [14] S. Agrawal and R. Soni, "Renewable Energy: Sources, Importance and Prospects for Sustainable Future," *Energy: Crises, Challenges and Solutions*, pp. 131–150, 2021.
- [15] A. F. Sherwani and J. A. Usmani, "Life cycle assessment of solar PV based electricity generation systems: A review," *Renewable and Sustainable Energy Reviews*, vol. 14, no. 1, pp. 540–544, 2010.
- [16] O. I. Okoro and T. C. Madueme, "Solar energy: a necessary investment in a developing economy," *International Journal of Sustainable Energy*, vol. 25, no. 01, pp. 23–31, 2006.
- [17] A. Paulillo, A. Striolo, and P. Lettieri, "The environmental impacts and the carbon intensity of geothermal energy: A case study on the Hellisheiði plant," *Environ Int*, vol. 133, p. 105226, 2019.
- [18] A. Dhar, M. A. Naeth, P. D. Jennings, and M. Gamal El-Din, "Geothermal energy resources: Potential environmental impact and land reclamation," *Environmental Reviews*, vol. 28, no. 4, pp. 415–427, 2020.
- [19] A. Dhar, M. A. Naeth, P. D. Jennings, and M. Gamal El-Din, "Geothermal energy resources: Potential environmental impact and land reclamation," *Environmental Reviews*, vol. 28, no. 4, pp. 415–427, 2020.
- [20] M. Berglund and P. Börjesson, "Assessment of energy performance in the life-cycle of biogas production," *Biomass Bioenergy*, vol. 30, no. 3, pp. 254–266, 2006.

References

- [21] J. B. Holm-Nielsen, T. Al Seadi, and P. Oleskowicz-Popiel, "The future of anaerobic digestion and biogas utilization," *Bioresour Technol*, vol. 100, no. 22, pp. 5478–5484, 2009.
- [22] M. Balat, "A review of modern wind turbine technology," *Energy Sources, Part A*, vol. 31, no. 17, pp. 1561–1572, 2009.
- [23] H. Huang and Z. Yan, "Present situation and future prospect of hydropower in China," *Renewable and Sustainable Energy Reviews*, vol. 13, no. 6–7, pp. 1652–1656, 2009.
- [24] J. Liu, J. Zuo, Z. Sun, G. Zillante, and X. Chen, "Sustainability in hydropower development—A case study," *Renewable and Sustainable Energy Reviews*, vol. 19, pp. 230–237, 2013.
- [25] M. Afzaal and P. O'Brien, "Recent developments in II–VI and III–VI semiconductors and their applications in solar cells," *J Mater Chem*, vol. 16, no. 17, pp. 1597–1602, 2006.
- [26] B. Munkhbayar, M. J. Nine, J. Jeoun, M. Ji, H. Jeong, and H. Chung, "Synthesis of a graphene–tungsten composite with improved dispersibility of graphene in an ethanol solution and its use as a counter electrode for dye-sensitized solar cells," *J Power Sources*, vol. 230, pp. 207–217, 2013.
- [27] W. Luo *et al.*, "A comparative life-cycle assessment of photovoltaic electricity generation in Singapore by multicrystalline silicon technologies," *Solar Energy Materials and Solar Cells*, vol. 174, pp. 157–162, 2018.
- [28] R. R. King *et al.*, "40% efficient metamorphic GaInP/ GaInAs/ Ge multijunction solar cells," *Appl Phys Lett*, vol. 90, no. 18, p. 183516, 2007.
- [29] R. R. King *et al.*, "40% efficient metamorphic GaInP/ GaInAs/ Ge multijunction solar cells," *Appl Phys Lett*, vol. 90, no. 18, p. 183516, 2007.
- [30] W.-Y. Rho, H.-Y. Yang, H.-S. Kim, B. S. Son, J. S. Suh, and B.-H. Jun, "Recent advances in plasmonic dye-sensitized solar cells," *J Solid State Chem*, vol. 258, pp. 271–282, 2018.

References

- [31] H. Sai *et al.*, “Triple-junction thin-film silicon solar cell fabricated on periodically textured substrate with a stabilized efficiency of 13.6%,” *Appl Phys Lett*, vol. 106, no. 21, p. 213902, 2015.
- [32] A. Bartolotta and G. Calogero, “Dye-sensitized solar cells: From synthetic dyes to natural pigments,” in *Solar Cells and Light Management*, Elsevier, 2020, pp. 107–161.
- [33] T. D. Lee and A. U. Ebong, “A review of thin film solar cell technologies and challenges,” *Renewable and Sustainable Energy Reviews*, vol. 70, pp. 1286–1297, 2017.
- [34] H. K. H. Lee, J. Barbé, and W. C. Tsoi, “Organic and perovskite photovoltaics for indoor applications,” in *Solar Cells and Light Management*, Elsevier, 2020, pp. 355–388.
- [35] K. J. Stevenson and S. Luchkin, “Photochemically-Induced Phase Segregation of Mixed Halide Perovskite Solar Cells,” in *Electrochemical Society Meeting Abstracts 239*, The Electrochemical Society, Inc., 2021, p. 1809.
- [36] NREL energy center, “NREL Photovoltaic cell efficiency .”
- [37] P. Harper, “The end in sight?: Some speculations on environmental trends in the twenty-first century,” *Futures*, vol. 32, no. 3–4, pp. 361–384, 2000.
- [38] ASTM, “American Society for Testing and Materials (ASTM),” ASTM.
- [39] C. A. Gueymard, “Reference solar spectra: Their evolution, standardization issues, and comparison to recent measurements,” *Advances in Space Research*, vol. 37, no. 2, pp. 323–340, 2006.
- [40] S. Rühle, “Tabulated values of the Shockley–Queisser limit for single junction solar cells,” *Solar energy*, vol. 130, pp. 139–147, 2016.
- [41] K. Ranabhat, L. Patrikeev, A. Antal’evna-Revina, K. Andrianov, V. Lapshinsky, and E. Sofronova, “An introduction to solar cell technology,” *Journal of Applied Engineering Science*, vol. 14, no. 4, pp. 481–491, 2016.
- [42] K. Ryu *et al.*, “High-efficiency n-type Si solar cells with novel inkjet-printed boron emitters,” *IEEE electron device letters*, vol. 33, no. 6, pp. 854–856, 2012.

References

- [43] A. Cuevas, M. J. Kerr, C. Samundsett, F. Ferrazza, and G. Coletti, "Millisecond minority carrier lifetimes in n-type multicrystalline silicon," *Appl Phys Lett*, vol. 81, no. 26, pp. 4952–4954, 2002.
- [44] A. S. Al-Ezzi and M. N. M. Ansari, "Photovoltaic solar cells: a review," *Applied System Innovation*, vol. 5, no. 4, p. 67, 2022.
- [45] M. H. Imtiaz and G. Hashmi, "Towards High Efficiency Solar Cells: Composite Metamaterials," *Global Journals of Research in Engineering*, vol. 13, no. F10, pp. 11–16, 2013.
- [46] Q. Su, G. Zhang, J. Lai, S. Feng, and W. Shi, "Green Solar Electric Vehicle Changing the Future Lifestyle of Human."
- [47] M. Wolf and H. Rauschenbach, "RESISTANCE EFFECTS ON SOLAR CELL MEASUREMENTS *," Pergamon Press, 1963.
- [48] N. Wu *et al.*, "Identifying the cause of voltage and fill factor losses in perovskite solar cells by using luminescence measurements," *Energy Technology*, vol. 5, no. 10, pp. 1827–1835, 2017.
- [49] A. S. Subbiah, A. Halder, S. Ghosh, N. Mahuli, G. Hodes, and S. K. Sarkar, "Inorganic hole conducting layers for perovskite-based solar cells," *J Phys Chem Lett*, vol. 5, no. 10, pp. 1748–1753, 2014.
- [50] J. Zhang, S.-T. Lee, and B. Sun, "Effect of series and shunt resistance on organic-inorganic hybrid solar cells performance," *Electrochim Acta*, vol. 146, pp. 845–849, 2014.
- [51] N. Wu *et al.*, "Identifying the cause of voltage and fill factor losses in perovskite solar cells by using luminescence measurements," *Energy Technology*, vol. 5, no. 10, pp. 1827–1835, 2017.
- [52] V. M. Le Corre *et al.*, "Revealing charge carrier mobility and defect densities in metal halide perovskites via space-charge-limited current measurements," *ACS Energy Lett*, vol. 6, no. 3, pp. 1087–1094, 2021.

References

- [53] A. L. Fahrenbruch, R. H. Bube, and R. V D'Aiello, "Fundamentals of solar cells (photovoltaic solar energy conversion)," 1984.
- [54] J. Yao *et al.*, "Quantifying losses in open-circuit voltage in solution-processable solar cells," *Phys Rev Appl*, vol. 4, no. 1, p. 014020, 2015.
- [55] Y. Da, Y. Xuan, and Q. Li, "Quantifying energy losses in planar perovskite solar cells," *Solar Energy Materials and Solar Cells*, vol. 174, pp. 206–213, 2018.
- [56] J. A. Nelson, *The physics of solar cells*. World Scientific Publishing Company, 2003.
- [57] D. M. Fébba, R. M. Rubinger, A. F. Oliveira, and E. C. Bortoni, "Impacts of temperature and irradiance on polycrystalline silicon solar cells parameters," *Solar Energy*, vol. 174, pp. 628–639, 2018.
- [58] C. Xiao, X. Yu, D. Yang, and D. Que, "Impact of solar irradiance intensity and temperature on the performance of compensated crystalline silicon solar cells," *Solar Energy Materials and Solar Cells*, vol. 128, pp. 427–434, 2014.
- [59] seaward, "How does temperature and irradiance affect I-V curves_ - Seaward Support," [https://www.seaward.com/gb/enquiry/.](https://www.seaward.com/gb/enquiry/), May 2023, Accessed: May 06, 2023. [Online]. Available: [https://www.seaward.com/gb/enquiry/.](https://www.seaward.com/gb/enquiry/)
- [60] U. Mouloud *et al.*, "Temperature effect on the organic solar cells parameters Djedjiga Hatem Effect of Temperature on the Organic Solar Cells Parameters," 2012. [Online]. Available: <https://www.researchgate.net/publication/292884301>
- [61] M. A. Green, E. D. Dunlop, J. Hohl-Ebinger, M. Yoshita, N. Kopidakis, and X. Hao, "Solar cell efficiency tables (Version 58)," *Progress in Photovoltaics: Research and applications*, vol. 29, no. 7, pp. 657–667, 2021.
- [62] J. C. Ogbulezie, A. O. Njok, M. K. Panjwani, and S. K. Panjwani, "The impact of high temperature and irradiance source on the efficiency of polycrystalline photovoltaic panel in a controlled environment," *International Journal of Electrical and Computer Engineering*, vol. 10, no. 4, p. 3942, 2020.
- [63] J. Liang *et al.*, "Temperature-Dependent Open-Circuit Voltage Measurements and Temperature-Dependent Open-Circuit Voltage Measurements and Light-Soaking in

- Hydrogenated Amorphous Silicon Solar Cells Light-Soaking in Hydrogenated Amorphous Silicon Solar Cells "Temperature-dependent Open-circuit Voltage Measurements and Light-soaking in Hydrogenated Amorphous Silicon Solar Cells Temperature-Dependent Open-Circuit Voltage Measurements and Light-Soaking in Hydrogenated Amorphous Silicon Solar Cells," 2005. [Online]. Available: <https://surface.syr.edu/phy>
- [64] T. Tobe, N. Shibayama, Y. Nakamura, M. Ikegami, H. Kanda, and T. Miyasaka, "Investigation of the Temperature Coefficients of Perovskite Solar Cells for Application in High-Temperature Environments," *Chem Asian J*, Jul. 2024, doi: 10.1002/asia.202400686.
- [65] A. Kojima, K. Teshima, Y. Shirai, and T. Miyasaka, "Organometal halide perovskites as visible-light sensitizers for photovoltaic cells," *J Am Chem Soc*, vol. 131, no. 17, pp. 6050–6051, 2009.
- [66] H.-S. Kim *et al.*, "Lead iodide perovskite sensitized all-solid-state submicron thin film mesoscopic solar cell with efficiency exceeding 9%," *Sci Rep*, vol. 2, no. 1, p. 591, 2012.
- [67] NREL, "NREL Best Research-Cell Efficiency Chart," *Best Research-Cell Efficiency Chart*, 2023.
- [68] M. A. Green, A. Ho-Baillie, and H. J. Snaith, "The emergence of perovskite solar cells," *Nat Photonics*, vol. 8, no. 7, pp. 506–514, 2014.
- [69] J. Berry *et al.*, "Hybrid organic–inorganic perovskites (HOIPs): Opportunities and challenges," *Advanced Materials*, vol. 27, no. 35, pp. 5102–5112, 2015.
- [70] B. Chen, X. Zheng, Y. Bai, N. P. Padture, and J. Huang, "Progress in tandem solar cells based on hybrid organic–inorganic perovskites," *Adv Energy Mater*, vol. 7, no. 14, p. 1602400, 2017.
- [71] P. K. Nayak and D. Cahen, "Updated assessment of possibilities and limits for solar cells," *Advanced Materials*, vol. 26, no. 10, pp. 1622–1628, 2014.

References

- [72] S. Yang, W. Fu, Z. Zhang, H. Chen, and C.-Z. Li, "Recent advances in perovskite solar cells: efficiency, stability and lead-free perovskite," *J Mater Chem A Mater*, vol. 5, no. 23, pp. 11462–11482, 2017.
- [73] M. Younas, T. A. Kandiel, A. Rinaldi, Q. Peng, and A. A. Al-Saadi, "Ambient-environment processed perovskite solar cells: A review," Nov. 01, 2021, *Elsevier Ltd*. doi: 10.1016/j.mtphys.2021.100557.
- [74] S. S. Mali and C. K. Hong, "pin/nip type planar hybrid structure of highly efficient perovskite solar cells towards improved air stability: synthetic strategies and the role of p-type hole transport layer (HTL) and n-type electron transport layer (ETL) metal oxides," *Nanoscale*, vol. 8, no. 20, pp. 10528–10540, 2016.
- [75] H. Zhang and N.-G. Park, "Progress and issues in pin type perovskite solar cells," *DeCarbon*, p. 100025, 2023.
- [76] J. Chen and Y. Wang, "Personalized dynamic transport of magnetic nanorobots inside the brain vasculature," *Nanotechnology*, vol. 31, no. 49, p. 495706, 2020.
- [77] M. Saliba *et al.*, "Cesium-containing triple cation perovskite solar cells: improved stability, reproducibility and high efficiency," *Energy Environ Sci*, vol. 9, no. 6, pp. 1989–1997, 2016.
- [78] H. Min *et al.*, "Perovskite solar cells with atomically coherent interlayers on SnO₂ electrodes," *Nature*, vol. 598, no. 7881, pp. 444–450, 2021.
- [79] N. J. Jeon *et al.*, "A fluorene-terminated hole-transporting material for highly efficient and stable perovskite solar cells," *Nat Energy*, vol. 3, no. 8, pp. 682–689, 2018.
- [80] W. E. I. Sha, X. Ren, L. Chen, and W. C. H. Choy, "The efficiency limit of CH₃NH₃PbI₃ perovskite solar cells," *Appl Phys Lett*, vol. 106, no. 22, p. 221104, 2015.
- [81] J. J. Yoo *et al.*, "Efficient perovskite solar cells via improved carrier management," *Nature*, vol. 590, no. 7847, pp. 587–593, 2021.
- [82] M. M. Lee, J. Teuscher, T. Miyasaka, T. N. Murakami, and H. J. Snaith, "Efficient hybrid solar cells based on meso-superstructured organometal halide perovskites," *Science (1979)*, vol. 338, no. 6107, pp. 643–647, 2012.

References

- [83] M. Jeong *et al.*, "Stable perovskite solar cells with efficiency exceeding 24.8% and 0.3-V voltage loss," *Science (1979)*, vol. 369, no. 6511, pp. 1615–1620, 2020.
- [84] J. Príncipe, V. C. M. Duarte, and L. Andrade, "Inverted Perovskite Solar Cells: The Emergence of a Highly Stable and Efficient Architecture," Apr. 01, 2022, *John Wiley and Sons Inc.* doi: 10.1002/ente.202100952.
- [85] S. Sun *et al.*, "The origin of high efficiency in low-temperature solution-processable bilayer organometal halide hybrid solar cells," *Energy Environ Sci*, vol. 7, no. 1, pp. 399–407, 2014.
- [86] T. Baikie *et al.*, "Synthesis and crystal chemistry of the hybrid perovskite (CH₃NH₃)PbI₃ for solid-state sensitised solar cell applications," *J Mater Chem A Mater*, vol. 1, no. 18, pp. 5628–5641, 2013.
- [87] A. Facchetti, "Polymer donor–polymer acceptor (all-polymer) solar cells," *Materials Today*, vol. 16, no. 4, pp. 123–132, 2013.
- [88] M. A. Green, A. Ho-Baillie, and H. J. Snaith, "The emergence of perovskite solar cells," *Nat Photonics*, vol. 8, no. 7, pp. 506–514, 2014.
- [89] S. P. Singh and P. Nagarjuna, "Organometal halide perovskites as useful materials in sensitized solar cells," *Dalton Transactions*, vol. 43, no. 14, pp. 5247–5251, 2014.
- [90] A. Marchioro *et al.*, "Unravelling the mechanism of photoinduced charge transfer processes in lead iodide perovskite solar cells," *Nat Photonics*, vol. 8, no. 3, pp. 250–255, 2014.
- [91] D. Zhou, T. Zhou, Y. Tian, X. Zhu, and Y. Tu, "Perovskite-based solar cells: materials, methods, and future perspectives," *J Nanomater*, vol. 2018, no. 1, p. 8148072, 2018.
- [92] H.-S. Kim *et al.*, "Lead iodide perovskite sensitized all-solid-state submicron thin film mesoscopic solar cell with efficiency exceeding 9%," *Sci Rep*, vol. 2, no. 1, p. 591, 2012.
- [93] S. D. Stranks *et al.*, "Electron-hole diffusion lengths exceeding 1 micrometer in an organometal trihalide perovskite absorber," *Science (1979)*, vol. 342, no. 6156, pp. 341–344, 2013.

References

- [94] N.-G. Park, "Perovskite solar cells: an emerging photovoltaic technology," *Materials today*, vol. 18, no. 2, pp. 65–72, 2015.
- [95] C. Wehrenfennig, G. E. Eperon, M. B. Johnston, H. J. Snaith, and L. M. Herz, "High charge carrier mobilities and lifetimes in organolead trihalide perovskites," *Advanced materials*, vol. 26, no. 10, pp. 1584–1589, 2014.
- [96] X. Liu, W. Zhao, H. Cui, Y. Wang, T. Xu, and F. Huang, "Organic–inorganic halide perovskite based solar cells—revolutionary progress in photovoltaics," *Inorg Chem Front*, vol. 2, no. 4, pp. 315–335, 2015.
- [97] S. Wozny *et al.*, "Controlled humidity study on the formation of higher efficiency formamidinium lead triiodide-based solar cells," *Chemistry of Materials*, vol. 27, no. 13, pp. 4814–4820, 2015.
- [98] I. Mesquita, L. Andrade, and A. Mendes, "Effect of relative humidity during the preparation of perovskite solar cells: Performance and stability," *Solar Energy*, vol. 199, pp. 474–483, 2020.
- [99] I. Mesquita, L. Andrade, and A. Mendes, "Effect of relative humidity during the preparation of perovskite solar cells: Performance and stability," *Solar Energy*, vol. 199, pp. 474–483, Mar. 2020, doi: 10.1016/j.solener.2020.02.052.
- [100] P. P. Boix, K. Nonomura, N. Mathews, and S. G. Mhaisalkar, "Current progress and future perspectives for organic/inorganic perovskite solar cells," *Materials today*, vol. 17, no. 1, pp. 16–23, 2014.
- [101] S. Ryu *et al.*, "Voltage output of efficient perovskite solar cells with high open-circuit voltage and fill factor," *Energy Environ Sci*, vol. 7, no. 8, pp. 2614–2618, 2014.
- [102] W. S. Yang *et al.*, "High-performance photovoltaic perovskite layers fabricated through intramolecular exchange," *Science (1979)*, vol. 348, no. 6240, pp. 1234–1237, 2015.
- [103] T. Singh and T. Miyasaka, "Stabilizing the efficiency beyond 20% with a mixed cation perovskite solar cell fabricated in ambient air under controlled humidity," *Adv Energy Mater*, vol. 8, no. 3, p. 1700677, 2018.

References

- [104] W. S. Yang *et al.*, "Iodide management in formamidinium-lead-halide-based perovskite layers for efficient solar cells," *Science (1979)*, vol. 356, no. 6345, pp. 1376–1379, 2017.
- [105] Q. Jiang *et al.*, "Surface passivation of perovskite film for efficient solar cells," *Nat Photonics*, vol. 13, no. 7, pp. 460–466, 2019.
- [106] H. Sarvari *et al.*, "Photovoltaic Performance of Lead-Iodide Perovskite Solar Cells Fabricated Under Ambient Air Conditions With HTM Solution Excluding LiTFSI," *IEEE J Photovolt*, vol. 8, no. 4, pp. 1051–1057, 2018.
- [107] A. Kojima, K. Teshima, Y. Shirai, and T. Miyasaka, "Organometal halide perovskites as visible-light sensitizers for photovoltaic cells," *J Am Chem Soc*, vol. 131, no. 17, pp. 6050–6051, 2009.
- [108] H.-S. Kim *et al.*, "Lead iodide perovskite sensitized all-solid-state submicron thin film mesoscopic solar cell with efficiency exceeding 9%," *Sci Rep*, vol. 2, no. 1, p. 591, 2012.
- [109] W. Hui *et al.*, "Stabilizing black-phase formamidinium perovskite formation at room temperature and high humidity," *Science (1979)*, vol. 371, no. 6536, pp. 1359–1364, 2021.
- [110] J. Lee *et al.*, "Achieving large-area planar perovskite solar cells by introducing an interfacial compatibilizer," *Advanced materials*, vol. 29, no. 22, p. 1606363, 2017.
- [111] Z. Song *et al.*, "A technoeconomic analysis of perovskite solar module manufacturing with low-cost materials and techniques," *Energy Environ Sci*, vol. 10, no. 6, pp. 1297–1305, 2017.
- [112] Y. Cheng *et al.*, "The detrimental effect of excess mobile ions in planar CH₃NH₃PbI₃ perovskite solar cells," *J Mater Chem A Mater*, vol. 4, no. 33, pp. 12748–12755, 2016.
- [113] K. Vandewal *et al.*, "Quantification of Quantum efficiency and energy losses in low bandgap polymer: fullerene solar cells with high open-circuit voltage," *Adv Funct Mater*, vol. 22, no. 16, pp. 3480–3490, 2012.

References

- [114] M. Tingem and M. Rivington, "Adaptation for crop agriculture to climate change in Cameroon: turning on the heat," *Mitig Adapt Strateg Glob Chang*, vol. 14, pp. 153–168, 2009.
- [115] J.-H. Im, C.-R. Lee, J.-W. Lee, S.-W. Park, and N.-G. Park, "6.5% efficient perovskite quantum-dot-sensitized solar cell," *Nanoscale*, vol. 3, no. 10, pp. 4088–4093, 2011.
- [116] M. M. Lee, J. Teuscher, T. Miyasaka, T. N. Murakami, and H. J. Snaith, "Efficient hybrid solar cells based on meso-superstructured organometal halide perovskites," *Science (1979)*, vol. 338, no. 6107, pp. 643–647, 2012.
- [117] J. M. Ball, M. M. Lee, A. Hey, and H. J. Snaith, "Low-temperature processed meso-superstructured to thin-film perovskite solar cells," *Energy Environ Sci*, vol. 6, no. 6, pp. 1739–1743, 2013.
- [118] D. Liu and T. L. Kelly, "Perovskite solar cells with a planar heterojunction structure prepared using room-temperature solution processing techniques," *Nat Photonics*, vol. 8, no. 2, pp. 133–138, 2014.
- [119] J. Lee, D. Seol, A. Cho, and N. Park, "High-efficiency perovskite solar cells based on the black polymorph of HC (NH₂)₂PbI₃," *Advanced Materials*, vol. 26, no. 29, pp. 4991–4998, 2014.
- [120] H. Zhou *et al.*, "Interface engineering of highly efficient perovskite solar cells," *Science (1979)*, vol. 345, no. 6196, pp. 542–546, 2014.
- [121] W. S. Yang *et al.*, "High-performance photovoltaic perovskite layers fabricated through intramolecular exchange," *Science (1979)*, vol. 348, no. 6240, pp. 1234–1237, 2015.
- [122] M. Saliba *et al.*, "Incorporation of rubidium cations into perovskite solar cells improves photovoltaic performance," *Science (1979)*, vol. 354, no. 6309, pp. 206–209, 2016.
- [123] W. S. Yang *et al.*, "Iodide management in formamidinium-lead-halide-based perovskite layers for efficient solar cells," *Science (1979)*, vol. 356, no. 6345, pp. 1376–1379, 2017.

References

- [124] E. H. Jung *et al.*, “Efficient, stable and scalable perovskite solar cells using poly (3-hexylthiophene),” *Nature*, vol. 567, no. 7749, pp. 511–515, 2019.
- [125] J. J. Yoo *et al.*, “Efficient perovskite solar cells via improved carrier management,” *Nature*, vol. 590, no. 7847, pp. 587–593, 2021.
- [126] P. Lin *et al.*, “Pseudo-halide perovskite solar cells,” *Adv Energy Mater*, vol. 11, no. 28, p. 2100818, 2021.
- [127] O. Ourahmoun, “Performance and Life-Time Stability of Perovskite Solar Cells,” *International Journal of Materials*, vol. 7, pp. 86–89, Dec. 2020, doi: 10.46300/91018.2020.7.15.
- [128] J. Idígoras *et al.*, “Enhancing moisture and water resistance in perovskite solar cells by encapsulation with ultrathin plasma polymers,” *ACS Appl Mater Interfaces*, vol. 10, no. 14, pp. 11587–11594, 2018.
- [129] Y. Du *et al.*, “Spacer engineering of thiophene-based two-dimensional/three-dimensional hybrid perovskites for stable and efficient solar cells,” *The Journal of Physical Chemistry C*, vol. 126, no. 7, pp. 3351–3358, 2022.
- [130] H. Kanda *et al.*, “Light Stability Enhancement of Perovskite Solar Cells Using 1H, 1H, 2H, 2H-Perfluorooctyltriethoxysilane Passivation,” *Solar Rrl*, vol. 5, no. 3, p. 2000650, 2021.
- [131] “A mini review of recent strategies towards stable nano-structure perovskite solar cell fabrication,” *International Journal For Innovative Engineering and Management Research*, pp. 430–436, Dec. 2020, doi: 10.48047/ijiemr/v09/i12/82.
- [132] J. M. Frost, K. T. Butler, F. Brivio, C. H. Hendon, M. Van Schilfgaarde, and A. Walsh, “Atomistic origins of high-performance in hybrid halide perovskite solar cells,” *Nano Lett*, vol. 14, no. 5, pp. 2584–2590, 2014.
- [133] B. Li, Y. Li, C. Zheng, D. Gao, and W. Huang, “Advancements in the stability of perovskite solar cells: degradation mechanisms and improvement approaches,” *RSC Adv*, vol. 6, no. 44, pp. 38079–38091, 2016.

References

- [134] Q. Meng *et al.*, “Effect of temperature on the performance of perovskite solar cells,” *Journal of Materials Science: Materials in Electronics*, vol. 32, pp. 12784–12792, 2021.
- [135] M. Adil Afroz *et al.*, “Thermal stability and performance enhancement of perovskite solar cells through oxalic acid-induced perovskite formation,” *ACS Appl Energy Mater*, vol. 3, no. 3, pp. 2432–2439, 2020.
- [136] G. Niu, X. Guo, and L. Wang, “Review of recent progress in chemical stability of perovskite solar cells,” *J Mater Chem A Mater*, vol. 3, no. 17, pp. 8970–8980, 2015.
- [137] D. Kim, D.-K. Lee, S. M. Kim, W. Park, and U. Sim, “Photoelectrochemical water splitting reaction system based on metal-organic halide perovskites,” *Materials*, vol. 13, no. 1, p. 210, 2020.
- [138] J. M. Frost, K. T. Butler, F. Brivio, C. H. Hendon, M. Van Schilfgaarde, and A. Walsh, “Atomistic origins of high-performance in hybrid halide perovskite solar cells,” *Nano Lett*, vol. 14, no. 5, pp. 2584–2590, 2014.
- [139] J. Yang, B. D. Siempelkamp, D. Liu, and T. L. Kelly, “Investigation of CH₃NH₃PbI₃ degradation rates and mechanisms in controlled humidity environments using in situ techniques,” *ACS Nano*, vol. 9, no. 2, pp. 1955–1963, 2015.
- [140] E. Akman, A. E. Shalan, F. Sadegh, and S. Akin, “Moisture-resistant FAPbI₃ perovskite solar cell with 22.25% power conversion efficiency through pentafluorobenzyl phosphonic acid passivation,” *ChemSusChem*, vol. 14, no. 4, pp. 1176–1183, 2021.
- [141] T. A. Berhe *et al.*, “Organometal halide perovskite solar cells: degradation and stability,” *Energy Environ Sci*, vol. 9, no. 2, pp. 323–356, 2016.
- [142] Z. Qian *et al.*, “Manipulating SnO₂ growth for efficient electron transport in perovskite solar cells,” *Adv Mater Interfaces*, vol. 8, no. 10, p. 2100128, 2021.
- [143] R. Dong *et al.*, “Novel series of quasi-2D Ruddlesden–Popper perovskites based on short-chained spacer cation for enhanced photodetection,” *ACS Appl Mater Interfaces*, vol. 10, no. 22, pp. 19019–19026, 2018.

References

- [144] A. P. Thilakan *et al.*, "Origin of extended UV stability of 2D atomic layer titania-based perovskite solar cells unveiled by ultrafast spectroscopy," *ACS Appl Mater Interfaces*, vol. 11, no. 24, pp. 21473–21480, 2019.
- [145] W. Li *et al.*, "Enhanced UV-light stability of planar heterojunction perovskite solar cells with caesium bromide interface modification," *Energy Environ Sci*, vol. 9, no. 2, pp. 490–498, 2016.
- [146] A. Farooq *et al.*, "Spectral dependence of degradation under ultraviolet light in perovskite solar cells," *ACS Appl Mater Interfaces*, vol. 10, no. 26, pp. 21985–21990, 2018.
- [147] S.-H. Turren-Cruz, A. Hagfeldt, and M. Saliba, "Methylammonium-free, high-performance, and stable perovskite solar cells on a planar architecture," *Science (1979)*, vol. 362, no. 6413, pp. 449–453, 2018.
- [148] T. Yang, N. J. Jeon, H. Shin, S. S. Shin, Y. Y. Kim, and J. Seo, "Achieving long-term operational stability of perovskite solar cells with a stabilized efficiency exceeding 20% after 1000 h," *Advanced Science*, vol. 6, no. 14, p. 1900528, 2019.
- [149] D. Liu, J. Yang, and T. L. Kelly, "Compact layer free perovskite solar cells with 13.5% efficiency," *J Am Chem Soc*, vol. 136, no. 49, pp. 17116–17122, 2014.
- [150] W. Ke *et al.*, "Efficient hole-blocking layer-free planar halide perovskite thin-film solar cells," *Nat Commun*, vol. 6, no. 1, p. 6700, 2015.
- [151] J. Pascual *et al.*, "Electron Transport Layer-Free Solar Cells Based on Perovskite–Fullerene Blend Films with Enhanced Performance and Stability," *ChemSusChem*, vol. 9, no. 18, pp. 2679–2685, 2016.
- [152] R. Sandoval-Torrientes *et al.*, "Modified Fullerenes for Efficient Electron Transport Layer-Free Perovskite/Fullerene Blend-Based Solar Cells," *ChemSusChem*, vol. 10, no. 9, pp. 2023–2029, 2017.
- [153] J. Pascual *et al.*, "Co-solvent effect in the processing of the perovskite: fullerene blend films for electron transport layer-free solar cells," *The Journal of Physical Chemistry C*, vol. 122, no. 5, pp. 2512–2520, 2018.

References

- [154] P. Zhao *et al.*, “Insulated interlayer for efficient and photostable electron-transport-layer-free perovskite solar cells,” *ACS Appl Mater Interfaces*, vol. 10, no. 12, pp. 10132–10140, 2018.
- [155] L. Huang *et al.*, “Schottky/p-n Cascade Heterojunction Constructed by Intentional n-Type Doping Perovskite Toward Efficient Electron Layer-Free Perovskite Solar Cells,” *Solar Rrl*, vol. 3, no. 2, p. 1800274, 2019.
- [156] W. Wu, J. Liao, J. Zhong, Y. Xu, L. Wang, and J. Huang, “Suppressing Interfacial Charge Recombination in Electron-Transport-Layer-Free Perovskite Solar Cells to Give an Efficiency Exceeding 21%,” *Angewandte Chemie*, vol. 132, no. 47, pp. 21166–21173, 2020.
- [157] C. W. Jang, D. H. Shin, and S.-H. Choi, “Photostable electron-transport-layer-free flexible graphene quantum dots/perovskite solar cells by employing bathocuproine interlayer,” *J Alloys Compd*, vol. 886, p. 161355, 2021.
- [158] H. Kim, J. Seo, and N. Park, “Material and device stability in perovskite solar cells,” *ChemSusChem*, vol. 9, no. 18, pp. 2528–2540, 2016.
- [159] J. Bouclé and N. Herlin-Boime, “The benefits of graphene for hybrid perovskite solar cells,” *Synth Met*, vol. 222, pp. 3–16, 2016.
- [160] M. Piralaee and A. Asgari, “Nitride/Perovskite Tandem Solar Cell with High Stability: Analytical Study of Adjusting Current Matching Condition,” *Int J Energy Res*, vol. 2023, 2023.
- [161] D. Liu, J. Yang, and T. L. Kelly, “Compact layer free perovskite solar cells with 13.5% efficiency,” *J Am Chem Soc*, vol. 136, no. 49, pp. 17116–17122, 2014.
- [162] N. H. Tiep, Z. Ku, and H. J. Fan, “Recent advances in improving the stability of perovskite solar cells,” *Adv Energy Mater*, vol. 6, no. 3, p. 1501420, 2016.
- [163] T. A. Berhe *et al.*, “Organometal halide perovskite solar cells: degradation and stability,” *Energy Environ Sci*, vol. 9, no. 2, pp. 323–356, 2016.

References

- [164] X. Li *et al.*, “Outdoor performance and stability under elevated temperatures and long-term light soaking of triple-layer mesoporous perovskite photovoltaics,” *Energy Technology*, vol. 3, no. 6, pp. 551–555, 2015.
- [165] T. Liu, K. Chen, Q. Hu, R. Zhu, and Q. Gong, “Inverted perovskite solar cells: progresses and perspectives,” *Adv Energy Mater*, vol. 6, no. 17, p. 1600457, 2016.
- [166] K. Wojciechowski, D. Forgács, and T. Rivera, “Industrial opportunities and challenges for perovskite photovoltaic technology,” *Solar Rrl*, vol. 3, no. 9, p. 1900144, 2019.
- [167] H. J. Snaith *et al.*, “Anomalous hysteresis in perovskite solar cells,” *J Phys Chem Lett*, vol. 5, no. 9, pp. 1511–1515, 2014.
- [168] A. S. Subbiah, A. Halder, S. Ghosh, N. Mahuli, G. Hodes, and S. K. Sarkar, “Inorganic hole conducting layers for perovskite-based solar cells,” *J Phys Chem Lett*, vol. 5, no. 10, pp. 1748–1753, 2014.
- [169] G. E. Eperon, S. D. Stranks, C. Menelaou, M. B. Johnston, L. M. Herz, and H. J. Snaith, “Formamidinium lead trihalide: a broadly tunable perovskite for efficient planar heterojunction solar cells,” *Energy Environ Sci*, vol. 7, no. 3, pp. 982–988, 2014.
- [170] M. Saliba *et al.*, “How to Make over 20% Efficient Perovskite Solar Cells in Regular (n–i–p) and Inverted (p–i–n) Architectures,” *Chemistry of Materials*, vol. 30, no. 13, pp. 4193–4201, 2018.
- [171] N. J. Jeon *et al.*, “Compositional engineering of perovskite materials for high-performance solar cells,” *Nature*, vol. 517, no. 7535, pp. 476–480, 2015.
- [172] C.-H. Chiang, J.-W. Lin, and C.-G. Wu, “One-step fabrication of a mixed-halide perovskite film for a high-efficiency inverted solar cell and module,” *J Mater Chem A Mater*, vol. 4, no. 35, pp. 13525–13533, 2016.
- [173] S. Bonabi Naghadeh, B. Luo, G. Abdelmageed, Y.-C. Pu, C. Zhang, and J. Z. Zhang, “Photophysical properties and improved stability of organic–inorganic perovskite by surface passivation,” *The Journal of Physical Chemistry C*, vol. 122, no. 28, pp. 15799–15818, 2018.

References

- [174] Q. Qiu, H. Liu, Y. Qin, C. Ren, and J. Song, "Efficiency enhancement of perovskite solar cells based on Al₂O₃-passivated nano-nickel oxide film," *J Mater Sci*, vol. 55, pp. 13881–13891, 2020.
- [175] R. K. Misra *et al.*, "Temperature-and component-dependent degradation of perovskite photovoltaic materials under concentrated sunlight," *J Phys Chem Lett*, vol. 6, no. 3, pp. 326–330, 2015.
- [176] B. Conings *et al.*, "Intrinsic thermal instability of methylammonium lead trihalide perovskite," *Adv Energy Mater*, vol. 5, no. 15, p. 1500477, 2015.
- [177] W. Chen, L. Xu, X. Feng, J. Jie, and Z. He, "Metal acetylacetonate series in interface engineering for full low-temperature-processed, high-performance, and stable planar perovskite solar cells with conversion efficiency over 16% on 1 cm² scale," *Advanced Materials*, vol. 29, no. 16, p. 1603923, 2017.
- [178] N. Chander *et al.*, "Reduced ultraviolet light induced degradation and enhanced light harvesting using YVO₄: Eu³⁺ down-shifting nano-phosphor layer in organometal halide perovskite solar cells," *Appl Phys Lett*, vol. 105, no. 3, 2014.
- [179] A. Fujishima, T. N. Rao, and D. A. Tryk, "Titanium dioxide photocatalysis," *Journal of photochemistry and photobiology C: Photochemistry reviews*, vol. 1, no. 1, pp. 1–21, 2000.
- [180] G. Niu, X. Guo, and L. Wang, "Review of recent progress in chemical stability of perovskite solar cells," *J Mater Chem A Mater*, vol. 3, no. 17, pp. 8970–8980, 2015.
- [181] H. J. Snaith, "Perovskites: the emergence of a new era for low-cost, high-efficiency solar cells," *J Phys Chem Lett*, vol. 4, no. 21, pp. 3623–3630, 2013.
- [182] J. Huang, C. Gao, D. Zhang, Q. Tian, F. Zhang, and S. Liu, "Influence of film quality on power conversion efficiency in perovskite solar cells," *Coatings*, vol. 9, no. 10, p. 622, 2019.
- [183] G. Li *et al.*, "Co-Solvent Engineering Contributing to Achieve High-Performance Perovskite Solar Cells and Modules Based on Anti-Solvent Free Technology," *Small*, vol. 19, no. 28, p. 2301323, 2023.

References

- [184] X. He, J. Wu, T. Wu, Z. Lan, and M. Huang, "Dimethyl Sulfoxide Solvent Engineering for High Quality Cation-Anion-Mixed Hybrid and High Efficiency Perovskite Solar Cells," *Energy Technology*, vol. 7, no. 2, pp. 346–351, 2019.
- [185] X. Wu *et al.*, "Green-solvent-processed formamidinium-based perovskite solar cells with uniform grain growth and strengthened interfacial contact via a nanostructured tin oxide layer," *Mater Horiz*, vol. 10, no. 1, pp. 122–135, 2023.
- [186] X. Zhang *et al.*, "Blade Coating Inverted Perovskite Solar Cells with Vacuum-Assisted Nucleation Based on Bottom Quasi-2D Passivation," *Solar RRL*, vol. 7, no. 5, p. 2200900, 2023.
- [187] Y. Rong *et al.*, "Synergy of ammonium chloride and moisture on perovskite crystallization for efficient printable mesoscopic solar cells," *Nat Commun*, vol. 8, no. 1, p. 14555, 2017.
- [188] G. Wang *et al.*, "Efficient perovskite solar cell fabricated in ambient air using one-step spin-coating," *RSC Adv*, vol. 6, no. 49, pp. 43299–43303, 2016.
- [189] Y. Wang, T. Mahmoudi, H.-Y. Yang, K. S. Bhat, J.-Y. Yoo, and Y.-B. Hahn, "Fully-ambient-processed mesoscopic semitransparent perovskite solar cells by islands-structure-MAPbI₃-xCl_x-NiO composite and Al₂O₃/NiO interface engineering," *Nano Energy*, vol. 49, pp. 59–66, 2018.
- [190] J. Troughton, K. Hooper, and T. M. Watson, "Humidity resistant fabrication of CH₃NH₃PbI₃ perovskite solar cells and modules," *Nano Energy*, vol. 39, pp. 60–68, 2017.
- [191] Y. Wang *et al.*, "Interfacial engineering with carbon–graphite–Cu δ Ni 1– δ O for ambient-air stable composite-based hole-conductor-free perovskite solar cells," *Nanoscale Adv*, vol. 2, no. 12, pp. 5883–5889, 2020.
- [192] J. Huang *et al.*, "Ambient Engineering for High-Performance Organic–Inorganic Perovskite Hybrid Solar Cells," *ACS Appl Mater Interfaces*, vol. 8, no. 33, pp. 21505–21511, 2016.

References

- [193] F. Yang *et al.*, “Dependence of acetate-based antisolvents for high humidity fabrication of CH₃NH₃PbI₃ perovskite devices in ambient atmosphere,” *ACS Appl Mater Interfaces*, vol. 10, no. 19, pp. 16482–16489, 2018.
- [194] J. Troughton, K. Hooper, and T. M. Watson, “Humidity resistant fabrication of CH₃NH₃PbI₃ perovskite solar cells and modules,” *Nano Energy*, vol. 39, pp. 60–68, 2017.
- [195] T. Zhong *et al.*, “Additives and interface engineering facilitate the fabrication of high-efficiency perovskite solar cells in ambient air-processed,” *Journal of Materials Science: Materials in Electronics*, vol. 34, no. 12, Apr. 2023, doi: 10.1007/s10854-023-10417-7.
- [196] P. Liu *et al.*, “Ambient scalable fabrication of high-performance flexible perovskite solar cells,” *Energy Environ Sci*, Aug. 2024, doi: 10.1039/d4ee02925a.
- [197] P. Nagarjuna, P. N. Kumar, S. P. Singh, M. Deepa, and M. A. G. Namboothiry, “Efficient organic–inorganic hybrid perovskite solar cells processed in air,” *Physical Chemistry Chemical Physics*, vol. 16, no. 45, pp. 24691–24696, 2014.
- [198] P. Luo, Z. Liu, W. Xia, C. Yuan, J. Cheng, and Y. Lu, “Uniform, stable, and efficient planar-heterojunction perovskite solar cells by facile low-pressure chemical vapor deposition under fully open-air conditions,” *ACS Appl Mater Interfaces*, vol. 7, no. 4, pp. 2708–2714, 2015.
- [199] J. Huang *et al.*, “Ambient Engineering for High-Performance Organic–Inorganic Perovskite Hybrid Solar Cells,” *ACS Appl Mater Interfaces*, vol. 8, no. 33, pp. 21505–21511, 2016.
- [200] W.-T. Wang *et al.*, “Nanoparticle-induced fast nucleation of pinhole-free PbI₂ film for ambient-processed highly-efficient perovskite solar cell,” *Nano Energy*, vol. 49, pp. 109–116, 2018.
- [201] K. Huang *et al.*, “Highly Efficient Perovskite Solar Cells Processed Under Ambient Conditions Using In Situ Substrate-Heating-Assisted Deposition,” *Solar RRL*, vol. 3, no. 3, p. 1800318, 2019.

References

- [202] J. Ding *et al.*, “Fully air-bladed high-efficiency perovskite photovoltaics,” *Joule*, vol. 3, no. 2, pp. 402–416, 2019.
- [203] J. J. Yoo *et al.*, “Efficient perovskite solar cells via improved carrier management,” *Nature*, vol. 590, no. 7847, pp. 587–593, 2021.
- [204] T. Zhong *et al.*, “Additives and interface engineering facilitate the fabrication of high-efficiency perovskite solar cells in ambient air-processed,” *Journal of Materials Science: Materials in Electronics*, vol. 34, no. 12, p. 1055, 2023.
- [205] M. C. Eze *et al.*, “Optimum silver contact sputtering parameters for efficient perovskite solar cell fabrication,” *Solar Energy Materials and Solar Cells*, vol. 230, p. 111185, 2021.
- [206] F. S. Rocha, A. J. Gomes, C. N. Lunardi, S. Kaliaguine, and G. S. Patience, “Experimental methods in chemical engineering: Ultraviolet visible spectroscopy—UV-Vis,” *Can J Chem Eng*, vol. 96, no. 12, pp. 2512–2517, 2018.
- [207] B. D. Viezbicke, S. Patel, B. E. Davis, and D. P. Birnie III, “Evaluation of the Tauc method for optical absorption edge determination: ZnO thin films as a model system,” *physica status solidi (b)*, vol. 252, no. 8, pp. 1700–1710, 2015.
- [208] R. Kurre, S. Bajpai, and P. K. Bajpai, “Synthesis, characterization, optical and transport properties of BaSnO₃ synthesized by wet chemical route,” *Materials Sciences and Applications*, vol. 9, no. 1, pp. 92–110, 2018.
- [209] Y. Lv, Y. Jin, W. Cai, Z. Zhang, X. Zhou, and H. Chen, “Air-processed carbon-based perovskite solar cells with enhanced efficiency and stability: Effect of temperature control and using CuSCN,” *J Alloys Compd*, vol. 821, Apr. 2020, doi: 10.1016/j.jallcom.2019.153272.
- [210] T. Zhang *et al.*, “Crystallinity preservation and ion migration suppression through dual ion exchange strategy for stable mixed perovskite solar cells,” *Adv Energy Mater*, vol. 7, no. 15, p. 1700118, 2017.

References

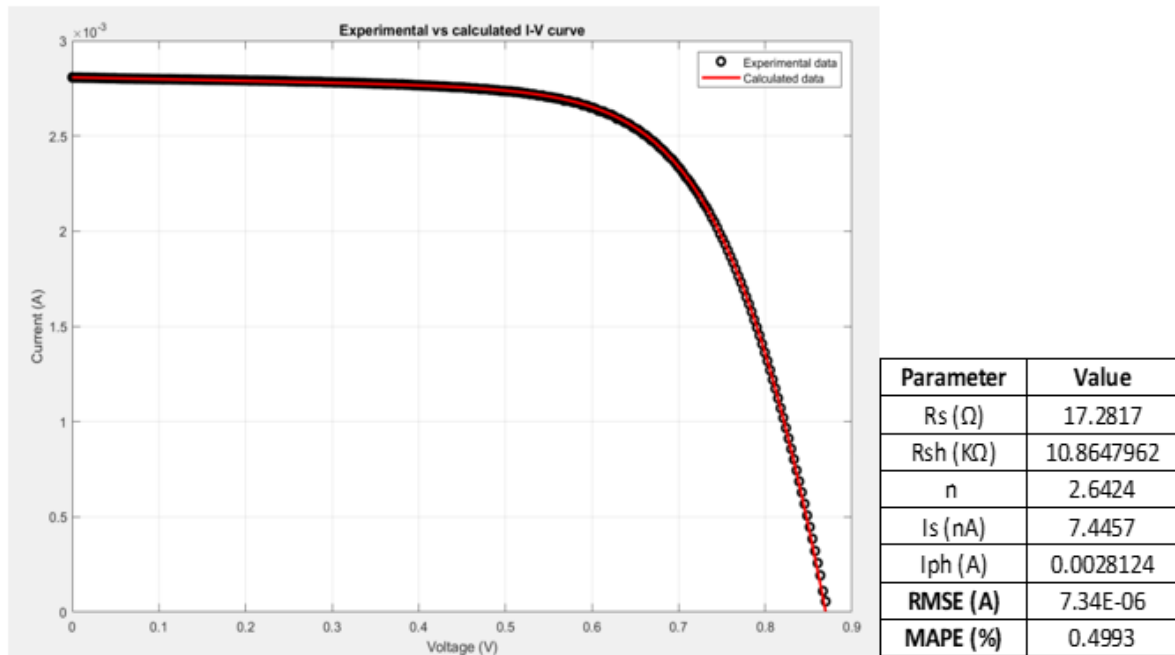
- [211] J. Liu *et al.*, “In situ growth of perovskite stacking layers for high-efficiency carbon-based hole conductor free perovskite solar cells,” *J Mater Chem A Mater*, vol. 7, no. 22, pp. 13777–13786, 2019.
- [212] K. Sveinbjörnsson *et al.*, “Ambient air-processed mixed-ion perovskites for high-efficiency solar cells,” *J Mater Chem A Mater*, vol. 4, no. 42, pp. 16536–16545, 2016.
- [213] N. Ahn, D.-Y. Son, I.-H. Jang, S. M. Kang, M. Choi, and N.-G. Park, “Highly reproducible perovskite solar cells with average efficiency of 18.3% and best efficiency of 19.7% fabricated via Lewis base adduct of lead (II) iodide,” *J Am Chem Soc*, vol. 137, no. 27, pp. 8696–8699, 2015.
- [214] N. J. Jeon, J. H. Noh, Y. C. Kim, W. S. Yang, S. Ryu, and S. Il Seok, “Solvent engineering for high-performance inorganic–organic hybrid perovskite solar cells,” *Nat Mater*, vol. 13, no. 9, pp. 897–903, 2014.
- [215] C. Zhou, A. B. Tarasov, E. A. Goodilin, P. Chen, H. Wang, and Q. Chen, “Recent strategies to improve moisture stability in metal halide perovskites materials and devices,” *Journal of Energy Chemistry*, vol. 65, pp. 219–235, 2022.
- [216] H. Yang, H. Wang, J. Zhang, J. Chang, and C. Zhang, “A Facile way to improve the performance of perovskite solar cells by toluene and diethyl ether mixed anti-solvent engineering,” *Coatings*, vol. 9, no. 11, p. 766, 2019.
- [217] C. Ying, C. Shi, N. Wu, J. Zhang, and M. Wang, “A two-layer structured Pbl₂ thin film for efficient planar perovskite solar cells,” *Nanoscale*, vol. 7, no. 28, pp. 12092–12095, 2015.
- [218] P. Docampo, F. C. Hanusch, N. Giesbrecht, P. Angloher, A. Ivanova, and T. Bein, “Influence of the orientation of methylammonium lead iodide perovskite crystals on solar cell performance,” *APL Mater*, vol. 2, no. 8, 2014.
- [219] C.-Y. Chang *et al.*, “Tuning perovskite morphology by polymer additive for high efficiency solar cell,” *ACS Appl Mater Interfaces*, vol. 7, no. 8, pp. 4955–4961, 2015.

References

- [220] Q.-Q. Ge *et al.*, “Promoting crystalline grain growth and healing pinholes by water vapor modulated post-annealing for enhancing the efficiency of planar perovskite solar cells,” *J Mater Chem A Mater*, vol. 4, no. 35, pp. 13458–13467, 2016.
- [221] D. D. S. Fung *et al.*, “Optical and electrical properties of efficiency enhanced polymer solar cells with Au nanoparticles in a PEDOT–PSS layer,” *J Mater Chem*, vol. 21, no. 41, pp. 16349–16356, 2011.

Appendix A: Other results not included in the main chapters.

A)



B)

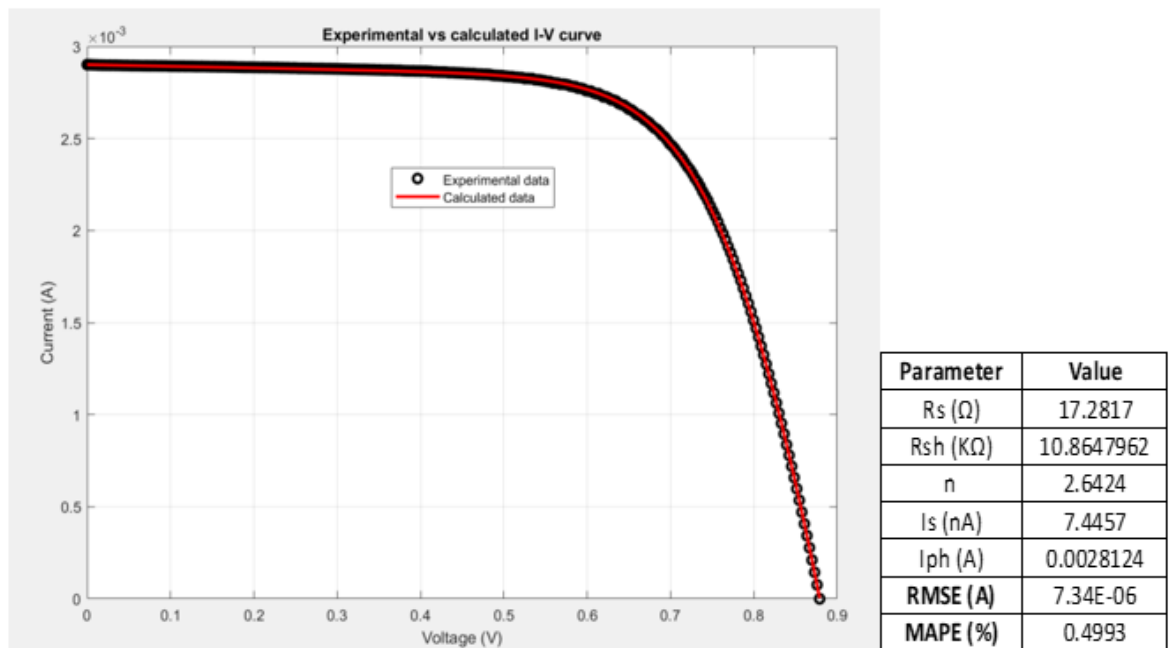


Figure 6-1 A) and B) illustrate the error between experimental and calculated I-V curves for perovskite devices.

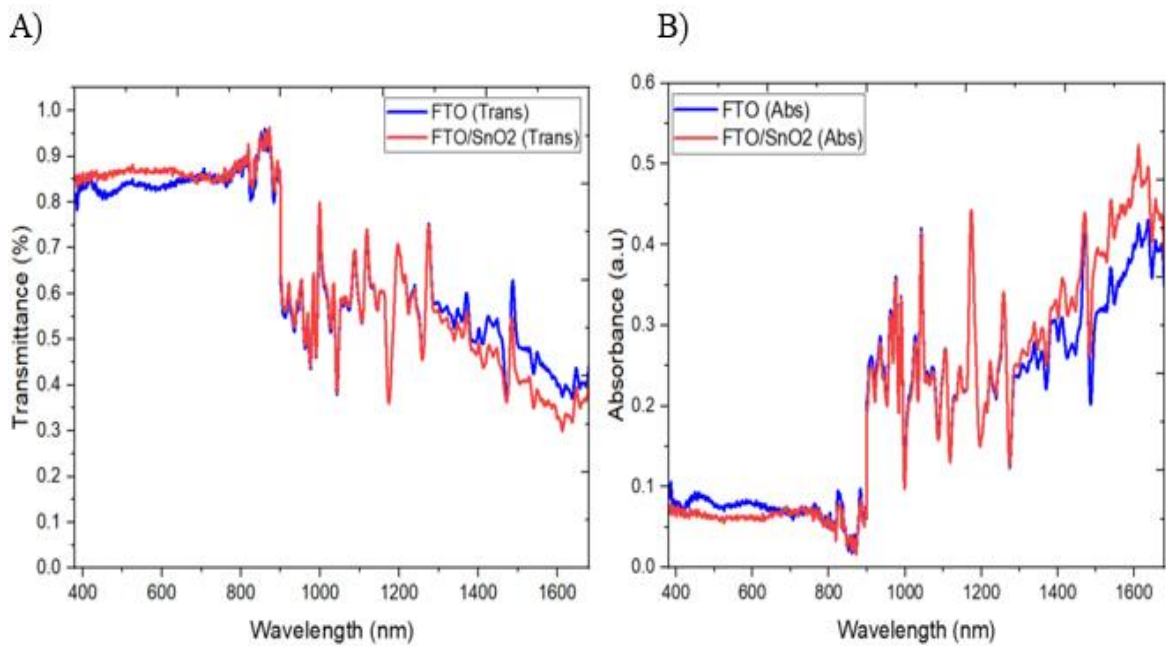


Figure 6-2 A) Transmission spectrum of FTO substrates and SnO₂ films deposited on FTO substrates. B) absorbance spectrum of FTO substrates and SnO₂ films deposited on FTO substrates.

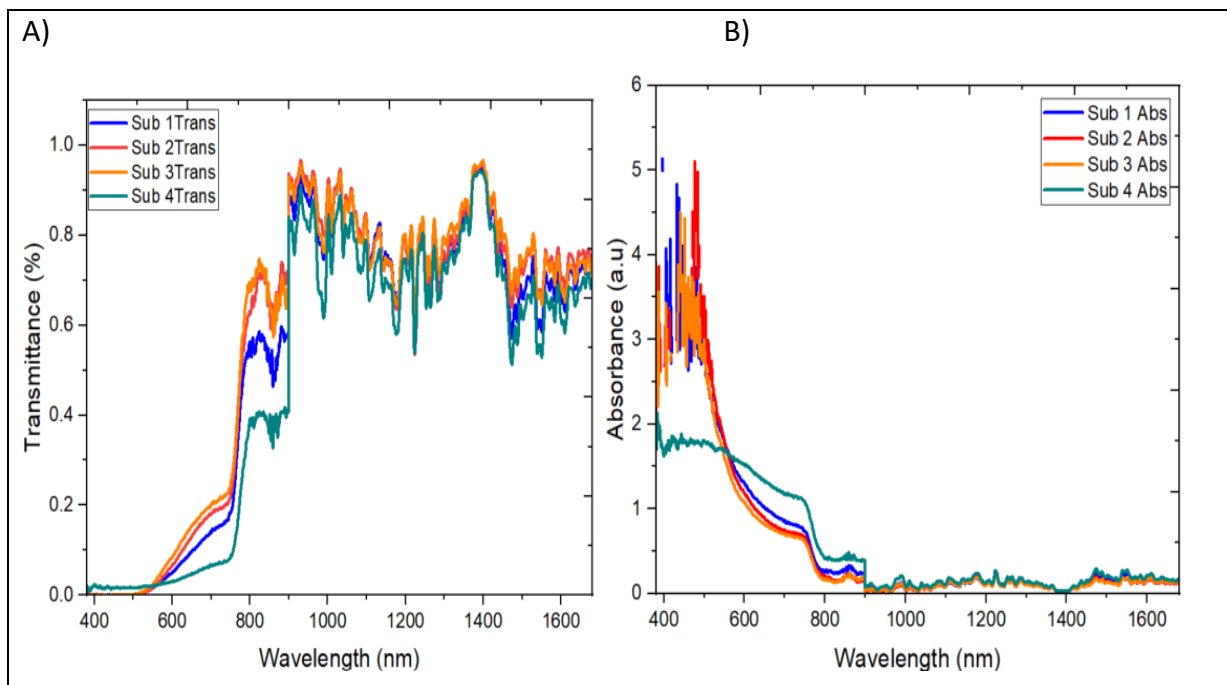


Figure 6-3 A) Transmittance spectra of FTO/SnO₂/MAPbI₃ films. B) absorbance spectra of FTO/SnO₂/MAPbI₃ films

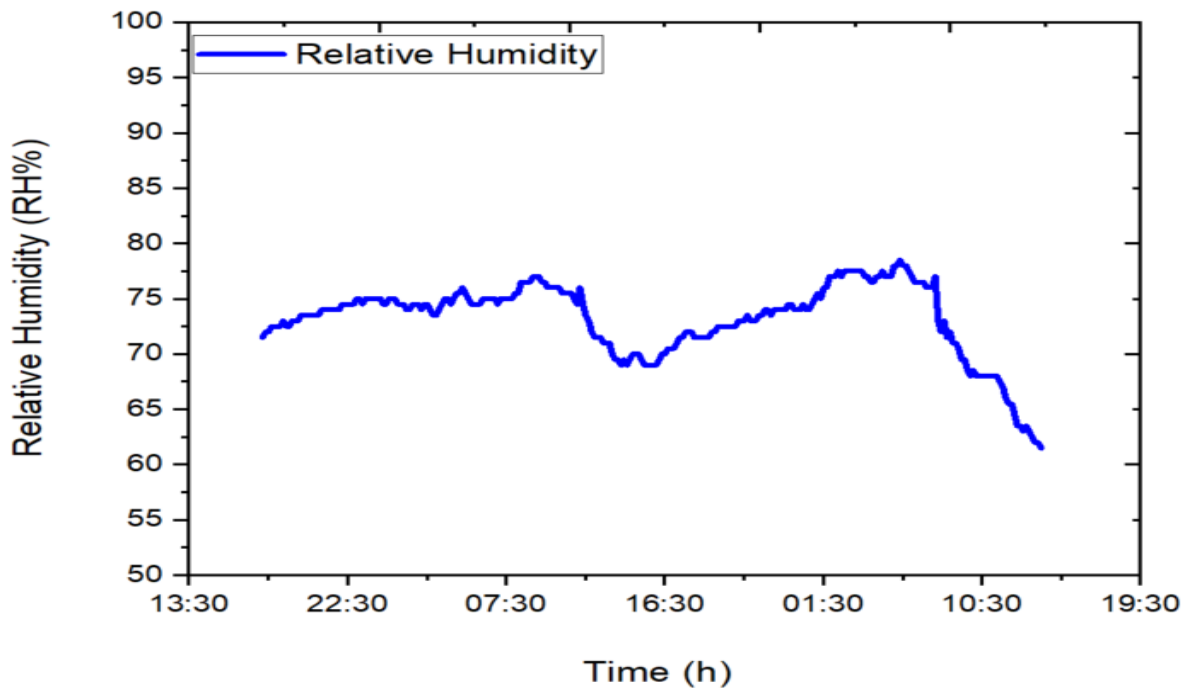


Figure 6-4 illustrates the humidity levels recorded over time in lab C3.03 at Cardiff University

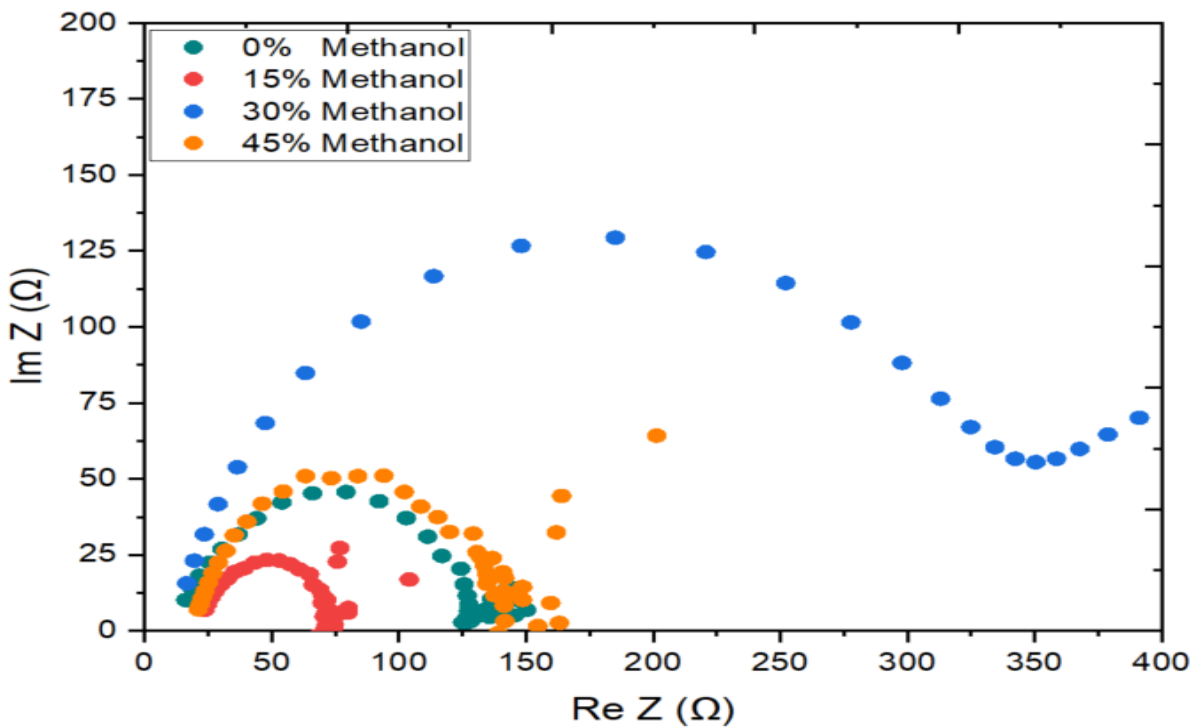


Figure 6-5 illustrates the Nyquist plot, which was generated by adding a combination of ethyl acetate and methanol as antisolvents at varying concentrations.

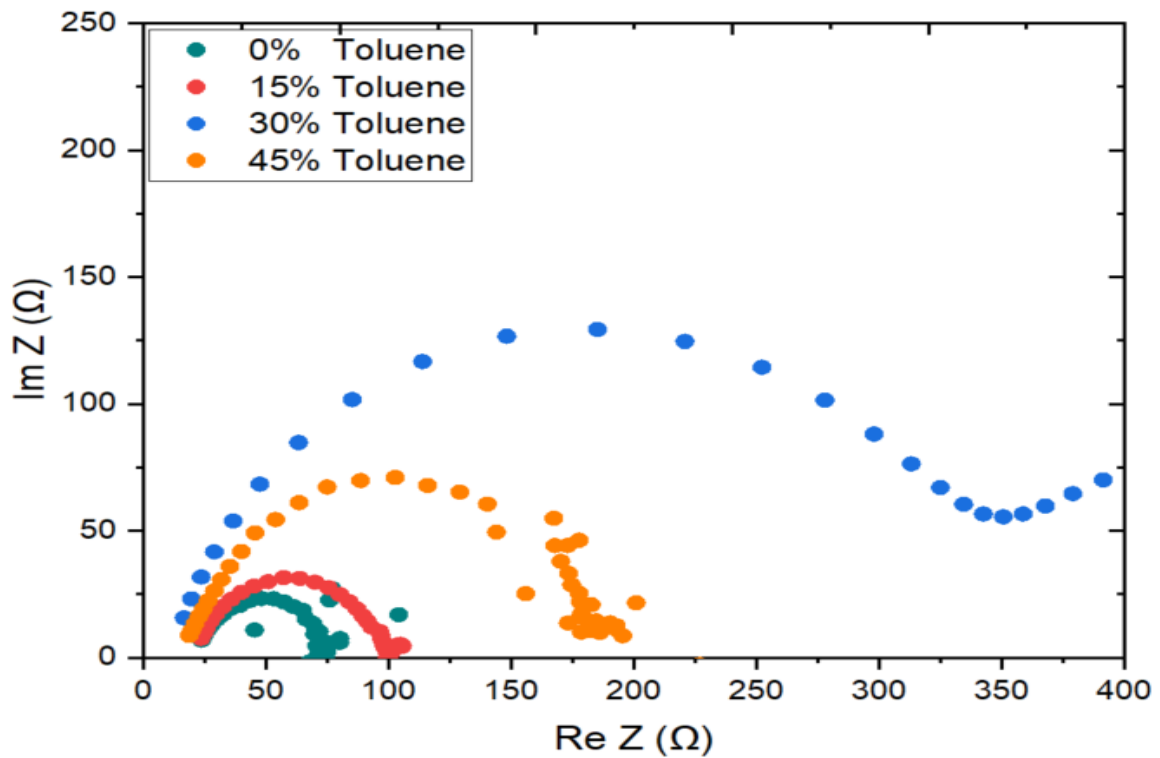


Figure 6-6 illustrates the Nyquist plot, which was generated by adding a combination of methyl acetate and toluene as antisolvents at varying concentrations.

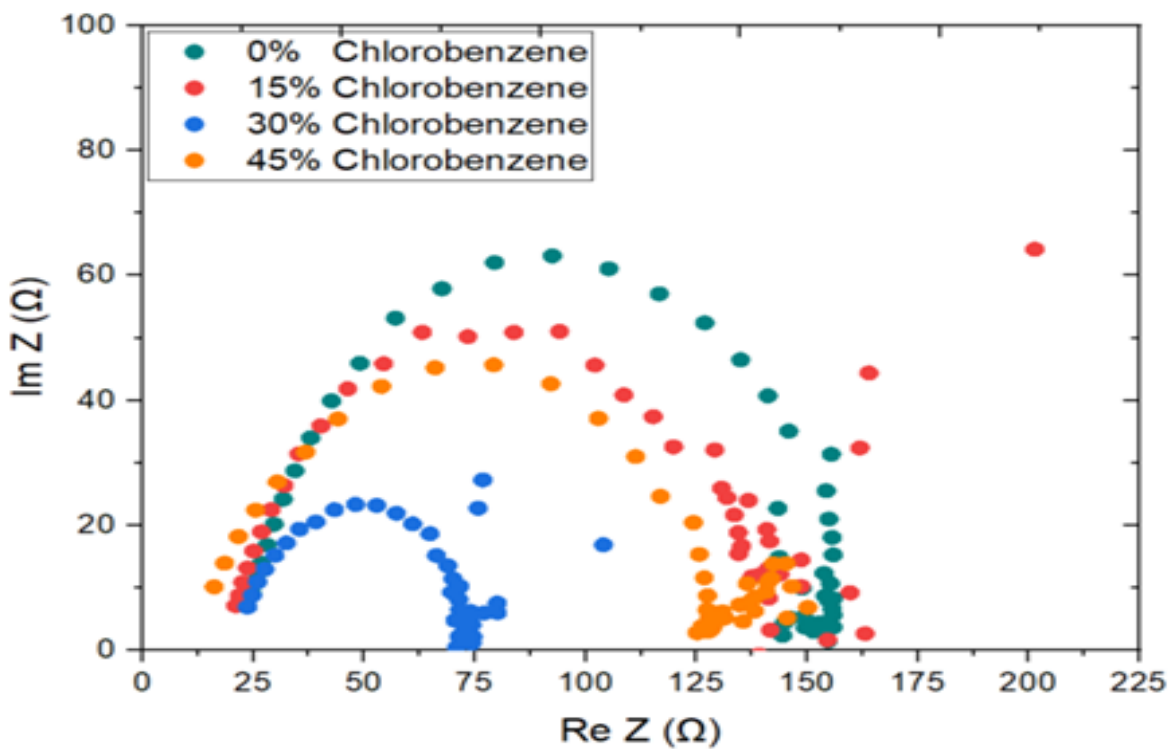


Figure 6-7 illustrates the Nyquist plot, which was generated by adding a combination of methyl formate and chlorobenzene as antisolvents at varying concentrations.

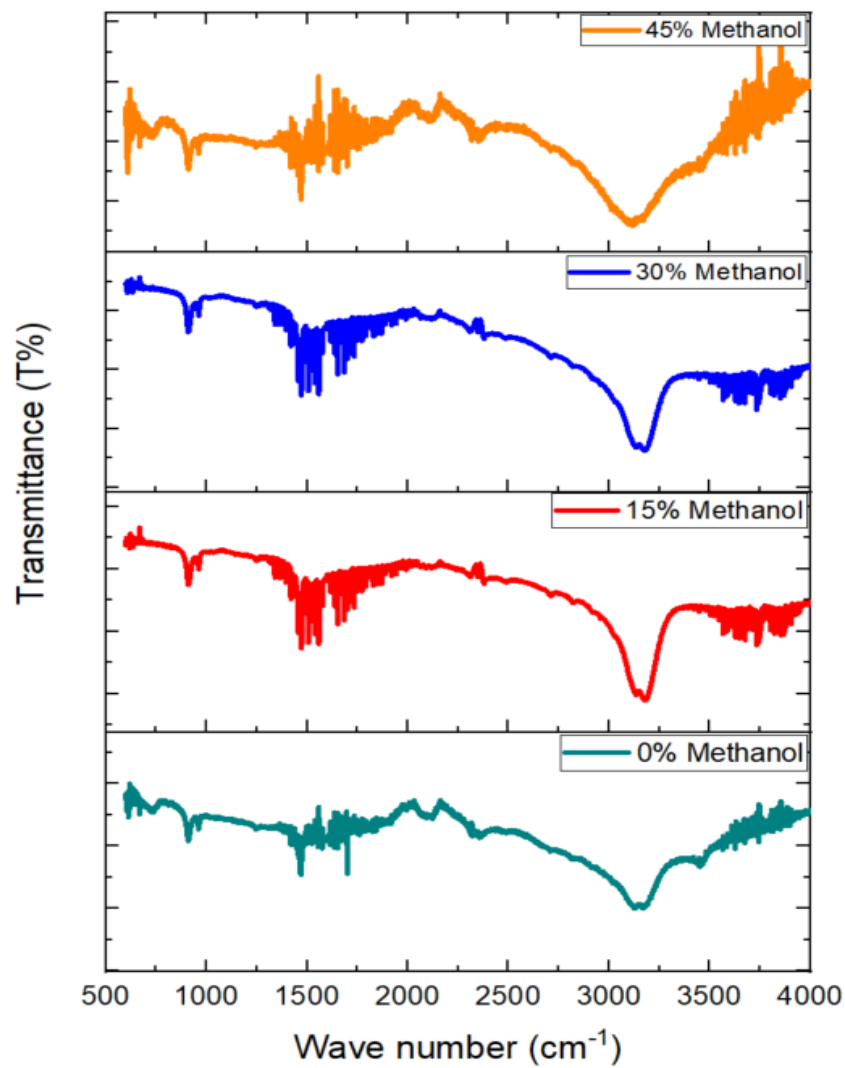


Figure 6-8 illustrates the FTIR spectra, which was generated by adding a combination of ethyl acetate and methanol as antisolvents at varying concentrations.

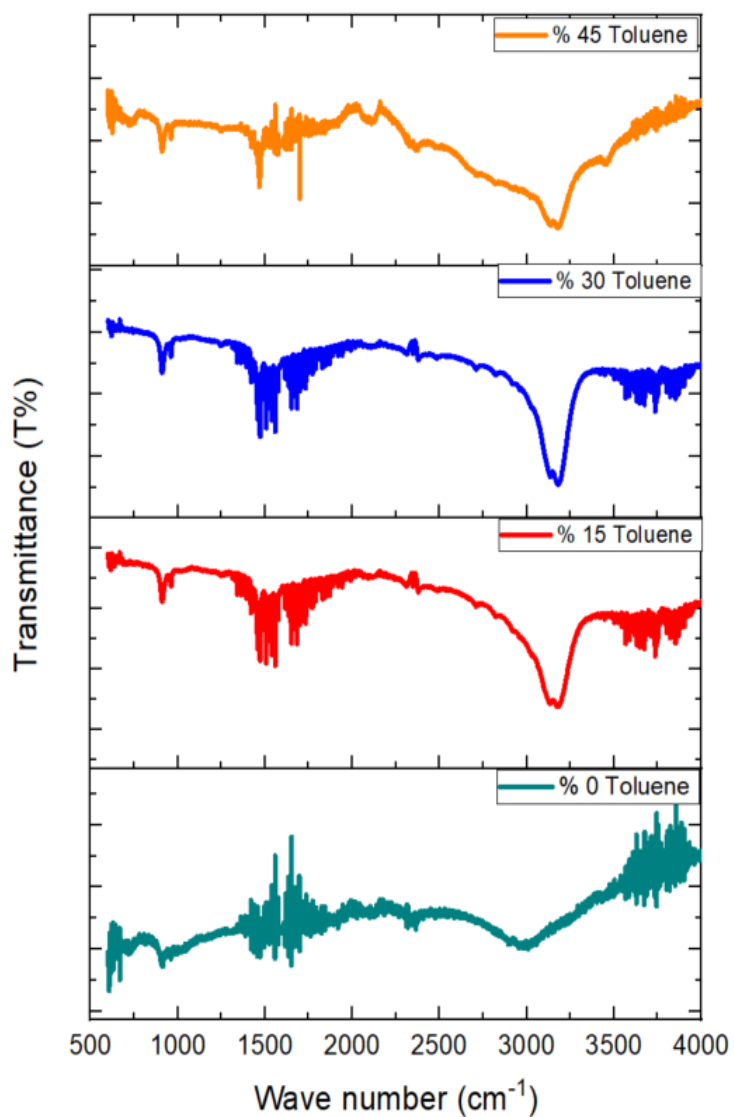


Figure 6-9 illustrates the FTIR spectra, which was generated by adding a combination of methyl acetate and toluene as antisolvents at varying concentrations.

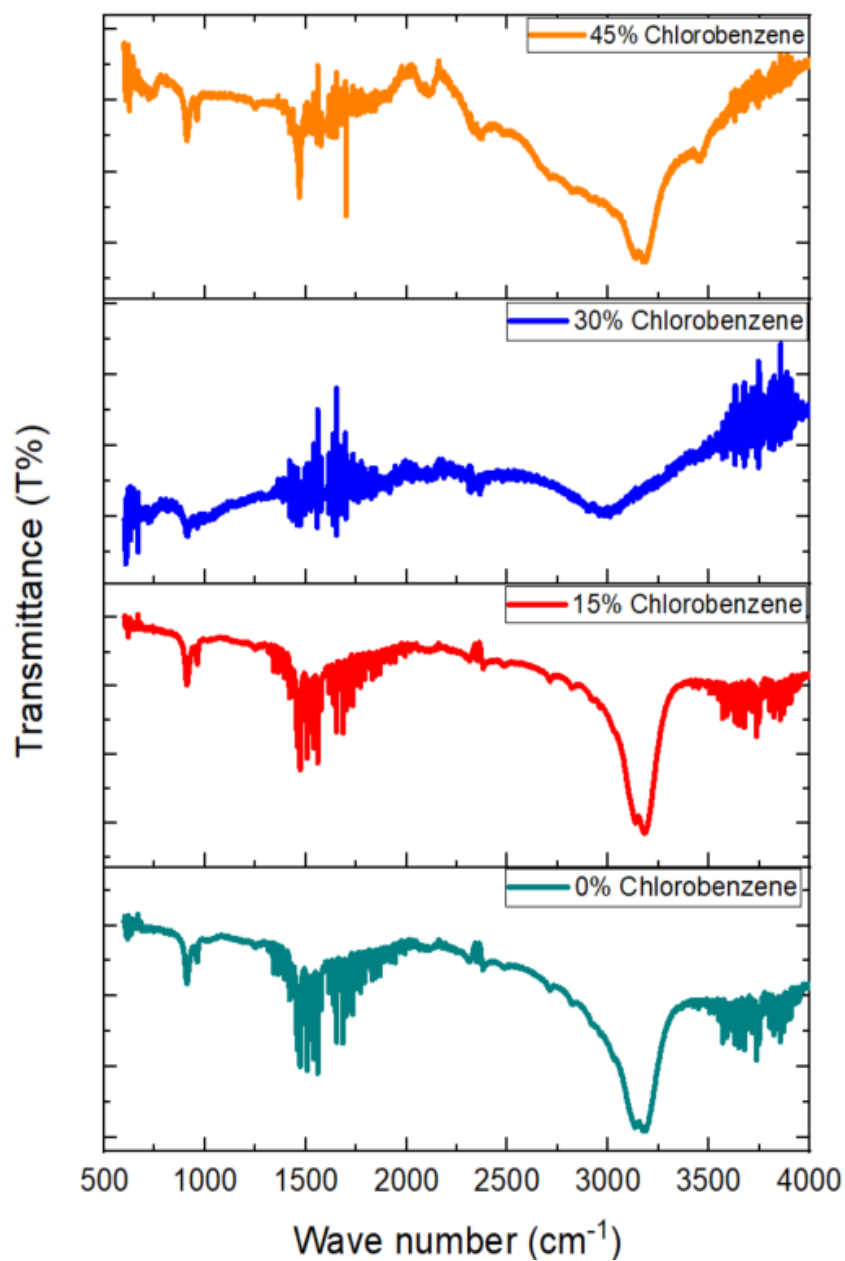


Figure 6-10 illustrates the FTIR spectra, which was generated by adding a combination of methyl formate and chlorobenzene as antisolvents at varying concentrations.

Appendix

Table 6-1 presents the measured electrical performance parameters of several perovskite devices.

Cells	R_s (Ω)	R_{sh} (Ω)	R_{CH} (Ω)	Extraction resistance (Ω)	Recombination resistance (Ω)	J_{sc} (mA/cm ²)	V_{oc} (V)	PCE (mW/cm ²)
Sub 8 C1	92	6666	335	0.276	0.036	20.77	1.04	12.43
Sub 8 C2	91	5262	319	0.287	0.043	22.07	1.06	13.31
Sub 7 C1	92	6250	275	0.333	0.029	23.46	0.97	11.73
Sub 7 C2	92	2856	260	0.354	0.059	24.29	0.95	11.40
Sub 6 C1	40	100000	279	0.145	0.002	21.68	0.91	12.83
Sub 6 C2	50	50000	286	0.174	0.005	20.96	0.90	11.81
Sub 6 C3	52	25000	322	0.161	0.011	18.59	0.90	10.66
Sub 8 C3	61	16666	279	0.219	0.013	19.86	0.83	10.40
Sub 7 C1	47	14286	304	0.154	0.018	19.34	0.88	11.62
Sub 7 C2	48	50000	311	0.156	0.005	18.72	0.87	11.06
Sub 7 C3	45	8333	298	0.151	0.030	19.86	0.89	12.07

Appendix

Sub 7 C4	42	25000	277	0.151	0.009	20.47	0.85	11.48
Sub 8 C1	71	8333	336	0.213	0.032	19.15	0.96	11.28
Sub 8 C2	89	7693	348	0.256	0.034	19.27	1.01	11.67
Sub 8 C3	63	8333	322	0.196	0.031	19.74	0.95	11.38
Sub 8 C4	77	7693	322	0.238	0.032	21.26	1.03	13.74
Sub 4 C2	118	4760	336	0.350	0.046	19.66	0.99	10.63
Sub 2 C1	99	3700	271	0.367	0.046	23.29	0.95	10.79
Sub 2 C2	104	20000	329	0.317	0.011	20.59	1.02	11.80
Sub 2 C3	101	6250	331	0.306	0.037	20.54	1.02	11.95

Appendix